Theoretical investigation of thermal transport in novel semiconductors with point defects

Mauro Fava

THÈSE

Pour obtenir le grade de

DOCTEUR DE L'UNIVERSITÉ GRENOBLE ALPES

Spécialité : PHYSIQUE DES MATERIAUX

Arrêté ministériel : 25 mai 2016

Présentée par

Mauro FAVA

Thèse dirigée par **Natalio MINGO**

Co-encadrée par **Ambroise VAN ROEKEGHEM**

préparée au sein du **Laboratoire Laboratoire d'Innovation pour les Technologies des Energies Nouvelles (LITEN - CEA)**
dans **l'École Doctorale Physique**

Etude théorique du transport thermique dans de nouveaux semi-conducteurs avec des défauts ponctuels

Theoretical investigation of thermal transport in novel semiconductors with point defects

Thèse soutenue publiquement le **27 avril 2021**,
devant le jury composé de :

Monsieur David BROIDO
PROFESSEUR, BOSTON COLLEGE, Rapporteur
Monsieur Georg H. K. MADSEN
PROFESSEUR, Technische Universität Wien, Rapporteur
Monsieur Jean-Louis BARRAT
PROFESSEUR DES UNIVERSITES, UNIVERSITE GRENOBLE ALPES, Président
Monsieur Stefano MOSSA
INGENIEUR HDR, CEA CENTRE DE GRENOBLE, Examinateur
Monsieur Jesús CARRETE MONTAÑA
DOCTEUR EN SCIENCES, Technische Universität Wien, Examinateur

Abstract

In this thesis we couple the projected augmented wave formulation of density functional theory with the Boltzmann transport equation for phonons to study the thermal transport in semiconductors. In particular, a recently developed Green's functions formalism is used to compute the phonon-defect scattering rates through evaluation of the T-matrix and application of the optical theorem. This methodology is explained and applied to study extrinsic dopants in boron arsenide (BAs) and p-type half-Heusler compounds (HHs).

BAs is a novel material with promising electronic and thermal management applications in virtue of its high room-temperature thermal conductivity (κ), while p-type HHs have induced a large interest in the scientific community in the recent years in virtue of their promising thermoelectric applications in medium temperature range.

In the case of boron arsenide we study a set of stable impurities that possess a dual nature of acceptors and donors, depending on which atom they substitute, and we assess how neutral and ionised dopants differently scatter phonons and reduce the thermal conductivity. We also extend our formulation to account for effects induced by the thermodynamics of defect formation and we evaluate how κ is reduced by a mixing of charged and neutral acceptors and donors.

In the case of half-Heuslers we study the role of the complete perturbation induced by substitutional defects on the lattice with respect to simpler models, and we give an explanation of the numerical results in term of pristine compound properties, namely electron and phonon projected density of states. Finally, we find a simple analytical model that fit the *ab initio* conductivity curves with few percent of errors.

Acknowledgement

A doctoral research program is the first doorstep to a life of exploration of the mysteries of Nature, and like all form of explorations, one knows the starting point but not the end of the journey. Since February 2018 I had the fortune to work on the modelling of several interesting materials in collaboration with many people around the world. I had the opportunity to understand and know not just important facts about my field of investigation, but also (part of) the right mindset to face physics in a professional way. Whereas I did not always find optimal results at every corner, I had the possibility to freely and creatively *explore* many paths and possible solutions.

I would like to express my gratitude towards Dr. Natalio Mingo for choosing me for this project and for leading my scientific growth throughout the last three years with keen suggestions, fruitful debates and the encouragement to "find my own way" through the research problems we tried to solve. I am also grateful to Dr. Ambroise Van Roekeghem for his advice and help in preparing this manuscript, and to Dr. Anton Bochkarev for his aid during my first year as a doctoral student. Among our collaborators, I thank prof. David Broido for his collaboration and suggestions during the preparation of the boron arsenide manuscript, and prof. Jesús Carrete for helping me with *almaBTE* related issues and with the draft of the half-Heuslers paper. I also thank Bonny Dongre, Nakib Haider Protik and Chunhua Li for our mail exchange concerning the accuracy of the data, and the thesis commission members Dr. Stefano Mossa and prof. Georg K. H. Madsen for listening at my yearly presentations and for giving me suggestions that enriched my work. Finally I would like to thank my family and my girlfriend Neda, for their being supportive in the last three years despite the many miles between us. I also dedicate this work to them.

Résumé

Dans cette thèse, nous couplons la formulation "projected augmented wave" de la théorie fonctionnelle de densité avec l'équation de transport de Boltzmann pour les phonons pour étudier le transport thermique dans les semiconducteurs. En particulier, un formalisme basé sur les fonctions de Green récemment développé est utilisé pour calculer les taux de diffusion des phonons par les défauts par l'évaluation de la matrice T et l'application du théorème optique. Cette méthodologie est expliquée et appliquée afin d'étudier les dopants extrinsèques dans l'arséniure de bore (BAs) et les composés demi-Heusler de type p (HHs).

BAs est un nouveau matériau avec des applications de gestion électronique et thermique prometteuses en raison de sa conductivité thermique (κ) à température ambiante élevée, tandis que les HHs de type *p* ont suscité un grand intérêt dans la communauté scientifique ces dernières années pour à leurs applications thermoélectriques prometteuses dans une plage de températures moyennes (entre 500 and 800 °C).

Dans le cas de l'arséniure de bore, nous étudions un ensemble d'impuretés stables qui possèdent une double nature d'accepteurs et de donneurs, selon l'atome qu'elles remplacent, et nous évaluons comment les dopants neutres et ionisés dispersent différemment les phonons et réduisent la conductivité thermique. Nous étendons également notre formulation pour tenir compte des effets induits par la thermodynamique de la formation des défauts et nous évaluons comment κ est réduit par un mélange d'accepteurs et de donneurs chargés et neutres.

Dans le cas des demi-Heuslers, nous étudions le rôle de la perturbation complète induite par des défauts de substitution sur le réseau par rapport à des modèles plus simples, et nous donnons une explication des résultats numériques á partir des propriétés du composé pur, à savoir les densités d'états électroniques et phononiques projetées sur les différentes orbitales atomiques. Enfin, nous proposons un modèle analytique simple qui correspond aux courbes de conductivité *ab initio* avec un faible pourcentage d'erreur.

Contents

List of Figures

List of Tables

1

Introduction

> Twas brillig, and the slithy toves Did gyre and gimble in the wabe; All mimsy were the borogoves, And the mome raths outgrabe.
>
> *Lewis Carroll*

All over the last decades there has been a steady trend over miniaturisation of electronic components with the aim of increasing the number of transistors per unit surface and to achieve better device performances. This trend is summarised by the Moore's law, which predicts a yearly doubling of the number of transistors that can be cast in a surface. This has proven to be remarkably accurate in the last fifty years. However, miniaturisation comes at a price. As an electric current flows through a (microscopic) device, it also generates heat due to the scattering between electrons and the lattice. This heat can hamper the current and even damage the component itself if it is not rapidly dissipated. Thus, the search for materials capable of achieving the latter task has become particularly vivid in the last few years. Heat dissipation has been recognised as one of the major hurdles in trying to keep up with the maintenance of the Moore's law in the future. Furthermore, along with the quest for green sources of energy, there has been a search for materials that allow for the efficient conversion of dissipated heat into electricity, with the goal of improving the energy efficiency of devices.

The transport of heat in semiconductors poses a challenge to many fields, such as the improvement of LED devices, development of batteries and micro and nanoelectronics. Doping plays a pivotal role as it must be tuned to achieve required device performances. While the thermal properties of pristine materials have been widely studied in the last century with great success, only in recent years has computational power permitted careful calculations of defect properties with an *ab initio* level of accuracy. It is clear that a deeper understanding of the interplay between defect thermodynamics, crystal growth and transport is needed not just for the technological applications but also in the search for novel materials that could outperform currently used semiconductors. A thorough understanding of the internal mechanisms behind thermal transport has proven to be of high relevance in order to drive society towards a greener future and better performances of electronic devices.

The objective of this thesis is to model how extrinsic dopants affect the thermal conductivity of semiconductors from first principles from a coupled density functional theory - Boltzmann transport equation perspective. The reasons behind this choice ensue from a quest of both accuracy of the calculations - something that can be achieved only if the inner quantum mechanical nature of crystals is taken into account - while at the same time testing and exploring methods that can prove useful to speed up the search for better performing materials for technological applications. A first modelling bottleneck is the determination of the set of impurities that can be added into a pristine crystal. In this case, first principles calculations help to identify specific kind of dopants and concentrations at a given temperature. Then the scattering between heat carrier (only phonons in the present work) and impurities has to be evaluated for different concentrations and temperatures. The thermal conductivity, labelled as κ, is the final descriptor for the evaluation of the thermal performances of a material and how they are influenced by defects.

The thesis is organised in the following way: chapter 2 gives a survey of density functional theory and lattice dynamics as well, introducing the concept of phonons as main heat carriers in non-degenerate semiconductors and insulators and digging out the main features of defect thermodynamics. Chapter 3 presents the theory behind

thermal transport in crystalline solids in details, deriving expressions for the thermal conductivity within the linear response and Boltzmann equation formalism. We will study the main mechanisms that affect phonons with particular emphasis on point defects as scattering centers. Chapters 4 and 5 present a survey on the recent research about the thermal properties of boron arsenide along with the results obtained during the development of this thesis. Finally, chapters 6 and 7 will show, respectively, an introduction and results for a set of half-Heusler ternary compounds with promising thermoelectric properties. Chapter 8 will highlights the conclusions for this work.

2

First principles phonon theory

2.1 Symmetries in crystals

2.1.1 Basic lattice properties

A 3D crystal is described by an infinite set of points in space, the so called "crystal lattice". The position of these points can be reconstructed by the discrete span of three basis vector. Given the basis, each point of the lattice can be uniquely identified by a linear combination of these vectors and the application of the translation symmetry over a discrete group manifold. The lattice vectors, here defined as $\vec{a}_1$, $\vec{a}_2$, $\vec{a}_3$, define a parallelepiped containing a single point of the lattice, and thus identifiable as primitive unit cell: thence, any point defined by

$$\vec{V}_{n_1,n_2,n_3} = n_1\vec{a}_1 + n_2\vec{a}_2 + n_3\vec{a}_3 \equiv \vec{V}_N, \tag{2.1}$$

with n_i integers belongs to the crystal, which can be clearly presented as the repetition in space of the primitive cell. Let's consider now a generic L2-integrable function, $f(\vec{r})$, that possess the same symmetry of the lattice and let's write it as Fourier series:

$$f(\vec{r}) = \sum_k f_k e^{i\vec{Q}_k\cdot\vec{r}}. \tag{2.2}$$

It is straightforward to notice that, for the function to fulfill the equality $f(\vec{r}) = f(\vec{r}+\vec{V}_N)$, a condition on the $\vec{Q}_k$ has to be imposed, specifically

$$\vec{Q}_k \cdot \vec{V}_N = 2\pi N \tag{2.3}$$

with N integer. The $\vec{Q}_k$ vectors that satisfy such condition possess the same periodicity of the original lattice and are defined in Fourier space. They form what is called "reciprocal lattice". Whereby in reciprocal space it is possible to define a transformed function that is invariant under translations and periodic.

We can use eq. 2.3 to construct the reciprocal lattice in a similar fashion as for the direct one. Given the direct lattice unit-cell volume, $V = \vec{a}_1 \cdot (\vec{a}_2 \wedge \vec{a}_3)$, to satisfy eq. 2.3 we can define

$$\vec{b}_i \equiv \frac{2\pi}{V} \vec{a}_j \wedge \vec{a}_k. \tag{2.4}$$

Thus, in the Fourier space the three vectors $\vec{b}_1$, $\vec{b}_2$ and $\vec{b}_3$ define a point of the reciprocal lattice and a unit cell in Reciprocal space, the latter being conventionally named "Brillouin zone" (BZ); as in the direct lattice, a span of the basis vector with integer coefficients allows to reach every point of the transformed lattice. Having functions periodic in reciprocal space is clearly helpful for the calculations, as it permits to focus on the BZ only, as for the other regions they can be reached by translations.

As for the unit cell types, there are several ways the lattice vector can orient and thus several possible geometries. As far we are concerned in this thesis, we are going to study zincblende materials, such that the three lattice vectors are taken equal in modulus and forming an orthogonal triad and such that the basis is constituted by two atoms in the unit cell. A choice of the lattice vector for this structure in the monatomic case is as follows:

$$\vec{a}_1 = (-1,0,1)\frac{a}{2}, \tag{2.5}$$

$$\vec{a}_2 = (0,1,1)\frac{a}{2}, \tag{2.6}$$

$$\vec{a}_3 = (-1,1,0)\frac{a}{2}, \tag{2.7}$$

a being the lattice constant of the material under consideration. By mean of eq. 2.4 the basis vector in reciprocal space are

$$\vec{b}_1 = (-1,-1,1)\frac{2\pi}{a}, \tag{2.8}$$

$$\vec{b}_2 = (1,1,1)\frac{2\pi}{a}, \tag{2.9}$$

$$\vec{b}_3 = (-1,1,-1)\frac{2\pi}{a}, \tag{2.10}$$

which correspond to a body-centered cubic lattice. It is also customary to identify the center of the Brillouin zone $(0,0,0)$ as Γ - point.

2.1.2 Bloch's theorem, electron bands and energy gap

Let's consider a crystal (lattice vectors $\vec{a}_1$, $\vec{a}_2$, $\vec{a}_3$) in a periodic potential V, such that:

$$V(\vec{x}_0) \equiv V(\vec{x}_0 + \vec{R}), \tag{2.11}$$

with $\vec{R} \equiv n_x\vec{a}_1 + n_y\vec{a}_2 + n_z\vec{a}_3 \equiv \vec{n}\cdot\vec{a}$, and n_x,n_y,n_z integers. We will show now that the wave-function in a material where the translation symmetry holds must have the following form:

$$\psi(\vec{r}) = e^{i\vec{k}\vec{r}}u(\vec{r}), \tag{2.12}$$

where $u(\vec{r}) = u(\vec{r}+\vec{R})$ has the same periodicity of the lattice and the wave-vector $\vec{k}$ is generated by the reciprocal basis. This is the Bloch's theorem.

It is clear that the Hamiltonian is invariant under the translation operator $\hat{T}_{\vec{a}}$ ($\vec{x} \longrightarrow \vec{x}+\vec{R}$):

$$[\hat{T}, \hat{H}] = 0. \tag{2.13}$$

Thus, either operator can be diagonalised with the same basis. We can also note that

$$T_{\vec{a}}\psi(\vec{r}) = t_{\vec{a}}\psi(\vec{r}) = \psi(\vec{r}+\vec{R}), \tag{2.14}$$

$$T_{\vec{b}}T_{\vec{a}}\psi(\vec{r}) = t_{\vec{b}}t_{\vec{a}}\psi(\vec{r}) = \psi(\vec{r}+\vec{a}+\vec{b}) = T_{\vec{a}+\vec{b}}\psi(\vec{r}) = t_{\vec{a}+\vec{b}}\psi(\vec{r}), \tag{2.15}$$

meaning that $t_{\vec{a}} = e^{ik\vec{n}\cdot\vec{a}}$, with $\vec{k}$ real vector generated by the reciprocal basis of the crystal. If we define now a function $u(\vec{r}) = e^{-i\vec{k}\vec{r}}\psi(\vec{r})$, we can easily see that it must have the periodicity of the lattice and this completes our proof. Let's consider now a periodic single particle Hamiltonian:

$$-\frac{\hbar^2\nabla^2}{2m}\psi + V\psi = E\psi. \tag{2.16}$$

Because of the translation symmetry and the Bloch's theorem, the potential can be re-written as $V(\vec{r}) = \sum_{\vec{G}} V_{\vec{G}} e^{i\vec{G}\cdot\vec{r}}$ and the wavefunction as $\psi(\vec{r}) = \sum_{\vec{G}} \psi_{\vec{G}} e^{i(\vec{G}+\vec{k})\cdot\vec{r}}$, with $\vec{G}$ belonging to the reciprocal lattice, meaning that

$$\left(\frac{\hbar^2 k^2}{2m} - E\right)\psi_{\vec{G}} + \sum_{\vec{G}} V_{\vec{G}}\psi_{\vec{G}-\vec{k}} = 0, \tag{2.17}$$

where the approximation $\nabla^2 u(\vec{r}) \ll k^2 u(\vec{r})$ has been used. Even considering the $V \to 0$ limit, the solution of the previous equation cannot be the free-electron model one, namely $\sim e^{i\vec{k}\cdot\vec{r}}$, as the latter and clearly neglects the periodicity of the lattice and the

degeneracy at the edges of the BZ. Therefore, we shall include a certain number of Fourier coefficients - let's say n - which characterise the state. This n - index is the "band index", and labels the Bloch' state along with $\vec{k}$. In presence of a weak but non-zero periodic potential $\sim V_0 \cos\left(\vec{G}\cdot\vec{r}\right)$, first order perturbation theory straightforwardly shows how the degeneracy is removed and an energy-gap is created, that is $E_{+,-} = \hbar^2 k^2/2m \pm V_0$. Considering the spin degeneracy, for an N - electron system (in the BZ) we can accommodate them from the lowest energy state to the highest according to the Pauli's exclusion principle. These considerations are of paramount importance to predict whether a material has insulating or metallic properties. In absence of strong electronic correlations, the crystal possesses metallic properties if the band with higher energy is only partially unoccupied. If that band is fully occupied, then the system is an insulator or a semiconductor, and energies of the order of E_{gap} are required to excite its electrons.

2.2 Density functional theory

The accurate modeling of the ground state properties of materials requires the use of the principles of quantum mechanics (QM) and the solution of the time-independent Schrödinger equation

$$-\sum_i \frac{\hbar^2}{2m_i}\nabla^2\psi + V\psi = E\psi. \tag{2.18}$$

However, due to the exponential-like scaling of the Hilbert space for the ground state search, finding the exact QM solution is practically unfeasible even for systems with relatively few atoms. This has produced a plethora of methods to cope with the numerical hurdles and approximately but realistically find the quantum properties of a system in its ground state. We can shortly mention the Hartree-Fock method, tight-binding and variational approaches or Monte Carlo based techniques. It can be proven, however, that we don't need the exact ground state wave-function ψ to model the ground state properties of a material: we just need the single particle density function ρ. This is the basis for what is called density functional theory (DFT): we will

now highlight the basic theorems behind DFT that make it, at least in principle, an exact ground state theory. We can consider a system defined by

$$\hat{H} = \hat{H}_0 + \hat{V}_{ext}, \tag{2.19}$$

where $\hat{H}_0$ includes the contribution from kinetic energies and inter-particle interactions, while $\hat{V}_{ext}$ represents an external potential. By considering $\hat{H}_0$ fixed, it is clear that the ground state wave-function and thus all the system properties, single particle density included, are a functional of the external potential. At the core of DFT lies the fact that there is a 1:1 correspondence between the external potential (by a constant factor) and ρ. To prove it, we will follow the standard argument of Kohn and Hohenberg [15].

Let us assume we have two external potentials, $\hat{V}_1$ and $\hat{V}_2$ s.t. their difference is not a constant but s.t. they lead to the same single particle density. We can now make the following associations:

- $\hat{V}_i \longrightarrow \{\psi_i, E_i\}$;
- $\hat{V}_1 \longrightarrow \rho \longleftarrow \hat{V}_2$;

That is, we assume the two potentials, i.e. two different ground states, may produce the same electronic density. For each case we can use the variational theorem:

$$E_1 < \langle \psi_2 | \hat{H}_1 | \psi_2 \rangle = E_2 + \langle \psi_2 | \hat{V}_1 - \hat{V}_2 | \psi_2 \rangle = E_2 + \int \rho_2(\vec{r})[V_1(\vec{r}) - V_2(\vec{r})]d^3r, \tag{2.20}$$

$$E_2 < \langle \psi_1 | \hat{H}_2 | \psi_1 \rangle = E_1 - \langle \psi_1 | \hat{V}_1 - \hat{V}_2 | \psi_1 \rangle = E_1 - \int \rho_1(\vec{r})[V_1(\vec{r}) - V_2(\vec{r})]d^3r. \tag{2.21}$$

If we now take $\rho_1 = \rho_2$, we obtain $E_1 + E_2 < E_1 + E_2$ which completes our proof. Up to a constant factor the external potential is consequently fully determined by the single particle density and therefore the knowledge of ρ can in principle be used to infer all

the ground state properties of the system, with the true ground state density function being the one that minimises the density functional energy. We can split the total energy of the system as a sum of kinetic and potential terms:

$$E[\rho] = T[\rho] + E_H[\rho] + E_{xc}[\rho] + \int v_{ext}(\vec{r})\rho(\vec{r})d^3r \equiv F[\rho] + \int v_{ext}(\vec{r})\rho(\vec{r})d^3r, \tag{2.22}$$

where the external potential contribution is separated from the internal part, dubbed F, which constitutes a universal functional. The elements T, E_H and E_{xc} are the kinetic, Hartree and exchange-correlation (XC) energies respectively. A standard expression is known for the Hartree term, of Coulombic origin:

$$v_H(\vec{r},[\rho]) = \int d^3r' \frac{\rho(\vec{r'})}{|\vec{r}-\vec{r'}|} \equiv \frac{\delta E_H[\rho]}{\delta\rho}. \tag{2.23}$$

However, an exact expression for the kinetic and exchange-correlation functionals $T[\rho]$ and $E_{xc}[\rho]$ respect to the density is unknown. Within the called orbital-free density functional approach [16] explicit expressions of T with respect to the electronic density can be derived. This approach resembles closely the Thomas-Fermi model [17], a density-based theory for interacting many-body electron systems that predates DFT. We will explore in more details the strategy devised by Kohn and Sham [18]. To estimate T consists into splitting ρ into single particle contributions $\{\phi_\alpha\}_{1..N}$, with α shorthand for $\vec{k}, n$ (wave-vector and band index, respectively); this way and considering the α-state occupancy f_α we can define density and kinetic operator as:

$$\rho(\vec{r}) = \sum_\alpha f_\alpha |\phi_\alpha(\vec{r})|^2 \tag{2.24}$$

and

$$T[\rho] = -\frac{\hbar^2}{2m}\sum_\alpha f_\alpha \int \phi^*_\alpha(\vec{r})\nabla^2\phi_\alpha(\vec{r})d^3r, \tag{2.25}$$

where f_α is either 1 or 0 depending on whether the α state is occupied or not. Finally by minimising the energy functional we get, for each of the N degrees of freedom in our system, the so called Kohn-Sham (KS) equations:

$$-\frac{\hbar^2}{2m}\phi_\alpha + v[\rho]\phi_\alpha = \varepsilon_\alpha \phi_\alpha \tag{2.26}$$

$\forall \alpha \in \{1...N\}$ where

$$v[\rho] = v_{ext} + v_H(\vec{r},[\rho]) + v_{xc}(\vec{r},[\rho]). \tag{2.27}$$

Eq. 2.26 are non linear with respect to the Kohn-Sham eigenvectors and they have to be solved self-consistently. The numerical procedure generally involves the expansion of the KS eigenstates with respect to a known basis. The choice of this basis includes plane waves, although it is possible to use more localised states like Gaussians, Slater or hydrogen atom basis. Due to the requirement of orthogonality between different wavefunctions, the behaviour of the states close to the nuclei is usually characterised by strong oscillations, which require a considerable number of basis set coefficients in order to be properly described. Often to speed up the calculations it is preferable to continuously smoothen the description of the states near the core (within a certain cutoff) while retaining their true behaviour out of the core region. Moreover, since inner states are mostly localised, they do not play a relevant role in typical solid state and chemical phenomena and therefore can be treated within a "frozen core" approximation, which means they can be computed for isolated atoms and transferred to crystals and molecules. This is the basic philosophy behind pseudopotential theory (PT) [19], with the internal electrons absorbed into the ionic potential so that it is possible to construct smooth valence (pseudo)wavefunctions.

We also mention the projector augmented wave method (PAW), conceptually similar to PT and in the context of plane waves [20]. Since this is going to be the approach used in our calculations, it is worth giving it a short introduction. PAW introduces a linear operator $\hat{\tau}$ such that:

$$|\phi_\alpha\rangle \equiv \hat{\tau}\left|\tilde{\phi}_\alpha\right\rangle, \tag{2.28}$$

where $|\phi_\alpha\rangle$ is the all-electron one-particle KS wavefunction and $\left|\tilde{\phi}_\alpha\right\rangle$ is a pseudo-state that has a smoother behaviour near the atom nuclei. The original and the pseudo wavefunctions differ only in a region close to the atomic nucleus and this prompts to define:

$$\hat{\tau} = \hat{1} + \sum_R \hat{\tau}_R, \tag{2.29}$$

with $\hat{\tau}_R$ vanishing out of a sphere near the nuclei and defined by the radius R. If we expand $\left|\tilde{\phi}_\alpha\right\rangle$ as a linear combination with respect to a pseudo-basis $\left|\tilde{\theta}_i\right\rangle$ we can write:

$$\hat{\tau} = \hat{1} + \sum_i (|\theta_i\rangle - \left|\tilde{\theta}_i\right\rangle) \langle p_i|, \tag{2.30}$$

where $|\theta_i\rangle \equiv \hat{\tau}\left|\tilde{\theta}_i\right\rangle$ are the all electron wavefunctions for an isolated atom and $|p_i\rangle$ are "projector functions" orthonormal to the $\left|\tilde{\theta}_i\right\rangle$ pseudostates. Then operators can be written in terms of this representation that preserve the all-electron eigenvalue spectrum [21], and again, the frozen core approximation is usually employed. It should be noted that the computational cost of solving the KS equations for a system of N$\sim 10^{23}$, typical for a solid, is still obviously too high. Nevertheless, in a crystalline material the periodicity comes in help: we can enormously reduce the number of degrees of freedom by considering only those belonging to the first Brillouin zone. We are left with the problem of evaluating E_{xc}. Although DFT is in principle an exact theory, the reliability of its prediction is intertwined with the accuracy of the chosen exchange-correlation functional. This term has been introduced as an improvement of the single particle approximation - previously used to define the Hartree and kinetic part of the KS equations - which neglects the effect of particle exchange and the many-body correlations present in the real systems. An electronic propriety that, for example, is subtly sensitive to the choice of the XC functional is the band gap, whose determination

is pivotal for the understanding of several physical properties - like the dielectric functions, refraction indices and doping to mention a few - where the physics is largely dominated by the electronic behaviour around the Fermi surface. Functionals that make use of the LDA [22] or GGA [23] approximations often fail to properly represent the many-body electronic correlations inside a material, while other methodologies like hybrid functionals [24], the random phase approximation [25, 26, 27, 28] and other Green's function based techniques like the Hedin equations and GW [29, 30] perform better while still preserving the single particle nature of the KS equations, although with a higher numerical cost.

Finally, the stability of the Fermi surface is of paramount importance to get the iterative solution of the Kohn-Sham equations properly converged. This turns to be of extreme importance when studying metals, where the close proximity of the occupied bands respect to the unoccupied ones prompts the use of fractional "smeared" occupations for the KS - states even at zero temperature [31, 32, 33].

2.2.1 Born-Oppenheimer approximation and ion dynamics

In a solid the degrees of freedom are typically electrons and nuclei. Since the latter are much heavier than the former, they usually also present a much slower dynamics. When this is the case, the complexity of the calculations can be reduced by separating the electronic from the nuclear contribution. Once we fix the atomic coordinates, we can solve the electronic problem alone, and use the electronic energy as a field for the ion dynamics. Thus, we define a total wave-function:

$$\tilde{\Psi}_{Ne}(\vec{R}_j,\vec{r}_i) = \sum_{q=1}^{M} \Psi_q(\vec{R}_j)\chi_q(\vec{R}_j,\vec{r}_i), \tag{2.31}$$

where $\{\vec{R}_j\}_j$ and $\{\vec{r}_i\}_i$ represent ionic and electronic coordinates, respectively. The electronic part is found by solving

$$\hat{H}_e\chi_q(\vec{R}_j,\vec{r}_i) = E_q(\vec{R}_i)\chi_q(\vec{R}_j,\vec{r}_i) \tag{2.32}$$

and finally, the electronic energy surface E_q (typically the ground state) is inserted into the nuclei Hamiltonian:

$$[\hat{H}_N(\vec{R}_j) + \hat{E}_q(\vec{R}_i)]\Psi_q(\vec{R}_j) = E_{tot}\Psi_q(\vec{R}_j). \tag{2.33}$$

The nuclear Hamiltonian is generally not diagonal with respect to the electronic states, mainly because of the $\vec{R}_j$-dependence of the latter (vibrionic couplings): being able to safely neglect the off-diagonal elements is what is called Born-Oppenheimer (BO) approximation [34]. If the ion dynamics is slow, the electronic wavefunctions evolve adiabatically in the nuclei potentials, so that the $|\vec{\nabla}_{\vec{R}_i}\chi_q|$-terms are small. Since the off-diagonal elements of the nuclear Hamiltonian $\langle\chi_s|\hat{H}_N|\chi_q\rangle$ are proportional to $(E_q - E_s)^{-1}$, the separation (non-crossing) between different energy surfaces E_q and E_s is a necessary condition for the BO approximation to hold. The Born-Oppenheimer evolution of a system can be studied by solving eq. 2.32 first in the field of the ions and then updating the atomic positions with eq. 2.33. Then, the electronic calculations can be repeated with the updated nuclei positions.

Considering that the relevant thermodynamic, mechanical, and transport properties of solids are mostly insensitive to nuclear quantum mechanical and vibrionic effects, the computational burden can be further lowered by assuming classical motion for the atoms in the electronic potential energy surface. In the context of DFT, this is translated into considering the total energy in a crystal as:

$$E_{tot} = E_{NN} + T_N + E_{ee} + T_e + U_{Ne}, \tag{2.34}$$

where E_{NN} (E_{ee}) is the nucleus-nucleus (electron-electron) interaction, T_N (T_e) is the nuclei (electrons) kinetic energy and U_{Ne} represents the ion-electron potential. The total density of the system at the DFT level can be written as:

$$\rho_{tot}(\vec{R},\vec{r}) = \rho_e(\vec{R},\vec{r}) + \rho_N(\vec{R},\vec{r}) = \rho_e(\vec{R},\vec{r}) + \sum_i^{N_{ion}} Z_i \delta(\vec{R} - \vec{R}_i). \tag{2.35}$$

The KS equations can be solved for the electronic part only and with U_{Ne} as the external potential. Once the solution of the electronic problem is known, the density itself can be used to determine the forces on which the nuclei dynamics depend. To get the QM force due to the atom-j displacement, the Hellman-Feynman theorem [35] is employed:

$$\vec{F}_j = -\langle\psi|\vec{\nabla}_j\hat{H}|\psi\rangle - \vec{\nabla}_j E_{NN} = -\int \rho(\vec{r})\frac{\partial v_{ext}}{\partial \vec{R}_j} d^3r - \vec{\nabla}_j E_{NN}, \tag{2.36}$$

and the ion positions can be updated consequently with Newton's second law: $\vec{R}_j(t) \longrightarrow \vec{R}_j(t+dt) = \vec{R}_j(t) + \vec{F}_j(t)dt$. Then the KS equations must be solved for the new atomic positions and so on, to get the full classical dynamics. As the classical dynamics from first principles is generally a primary tool to extract the thermodynamical properties of a system assuming the ergodic hypothesis, it can be necessary to speed it up to get a thorough sampling of the phase space. A method developed for this purpose is the Car-Parrinello molecular dynamics [36], which assumes an adiabatic coupling between electronic and atomic degrees of freedom. Therefore, a classical Lagrangian can defined for the electrons that follow *adiabatically* the ionic motion. Another frequently used approach is the metadynamics [37], which in short introduces a fictitious potential that is used to fill deep minima of the free energy so to explore a larger region of phase space than with the true dynamics at the same simulation length conditions.

In this thesis we are going to study systems where the BO approximation holds. However, neglecting the vibrionic coupling - i.e. the variation of the KS wavefunctions with respect to changes in the ion positions - is not advisable in those systems where there is crossing between different potential energy surfaces or, for instance, in presence of Kohn anomalies [38]. Therefore several theoretical tools have been designed to "diabatically" couple different energy surfaces. We mention the diabatic transformation of the ion Hamiltonian developed by Smith [39] and, in the semiclassical dynamics

context, the surface hopping method [40, 41] among the tools developed to study what nowadays is a very active field of research.

2.3 Lattice dynamics

2.3.1 Phonons

The total potential energy V for an N-atoms crystal with M atoms in the unit cell can be expanded in a Taylor series. Close to the minimum energy configuration the leading order of V is quadratic in the ion displacements:

$$V(\{u_i\}_i) = V_0 + \frac{1}{2}\sum_{i,j} u_i \Phi_{i,j} u_j, \tag{2.37}$$

where the index i is a shorthand for $(\vec{R}, \tau, \alpha)$, that is unit cell point, label for the position of the atom inside the unit cell ($\vec{r}_\tau$) and cartesian direction, respectively. The term u_i represents the displacement of the i^{th} degree of freedom w.r.t. the minimum energy position and $\Phi_{i,j}$ are the second derivatives of the energy w.r.t. the displacements or interatomic force constants (IFCs) evaluated in the equilibrium configuration. Lastly, the V_0 term represents the energy for the non-displaced configuration; it is irrelevant for the following calculations and it can be taken to be zero. To solve this system classically, we take the equations of motions:

$$m_i \ddot{u}_i = -\sum_j \Phi_{i,j} u_j. \tag{2.38}$$

To proceed further, we will resort to normal mode analysis. Let's assume that we can write $u_i(t) = A_{\tau,\alpha} e^{i\omega t}$: in this way, eq. 2.38 can be rewritten as

$$m_\tau \omega^2 A_{\tau\alpha} = \sum_{R',\tau',\beta} \Phi^{R',\tau',\beta}_{R,\tau,\alpha} A_{\tau',\beta}, \tag{2.39}$$

where we have resorted to the full index notation. We recognise also that the atomic positions can be written as $\vec{R}_\tau \equiv \vec{R} + \vec{r}_\tau \equiv \vec{R}(\tau)$. Let's define $A_{\tau,\alpha}(\vec{q}) = e^{i\vec{q}\cdot\vec{R}_\tau}\varepsilon_{\tau,\alpha}(\vec{q})$, where $\vec{q}$ belongs to the first Brillouin zone, and $s_{\tau,\alpha}(\vec{q}) \equiv \varepsilon_{\tau,\alpha}(\vec{q})\sqrt{m_\tau}$. This rewriting leads to

$$\omega^2 s_{\tau,\alpha}(\vec{q}) = \sum_{R',\tau',\beta} \frac{1}{\sqrt{m_\tau m_{\tau'}}} \Phi^{R',\tau',\beta}_{R,\tau,\alpha} e^{i\vec{q}\cdot[\vec{R}'(\tau') - \vec{R}(\tau)]} s_{\tau',\beta}(\vec{q}). \tag{2.40}$$

Now we can exploit the invariance under translation of the IFCs to set $\vec{R} \equiv \vec{0}$ - which fixes the unit cell - and thus define the "dynamical matrix" of the system:

$$D^{\tau'\beta}_{\tau\alpha}(\vec{q}) \equiv \frac{1}{\sqrt{m_\tau m_{\tau'}}} \sum_{R'} \Phi^{R',\tau',\beta}_{0,\tau,\alpha} e^{i\vec{q}\cdot[\vec{R}'(\tau') - \vec{0}(\tau)]}, \tag{2.41}$$

which leads to

$$\sum_{\tau',\beta} D^{\tau'\beta}_{\tau\alpha}(\vec{q}) s_{\tau',\beta}(\vec{q}) = \omega^2 s_{\tau,\alpha}(\vec{q}). \tag{2.42}$$

Thus, the original N-atoms (3N degrees of freedom) problem has been mapped into a system with only 3M degrees of freedom as result of the translation symmetry: solving it means solving an eigenvalue equation in the form of eq. 2.42, to get a spectrum of the form $\{\omega^2_{b,\vec{q}}, \vec{s}_{b,\vec{q}}\}_{\vec{q},b}$ where b denotes the branch index stemming from the M-atomic character of the unit cell. We can write the displacements as:

$$\vec{u}_{R(\tau)}(t) = \frac{1}{\sqrt{N m_\tau}} \sum_{\vec{q},b} e^{i(\vec{q}\cdot\vec{R}(\tau) - \omega_{\vec{q},b}t)} \vec{s}_{\vec{q},b} Q_b(\vec{q}), \tag{2.43}$$

with the eigenstates assumed to be normalised and $Q_b(\vec{q})$ being the amplitude of the oscillations. Therefore we can have a complete description of the dynamics in terms of collective atomic vibrations. We can also understand the appearance of three soft modes ($\omega_{b,\vec{q}} \to 0$) in the $\vec{q} \to 0$ limit as result of the invariance of the IFCs with respect to global translations in space. To get further understanding we restrict ourselves to the simple case of a 1D diatomic chain of atoms of masses m_1 and m_2 and lattice constant

a in presence of nearest neighbours interactions only, labelled as C. The two branches of the system have the following expression:

$$\omega^2_{\vec{q},\pm} = \frac{C}{m_1 m_2}\left[m_1 + m_2 \pm \sqrt{m_1^2 + m_2^2 + 2m_1 m_2 \cos(qa)}\right]. \tag{2.44}$$

In the long-wavelength limit the $-$ $(+)$ solution is proportional to q (constant), i.e. it has constant (zero) group velocity. The $-$ branch corresponds to the acoustic modes, as they are associated to the propagation of sound in a crystal, with the unit cell atoms moving in phase. The $+$ case to the optical modes, the name coming from the two atoms oscillating out-of phase in the small $\vec{q}$ limit. This may originate an electric dipole if the atoms possess opposite charges, thence generating an electromagnetic field. In real materials the EM frequency associated with optical phonons generally belongs to the infrared spectrum.

So far we have analysed the problem only from a classical point of view, but we will see now that the quantum extension is easy to derive in the normal modes framework. Since we can expand the atomic displacements and momenta with respect to normal modes like in eq. 2.44, it be seen that in the phonon representation the kinetic and quadratic potential parts of the energy are equal and can be cast as:

$$K = V = \frac{1}{2}\sum_{b,\vec{q}} \omega^2_{\vec{q},b} |Q_b(\vec{q})|^2. \tag{2.45}$$

Therefore the total energy is:

$$E = \sum_{b,\vec{q}} \omega^2_{\vec{q},b} |Q_b(\vec{q})|^2. \tag{2.46}$$

It can be noticed how we have reduced our original problem to a set of independent harmonic oscillators. We can now think of the crystal as a "perfect gas" made of collective oscillating normal modes. Let's apply the canonical quantization, namely:

$$u_i, p_j \longrightarrow \hat{u}_i, \hat{p}_j \tag{2.47}$$

and

$$\{u_i, p_j\}_{P.B.} = \delta_{i,j} \longrightarrow \frac{[\hat{u}_i, \hat{p}_j]}{i\hbar} = \delta_{i,j}. \tag{2.48}$$

Given eq. 2.44 it is clear to satisfy the Heisenberg uncertainty relation the now quantized amplitude $\hat{Q}_b(\vec{q})$ and its adjoint $\hat{Q}_b^\dagger(\vec{q})$ must in turn satisfy $[\hat{Q}_b(\vec{q}), \hat{Q}_b^\dagger(\vec{q})] = \hbar\delta_{\vec{q},\vec{q}'}\delta_{b,b'}/\omega_{\vec{q},b}$. If we define the operators $\hat{a}_{\vec{q},b}$ and $\hat{a}_{\vec{q},b}^\dagger$ so that $[\hat{a}_b(\vec{q}), \hat{a}_b^\dagger(\vec{q})] = \delta_{\vec{q},\vec{q}'}\delta_{b,b'}$, we have:

$$\hat{a}_{\vec{q},b} = \sqrt{\frac{\hbar}{\omega_{\vec{q},b}}}\hat{Q}_{\vec{q},b} \tag{2.49}$$

and

$$\hat{a}_{\vec{q},b}^\dagger = \sqrt{\frac{\hbar}{\omega_{\vec{q},b}}}\hat{Q}_{\vec{q},b}^\dagger. \tag{2.50}$$

We can exploit the properties of the commutator to rewrite the quantized Hamiltonian as

$$\hat{H} = \sum_{b\vec{q}} \hbar\omega_{b\vec{q}}\left(\hat{a}_{b,\vec{q}}^\dagger \hat{a}_{b,\vec{q}} + \frac{1}{2}\right), \tag{2.51}$$

which possesses the form of a sum over different quantized harmonic oscillators at different frequencies. The hereby defined $\hat{a}_{b,\vec{q}}^\dagger$ and $\hat{a}_{b,\vec{q}}$ are the bosonic creation and annihilation operators. We also identify $\hat{a}_{b,\vec{q}}^\dagger \hat{a}_{b,\vec{q}}$ as the $(\vec{q}, b)$ - number operator $\hat{n}_{b,\vec{q}}$ which is clearly a constant of motion.

So the quantum behaviour of the system can be defined in terms of creation and destruction of bosons, here named phonons, with respect to a vacuum state $|0\rangle$. That is, we identify with $|n\rangle_{\vec{q},b}$ a (Fock) state that labels the presence of n bosons in the

$(\vec{q}, b)$ - mode each one with with energy $\hbar\omega_{b,\vec{q}}$. Since they depend on the wavevector $\vec{q}$ their existence is obviously related to existence of a Brillouin zone, hence they are also dubbed "quasiparticles". Phonons are the modes of the displacement field and the quanta of atomic vibrations. We can write the second-quantized atomic displacements as:

$$\hat{u}_{\vec{R}_i,\tau,\alpha}(t) = \sqrt{\frac{\hbar}{2N_{u.c.}M_\tau}} \sum_{b,\vec{q}} \frac{s_{b,\alpha}(\vec{q})}{\sqrt{\omega_{b,\vec{q}}}} e^{i\vec{q}\vec{R}_i} \left[e^{-i\omega_{b,\vec{q}}t} \hat{a}_{b,\vec{q}} + e^{i\omega_{b,\vec{q}}t} \hat{a}^\dagger_{b,-\vec{q}} \right], \tag{2.52}$$

where $N_{u.c.}$ is the number of unit cells. Therefore, the ground state at T = 0 K is associated with zero phonons in virtue of the third principle of thermodynamics. We can also understand that every physical phenomenon that involves lattice vibrations is associated with phonons. This will be useful when we introduce the physics of thermal transport in non metallic crystals. We can also observe that any non-harmonic term in the original DFT Energy expression that has been previously omitted, can in fact play the role of a perturbation in the system. This perturbation is accountable for the thermalisation of the system, since it makes the number operators $\hat{n}_{b,\vec{q}}$ a non conserved quantity, and of heat transport as well. Finally, the non-conservation of the phonons number beyond the harmonic theory makes the canonical ensemble an ideal choice to study the finite temperature thermodynamics.

So far we have studied the harmonic system at zero temperature. It is possible to describe the phonons at finite temperature in the canonical ensemble formalism. Let the partition function be

$$Z \equiv Tr[e^{-\beta\hat{H}}] = \prod_{\lambda} [1 - e^{-\beta\hbar\omega_\lambda}]^{-1} \tag{2.53}$$

with $\beta \equiv (k_B T)^{-1}$ and λ as shorthand for $(b, \vec{q})$. From the partition function we can derive the energy functionals and all the thermodynamical properties. The free energy reads

$$F(V,T) = -k_B T \ln(Z) = -k_B T \sum_{\lambda} \ln[1 - e^{-\beta\hbar\omega_\lambda}]^{-1} = k_B T \int d\omega D(\omega) \ln[1 - e^{-\beta\hbar\omega}], \quad (2.54)$$

where the introduced $D(\omega)$ is the phonon density of states (phDOS), that is the number of states within ε and $\varepsilon + \delta\varepsilon$ divided by $V\delta\varepsilon$. The phDOS is a regular-behaved function except for the Van-Hove singularities, i.e. those points in the BZ where the dispersion has gradient equal to zero [42]. The entropy, heat capacity at constant volume and temperature dependent mode occupation numbers for the phonon gas are, respectively:

$$S = -\left(\frac{\partial F}{\partial T}\right)_V = -k_B \int d\omega D(\omega) \left\{ \ln[1 - e^{-\beta\hbar\omega}] - \frac{\beta\hbar\omega}{e^{\beta\hbar\omega} - 1} \right\}, \quad (2.55)$$

$$C_V = T\left(\frac{\partial S}{\partial T}\right)_V = k_B \int d\omega D(\omega) (\beta\hbar\omega)^2 \frac{e^{\beta\hbar\omega}}{(e^{\beta\hbar\omega} - 1)^2} \quad (2.56)$$

and

$$n_\lambda^0 = Tr[e^{-\beta\hat{H}} \hat{n}_\lambda] = \frac{1}{e^{\beta\hbar\omega_\lambda} - 1}. \quad (2.57)$$

We can observe that $n_\lambda^0 \to 0$ for $T \to 0$ and $n_\lambda^0 \to \beta^{-1}$ for $T \to \infty$. Although the mean value of the displacement field in eq. 2.52 is clearly zero at every temperature with respect to the phonon Fock basis, we can compute the thermal mean square displacement as

$$\langle \hat{u}_{i,\tau,\alpha}(t) \hat{u}_{i,\tau,\alpha}(t)^\dagger \rangle = \frac{\hbar}{2N_{u.c.} M_\tau} \sum_{\lambda} \frac{|s_{b,\alpha}(\vec{q})|^2}{\omega_{b,\vec{q}}} (2n_\lambda^0 + 1). \quad (2.58)$$

In case we assume linear phonon dispersion - which is a reasonable choice in the long wavelength limit for acoustic modes - the previous expressions turn to be solvable in closed form. The heat capacity specifically recovers the Dulong and Petit behaviour $C_V \sim 3Nk_B$ at high temperature and shows a trend $\sim (T/T_D)^3$ close to $T = 0$ K (Debye model), where T_D is the Debye temperature defined by $k_B T_D = \hbar\omega_D$, the latter being the

Debye frequency which acts as an integration cutoff for the calculation of thermodynamic quantities.

2.4 Inter-atomic force constants

A realistic study of crystals through harmonic lattice dynamics is obviously tangled with a thorough evaluation of the IFCs introduced in eq. 2.37 and 2.38. Here we will briefly review the main two methods currently employed to get the force constants with *ab initio* accuracy, namely, the frozen-phonon (FP) method and density functional perturbation theory (DFPT). We will also show some of the most recently developed approaches to cope with either low-symmetry systems or in presence of large anharmonic effects that force us to go beyond the harmonic theory.

2.4.1 Real space method

In the FP approach [43, 44, 45, 46], the core objects that we aim to compute are the DFT inter-atomic forces through Hellmann-Feynman theorem, previously introduced in eq. 2.36. The calculation of these forces involves the electronic density only and not its derivatives with respect to atomic displacements. This method is real-space based, and it is, generally, highly sensitive to the system size. This means that large supercells involving typically ≥ 100 atoms must be considered in order to obtain numerically accurate results. The central idea of the method is to evaluate the force acting on atom-i in the minimum non-displaced energy configuration ($|\vec{F}_i^{eq.}| \leq \varepsilon$ with ε choosen to be small) and for the structure with selected atomic displacements ($\vec{F}_i^{'}$). Once these forces are known, the IFCs can be evaluated numerically as

$$IFCs_{\alpha,\beta}^{(i,j)} \approx -\frac{F_{i\beta}^{'} - F_{i\beta}^{eq.}}{\Delta_{j\alpha}} \approx -\frac{F_{i\beta}^{'}}{\Delta_{j\alpha}}, \tag{2.59}$$

where $\Delta_{j\alpha}$ is the displacement from equilibrium of atom-j along the cartesian direction α. Once the IFCs are known, it is possible to evaluate the Dynamical Matrix at all $\vec{q}$ and so the phonon properties. Crystal symmetries, where present, can be employed

in order to reduce the computational burden of the method, thence reducing the number of displaced structures that we need to consider. Clearly, this method can be easily extended to compute higher order Force Constants, at the price of increasing the computational cost. If the forces can be considered as short-ranged, it is reasonable to introduce some cutoff beyond which the IFCs are automatically set to zero, thereby reducing the number of atomic displacements to be considered. A clear drawback of this approach is the requirement of supercells larger in size than the maximum distance that allows interactions between atoms, which can be problematic in presence of long range forces [47, 48, 49].

2.4.2 Perturbation theory

In the DFPT method [50, 51, 52, 53] we evaluate the dynamical matrix directly and without passing from the Hellmann-Feynman forces. This can be done by evaluating analytically the derivatives of the forces (see eq. 2.36) at the equilibrium low-energy state

$$\Phi_{i,j} = \vec{\nabla}_i \langle \psi | \vec{\nabla}_j \hat{H} | \psi \rangle + \vec{\nabla}_i \vec{\nabla}_j E_{NN}, \tag{2.60}$$

with the electronic contribution given by

$$\vec{\nabla}_i \langle \psi | \vec{\nabla}_j \hat{H} | \psi \rangle = \int \left[\rho(\vec{r}) \frac{\partial^2 v_{ext}}{\partial \vec{R}_i \partial \vec{R}_j} + \frac{\partial \rho(\vec{r})}{\partial \vec{R}_i} \frac{\partial v_{ext}}{\partial \vec{R}_j} \right] d^3 r. \tag{2.61}$$

We can see that the knowledge of the first-order variation in the density is required. The latter can be considered as a product of the lattice displacement, to be considered as a perturbation $\delta v[\delta\rho]$ of the Hamiltonian. Thus, if we rely on the first order time independent perturbation theory, we get

$$[\varepsilon_\alpha - \hat{H}] \, |\delta\phi_\alpha\rangle = \delta v[\rho] \, |\phi_\alpha\rangle \,, \tag{2.62}$$

$$\delta\phi_\alpha(\vec{r}) = \sum_{\beta\neq\alpha} \frac{\langle\phi_\beta|\,\delta v[\delta\rho]\,|\phi_\alpha\rangle}{\varepsilon_\alpha - \varepsilon_\beta}\phi_\beta(\vec{r}) \tag{2.63}$$

and

$$\delta\rho(\vec{r}) = \sum_{\beta\neq\alpha} (f_\alpha - f_\beta)\frac{\langle\phi_\beta|\,\delta v[\delta\rho]\,|\phi_\alpha\rangle}{\varepsilon_\alpha - \varepsilon_\beta}\phi^*_\alpha(\vec{r})\phi_\beta(\vec{r}), \tag{2.64}$$

where ϕ_α, ϕ_β are non-interacting Kohn-Sham states, f_α, f_β are the single particle occupation numbers previously defined in eq. 2.24 and α, β represent wave vector and band index. Clearly eq. 2.64 must be solved self-consistently, starting from the non-displaced ground state Kohn-Sham eigenvectors and eigenvalues, since the perturbation depends on $\delta\rho$ itself. Given a crystal, instead of considering single atom displacements like in the FP method, we can make use of the periodicity of the system and assume that all the atoms are displaced from equilibrium according to $u_{\tau,\alpha} \equiv R_{\tau,\alpha} - R^0_{\tau,\alpha} = A_{\tau,\alpha}e^{i\vec{q}\cdot\vec{R}_{i,0}} + A^*_{\tau,\alpha}e^{-i\vec{q}\cdot\vec{R}_{i,0}}$.

So, by working in reciprocal space only we can obtain the dynamical matrix directly at a given phonon wave-vector $\vec{q}$:

$$D^{\tau'\beta}_{\tau\alpha}(\vec{q}) = \frac{1}{\sqrt{M_\tau M_{\tau'}}}\delta^{\vec{q}}_{\tau,\alpha}\delta^{-\vec{q}}_{\tau',\beta}E, \tag{2.65}$$

where $\delta^{\vec{q}}_{\tau,\alpha} \equiv \partial/\partial A_{\tau,\alpha}$ and $\delta^{\vec{-q}}_{\tau,\alpha} \equiv \partial/\partial A^*_{\tau,\alpha}$. This method has the advantage that we can work directly with the unit cell, thus reducing the computational cost. However, since we can only evaluate the dynamical matrix one wave-vector at the time, to get the full phonon dispersion it is common to compute D on a grid, and then get the real space IFCs through smooth Fourier interpolation. Finally we remind that the original DFPT scheme has been developed for insulators, with integer occupancy factors. The extension to the fractional f_α, f_β to study metals was introduced in [54], within a plane wave framework.

2.4.3 Stochastic and data-driven methods

Heretofore we have been focusing our attention exclusively on the second-order IFCs in the case of periodic lattices. However, it is possible to use the aforementioned methods also to evaluate higher order inter-atomic force constants and second-order IFCs for systems where the translation symmetry is broken by disorder or impurities. These calculations are pivotal if we need to go beyond lattice dynamics and consider non-harmonic effects. In these cases the minimal required number of displacements is much larger than for the Harmonic Theory and thus often numerically unfeasible for both the frozen-phonon and DFPT methods: furthermore we need to resort to large supercells, especially whilst having impurities, in order to avoid numerical artifacts due to the periodic images of the defects under periodic boundary conditions. Therefore some strategies have been adopted in the past few years to overcome these issues. We will review some of them, specifically compressed sensing [55], neural network - based approaches [56] and phonon renormalization techniques.

For those materials that present low symmetries, either because of defects or because of the presence of a considerably high number of atoms in the unit cell, a way to speed up the calculations could be the stochastic sampling of interatomic forces and displacements, to be then fitted to a low-order polynomial. Expanding the force acting on atom-i along the direction α gives

$$F_{i\alpha}(\{u_{i\alpha}\}_{1..N}) = -\sum_{j,\beta} \Phi^{ij}_{\alpha\beta} u_{j\beta} - \frac{1}{2}\sum_{j,\beta}\sum_{k,\gamma} \Phi^{ijk}_{\alpha\beta\gamma} u_{j\beta} u_{k\gamma} + O(u^3), \tag{2.66}$$

which is linear in the IFCs. We can recast the previous equation in a more compact form [55]:

$$\mathscr{F} \equiv M(u_{i\alpha})\tilde{a}, \tag{2.67}$$

where $\mathscr{F}$ comprises the set of interatomic forces, $M(u_{i\alpha})$ is the sensing matrix that

depends on the atomic displacements with constraints imposed by symmetry transformations, and $\tilde{a}$ is a vector containing a set of independent parameters which are related to the force constants by linear transformations. If we sample a supercell N_c times and collect the forces $\{f_m\}_m$ and corresponding displacements $\{u_m\}_m$, $m = 1, .., N_c$, we can extract the IFCs by minimising the following ordinary least squares (OLS) loss function:

$$\mathscr{L}(\Phi) = \sum_{m=1..N_c} [f_m - (M(u_{i\alpha})\tilde{a})_m]^2. \tag{2.68}$$

The OLS method solves an *overdetermined* systems that requires a number of forces larger than the number of parameters. However the short range nature of the interatomic interactions implies that most of the IFCs are zero. Indeed, we can recognise that although the number of degrees of freedom in eq. 2.66 scales like O(N^n) - with N being the number of atomic sites and n the order for the truncation of the expansion - the number of independent parameters of the model is much smaller because of symmetries and constraints imposed by conservation laws. Furthermore, among the independent parameters many of them are negligibly small if we consider the decay of the interaction with distance and the order of the expansion. This fact can be exploited as it makes possible to resort to compressed sensing techniques [57, 58, 6], which would require a smaller set of linear equations to retain statistical accuracy and therefore the sampling of less configurations with respect to the OLS method, thus save computational resources.

Since the number of free parameters can be very large, usually eq. 2.66 is truncated at the lowest orders and by imposing some distance cutoff. The approach devised by Eriksson et al. [55] considers also the clustering of sites to represent the symmetries of IFCs. Clusters are categorised based on the number of sites they include, so to have singlets, doublets and n-body interactions. The IFCs expansion is therefore truncated also at the cluster size level. If we assume that many or most of the IFCs are zero, we can mitigate the overfitting problems by including l_1- or l_2- norms of the solution in the loss functions:

$$\mathscr{L}(\Phi) \longrightarrow \mathscr{L}'(\Phi) = \mathscr{L}(\Phi) + \alpha|\Phi| + \beta||\Phi||^2, \tag{2.69}$$

where $\alpha = 0$ corresponds to a Ridge regression (l_1 norm) and $\beta = 0$ (l_2 norm) to the least absolute shrinkage and selection operator method (LASSO). Either method has the purpose of sending many of the IFCs to zero during the minimisation of the loss function, thus reinforcing the transferability of the result. The regularisation of the OLS is required as the solution is sparse and often contains noise factors stemming, from instance, from the cluster truncation. Cross validation techniques can assess the validity of a solution. Several non-LASSO methods can be used to regularise the OLS, like Bayesian ridge regression or recursive feature elimination to mention a few. This approach allows in principle the construction of a "force constant potential" that, after training, can predict the IFCs for several supercell structures.

2.4.4 Classical force fields and neural networks

A problem concerning quantum-based methods is the practical inability to study systems comprising more than a few hundreds of atoms in a reasonable time. This problem is reflected into the calculation of the potential energy surface, which is a fundamental quantity to predict mechanical, thermal and thermodynamical properties in materials. So it can be advisable to use classical force fields with carefully chosen parameters instead of a QM based formulation. These have the obvious advantage to be analytical functions of the atomic coordinates, hence making the full calculations of the ion dynamics much faster. However, the determination of suitable functional forms and correct parameters is hindered by the - often - complex energy landscape of the system, which makes finding optimal force fields an arduous task, usually with a poor level of transferability. Recent developments in the theory of neural networks (NN) [56, 5] are paving the way for a change in that sense. A NN - layer takes this general form:

$$y(\vec{x}; \vec{w}_l; \vec{\theta}) = \sum_{i=1..M} q_i \sigma(\vec{w}_i \cdot \vec{x} + \theta_i), \tag{2.70}$$

where σ is the neuron activation function, M is the number of neurons in the layer, $\vec{x}$ is the input vector and $\vec{W}$ and θ are the neuron weights and bias, respectively. As a consequence of Cibenko's theorem [59], with proper choices of the activation function a neural network can represent any function with compact support, given proper values to the neurons' weights: it this way, building a "good" classical force field just requires data (atomic configurations and corresponding energies and forces) but not careful choices of the functional form. Clearly being a data-driven method likewise the aforementioned kernel ridge/LASSO, crystal symmetries whenever present have to be reinforced in order to reduce the amount of data we have to feed the NN with and increase the accuracy. The procedure adopted by Behler and Parrinello (BP) consists into mapping the atomic coordinates onto descriptors - also named "symmetry functions" - that automatically fulfill the crystal symmetries, see Fig. 2.2. These symmetry functions are used to give a representation for the local environment surrounding an atom and act as an input for a set of atomic neural networks. The BP scheme defines the total energy of the system as a sum over atomic contributions:

$$E = \sum_i E_i^{NN}, \tag{2.71}$$

where the term E_i^{NN} is the energy associated with the environment surrounding the i-atom. This environment can be defined at the symmetry function level with a properly chosen cutoff function. The parameters of the NNs are then fitted to DFT (or other methods) data, thus enabling for accurate reconstructions of the PES. Several strategies have been developed to improve the description of the potential energy surface and interatomic forces for a vast genre of systems, including semiconductors, metals, molecular systems and so on, with the goal of exploring thermodynamic and transport properties. We recommend the reader the review of Behler [60] on this topic. In the context of the evaluation of interatomic force constants, in fig. 2.2 we show a phonon band structure test calculation performed with a neural network model for Ga_4P_4. We remark that the individual atomic terms in eq. 2.71 can be constructed to represent the energy of a local environment rather than a specific lattice configuration. Therefore,

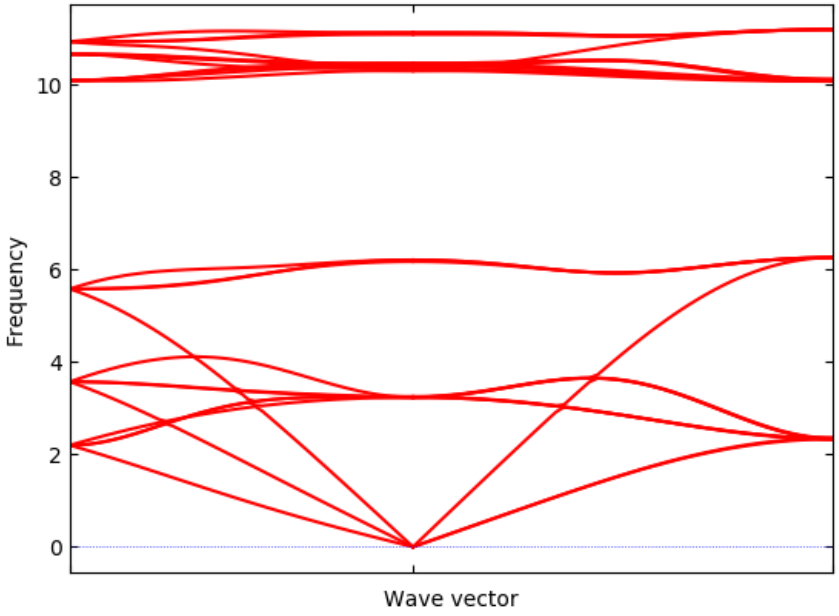

Figure 2.1: Phonon band structure of cubic Ga_4P_4 obtained via Phonopy code [1, 2] (frozen-honon approach) and neural network force field from [3, 4]. BZ symmetry points are X, Γ and L.

this approach makes possible to study the properties of embedded systems like, for example, lattice vacancies [3]) and interfaces between different structural phases [4], provided that the chemical composition used to train the network is preserved.

2.4.5 Phonon renormalization

The harmonic lattice dynamics clearly neglects non-harmonic effects or treats them in a perturbation fashion. However while representing a good approximation for the zero temperature close-to-equilibrium physics, it fails to properly represent the full ion dynamics where the non harmonic terms in the energy expansion cannot be considered small. These anharmonic terms drive phenomena like thermal expansion or structural phase transitions at finite temperature, and have been proven to be important for thermal transport as well. To cope with these effects theoretical tools like the quasi-harmonic approximation [61] were developed at first. Nevertheless, they are often

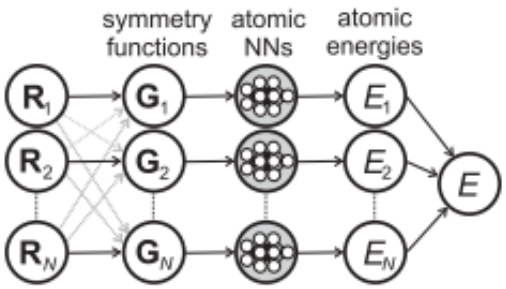

Figure 2.2: Neural network scheme from [5]. Atomic coordinates are mapped onto a set of functions that preserve the true symmetries of the systems with the goal to produce a set of atomic energies.

insufficient for their quantitative description. A way to circumvent these issues is the molecular dynamics (MD), where Newton's equation of motion are solved for the ions and ergodicity is assumed in order to extract statistical mechanical properties, at the price of neglecting the quantum character of lattice vibrations and effects related to the zero-point vibrations. To keep including the latter and at the same time retain the conceptual simplicity and analytical properties of the harmonic model, several renormalization techniques have been concocted in a way that an implicit temperature dependence is acquired by carefully modified IFCs or frequencies. A primer for the study of phonon renormalization can be found in [62]. A short list of these methods include the self-consistent phonon theory (SCPH) [63], self-consistent ab-initio lattice dynamics (SCAILD) [64], temperature dependent effective potential (TDEP) [65] and the stochastic self-consistent harmonic approximation (SSCHA) [66].

These methods assume strategies to modify either the force constants or the phonon frequencies in a way that the non-harmonic terms are implicitly captured, thus deriving renormalized interactions that can be eventually described with ordinary perturbation theory. As an example we follow the work of Tadano and Tsuneyuki in the context of SCPH [6] we can define the crystal Hamiltonian as

$$\hat{H} = \hat{H}_0 + \hat{V}_3 + \hat{V}_4 + O(\hat{V}_5), \tag{2.72}$$

where $\hat{H}_0$ includes the ordinary harmonic model and the subsequent potentials cannot be properly evaluated by mean of perturbation theory. The first order diagram associated with the self energy for the quartic term V_4 is:

$$\Sigma^4_{\vec{q},jj'}(i\omega_m) = -\frac{1}{2}\sum_{q_1}\frac{\hbar}{4\omega_{q_1}\sqrt{\omega_{\vec{q},j'}\omega_{\vec{q},j}}}\Phi(\vec{q},j;-\vec{q},j';q_1;-q_1)[1+2n(\omega_{q_1})], \tag{2.73}$$

where $q \equiv (\vec{q},j)$, $\Phi(\vec{q},j;\vec{q},j';q_1;-q_1)$ is the quartic anharmonicity in the reciprocal basis representation and $n(\omega_q)$ is the equilibrium Bose-Einstein distribution. The Dyson equation for the system Green's function (GF) reads

$$\hat{G}^{-1}(\omega) = \hat{G_0}^{-1}(\omega) - \hat{\Sigma}(\omega) \tag{2.74}$$

with the non-interacting GF given by $G_{\lambda,\lambda',0}(\omega) \equiv -2\omega_\lambda\,\delta_{\lambda,\lambda'}/(\omega^2-\omega_\lambda^2)$. Clearly the interacting GF has poles corresponding to the quasi-particle excitation where the non-harmonic terms are included. Therefore, it is straightforward that eq. 2.74 can be recast as

$$\mathrm{Det}[\omega^2 - \hat{V}_\lambda(\omega)] = 0 \tag{2.75}$$

with $V_{\lambda,\lambda'}(\omega) \equiv \omega_\lambda^2\delta_{\lambda,\lambda'} - \Sigma_{\lambda,\lambda'}(\omega)\sqrt{4\omega_\lambda\,\omega_{\lambda'}}$, and then solved self-consistently. If we assume Σ^4 to be diagonal in the polarisation index j, then eq. 2.75 can be simplified and turns to be $\Omega_q^2 = \omega_q^2 + 2\Omega_q I_q[\Omega_q]$, with I_q defined as:

$$I_q[\Omega_q] = \frac{1}{2}\sum_{q_1}\frac{\hbar}{4\Omega_{q_1}\Omega_q}\Phi(q;-q;q_1;-q_1)[1+2n(\Omega_{q_1})]. \tag{2.76}$$

The approach devised by Tadano and Tsuneyuki then uses the cubic anharmonicity in a perturbation fashion to assess the phonon lifetimes for the frequencies and polarisation vectors extracted from eq. 2.75. In particular the SCPH method is combined with the LASSO approach to extract the IFCs at high order mentioned in section 2.4.3.

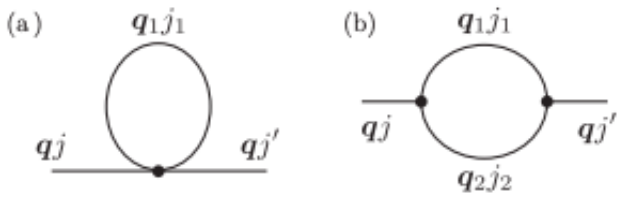

Figure 2.3: First order and second order diagrams for the quartic and cubic phonon self energies respectively reported from [6].

Another self consistent approach, namely the SCAILD method, that involves the modification of IFCs directly instead of the frequencies, can be summarised by the following steps. If we want to evaluate the IFCs at finite temperature T, we need to sample the inter-atomic forces and configurations at that T. As the DFT energy is normally evaluated at zero temperature, this means we should fit the configurations-forces data set to a low order polynomial. We can make use the quadratic nature of the Hamiltonian which implies a Gaussian shaped distribution function for the displacements. The not normalised distribution function for the interatomic displacements is

$$\hat{\rho}_{ph}(\{u_i\}_i;T) = \exp\left(-\frac{1}{2}\sum_{\vec{R},\vec{R}'}\sum_{\tau,\tau'}\sum_{\alpha,\beta}\hat{u}_{\vec{R}',\tau'\beta}B^{\vec{R}'\tau'\beta}_{\vec{R},\tau\alpha}\hat{u}_{\vec{R},\tau\alpha}\right), \tag{2.77}$$

where $B = \langle \hat{u}_{\vec{R},\tau,\alpha}(t)\hat{u}_{\vec{R}',\tau',\beta}(t)^{\dagger}\rangle^{-1}$ is the inverse of the mean square displacement matrix. We can use $\hat{\rho}_{ph}(\{u_i\}_i;T)$ to sample the configuration space of a system at finite temperature. The originally proposed SCAILD algorithm [64] assumed the classical high-T limit for the phonon distributions. Here we will explain in short the quantum version (QSCAILD) [67] that can be summarised by the following steps:

- Evaluate the small-displacements IFCs and corresponding phonon eigenvalues and eigenvectors;
- Use the small-displacements eigenvalues and eigenvectors to evaluate the displacements distribution $\rho_{ph,0}(T)$ at a finite and fixed temperature T, and use that distribution to generate random atomic displacements in the unit/supercell;

- Evaluate the DFT inter-atomic forces corresponding to those displacements and fit them to a linear model to extract the IFCs;
- Extract new eigenvalues and eigenvectors from the new IFCs and use them to build a new displacement distribution $\rho_{ph,1}(T)$. Iterate until $|\rho_{ph,n+1} - \rho_{ph,n}| \ll \varepsilon$.

Once the displacement distribution is converged, the corresponding renormalized force constants can be used to extract temperature dependent phonon properties.

2.5 Lattice impurities

In this section we are going to define and introduce the concept of lattice impurity [68]. An impurity is anything that can break the discrete symmetry of translation in a crystal. It can be an external atom introduced during the growing process of the crystal, like a substitutional or an interstitial defect, or it can be an intrinsic impurity like a vacancy, namely the removal of a regular atom, or an antisite. A short and non-comprehensive list of impurities includes:

- Vacancies, namely the complete breaking of the bonds and removal of an atom in the system;
- Interstitials, that is atoms that are added to the system in positions that are not reachable through lattice translations;
- Substitutionals, that is external atoms that replace host atoms in the crystal structure at regular positions;
- Antisites, which are swaps in the ordering of the atoms in the lattice, for non monatomic compounds. If for instance we have a binary system with atom A lying at the center of the unit cell and atom B at one corner, an antisite would reverse the A and B positions;
- Non point-like impurities, i.e. extended defects, include grain boundaries, dislocations and stacking faults;

Even if we have an ideal crystal growth, such that no external impurities have been introduced in the system, intrinsic impurities should be considered [69]. Indeed, let's take the case of a vacancy: the vacancy formation energy E_{vac} required to completely break the bonds surrounding an atom in the crystal is obviously finite. So, the Gibbs free energy corresponding to a N - atom configuration where N_{vac} - vacancies are present is

$$G = N_{\text{vac}} E_{\text{vac}} - T(S_{\text{conf.}} + S_{\text{vib.}}). \tag{2.78}$$

The configurational entropy is given by

$$S_{\text{conf.}} = k_B \ln\left(\frac{N!}{(N - N_{\text{vac}})!(N_{\text{vac}})!}\right) \tag{2.79}$$

and it is the largest contribution to the entropy at low temperatures, so that any other source of entropy (like the vibrational contribution $S_{\text{vib.}}$) can be usually neglected [70]. If we use the Stirling's approximation, $\ln(x!) \approx x\ln(x) - x$, we straightforwardly see that, at equilibrium,

$$\frac{dG}{dN_{\text{vac}}} = 0 \implies \frac{N_{\text{vac}}}{N} = \frac{1}{1 + e^{E_{\text{vac}}/k_B T}} \approx e^{-E_{\text{vac}}/k_B T} \tag{2.80}$$

when $E_{\text{vac}} \gg k_B T$. The formation energy being finite, there is a non-zero concentration of vacancies at any temperature $\neq 0$. Therefore, we can argue that - even in ideal crystal growth conditions - we cannot avoid considering impurities as their presence in the material is contemplated by thermodynamics.

Defect formation energies are of paramount importance to study defect stability and diffusion processes, but only in recent years their calculation has been made possible. Here we will inspect in details the supercell approach, while for the other techniques we send the reader to the review of Freysoldt et al. [70]. In the supercell method we generate a supercell out of the unit cell of a certain material. Once we have

computed the energy of the pristine system, we cast an impurity inside it. Naively one could expect the formation energy of the defect to be given by the difference between the energy of the doped structure and the pure one. However, several errors are introduced within this methodology that requires the application of correction terms. In the case of charged defects, the periodic boundary conditions allow for the presence of a $\sim 1/r$ Coulomb-like interaction between a dopant and its periodic image, which is as strong as the supercell is small. Since we are usually interested in the study of the low-concentration limit, this interaction - hereafter named Makov-Payne term or E_{MP} [71] - has to be removed from the computation of the total energy of the doped structure. Furthermore, the Kohn-Sham eigenvalues and eigenstates depend on the cell-averaged electrostatic potential, whose zero value is affected by the addition of impurities: therefore, the need to align the potentials in order to have a common zero for the energies [72]. Finally, common DFT functionals like LDA or GGA - albeit of fast numerical evaluation - present an electronic band structure that is often inconsistent with measurements and thus require a correction ΔE_{gap} to the electronic gap of the pristine system. This term can be obtained either empirically or with the aid of more thorough methods, like for example GW, hybrid functionals and modified pseudopotentials [73]. Altogether, the three correction terms must be summed, leading to

$$E_{corr} = E_{PA} + E_{MP} + \Delta E_{gap}, \tag{2.81}$$

where the potential alignment term is defined by the difference of the averaged electrostatic potential energies between doped and pristine supercell, namely $E_{PA} = q[V_{q,def} - V_{pr.}]$, and the Makov - Payne multipole correction E_{MP} is defined by

$$E_{MP} = \frac{q^2 \alpha_M}{2\varepsilon L} + \frac{2\pi q Q}{3\varepsilon L^3} + O(L^{-5}). \tag{2.82}$$

Here q is the charge of the defect, ε is the static dielectric constant which screens the Coulomb potential inside the crystal, α_M is the Madelung constant, Q is the quadrupole

moment and L^3 is the volume of the supercell. The Makov - Payne term is smaller when the system size is large. Concerning ΔE_{gap}, a common strategy for its assessment consists into evaluating the corrections to the VBM and CBM energies - namely $\Delta\varepsilon_{VBM}$ and $\Delta\varepsilon_{CBM}$ - and then take $\Delta E_{gap} = q\Delta\varepsilon_{VBM}$, with the further assumption that the Fermi level of the doped system can range within the corrected gap. Finally, considering also E_{corr}, the formation energy for a defect D_q of charge q is:

$$\Delta E_{form.}[D_q;\varepsilon_F] = E_{D_q} - E_{prist.} + E_{corr} + \sum_i n_i(\mu_i^0 + \Delta\mu_i) + q\varepsilon_F, \tag{2.83}$$

where E_{D_q} ($E_{prist.}$) is the DFT-computed energy for the defect-laden (pristine) system, ε_F is the Fermi level, μ_i^0 is the chemical potential for the i-specie in a reference stable configuration (e.g. O_2 for air oxygen or S_8 for solid sulphur, usually evaluated at ambient pressure and temperature), and $\Delta\mu_i$ takes into account the synthesis conditions and the exchange of atoms between the bulk crystal and the reservoirs. Here we adopt the convention $n_i \geq 0$ ($n_i \leq 0$) when atoms are removed from (added to) the crystal. In case charged impurities are considered, we must also include the energy cost for adding/removing an electron, here represented by the Fermi level (which plays the role of chemical potential for the electrons). Several constraints must be imposed on the chemical potentials $\Delta\mu_i$ in order to keep the crystal structure stable and avoid possible competing phases. For example, if we have a binary crystal AB with heat of formation ΔH_{AB}, we shall impose

$$\Delta\mu_A + \Delta\mu_B = 2\Delta H_{AB} \tag{2.84}$$

along with $\Delta\mu_A \leq 0$ and $\Delta\mu_B \leq 0$ so that A and B do not precipitate to their reference phases. If A and B can form a competing phase A_aB_b with $a, b \neq 1$, we have to set a further bound on the chemical potential, that is

$$a\Delta\mu_A + b\Delta\mu_B \leq (a+b)\Delta H_{A_aB_b}. \tag{2.85}$$

If for example we dope Si with P, along with $\Delta\mu_{Si} \leq 0$ we need to consider $\Delta\mu_{Si} + \Delta\mu_P \leq 2\Delta H_{SiP}$ and $\Delta\mu_{Si} + 2\Delta\mu_P \leq 3\Delta H_{SiP_2}$ in order to avoid both the formation of SiP and SiP_2. It shall be noticed that the reference chemical potential for a specie in the pure phase depends on pressure (p) and temperature (T) [70]. While these dependencies can generally be neglected for solid phases without loss of accuracy, they are important for elements in the gaseous state. Thus, we can resort to the parametrized Shomate equation [74] to evaluate the p-T dependent chemical potential for species in the gas reference phase.

Charged impurities affect the position of the Fermi level in semiconductors by introducing energy levels inside the gap and can either shift it towards the VBM or the CBM depending on their acceptor/donor nature. The total charge in the system given by the amount of holes p minus the amount of negative carriers n must be zero, either in the pristine system and the presence of doping, at all temperatures. Thence, we have

$$p(\varepsilon_F, T) - n(\varepsilon_F, T) = N_A^- - N_D^+, \tag{2.86}$$

where N_A^- and N_D^+ are the concentration of ionised acceptors and donors in the system. Hole and electron concentrations can be expressed as

$$p(\varepsilon_F, T) = \int_{-\infty}^{\varepsilon_{\text{VBM}}} D(\varepsilon)(1 - f(\varepsilon; \varepsilon_F, T))d\varepsilon \tag{2.87}$$

and

$$n(\varepsilon_F, T) = \int_{\varepsilon_{\text{CBM}}}^{\infty} D(\varepsilon) f(\varepsilon; \varepsilon_F, T) d\varepsilon, \tag{2.88}$$

where $D(\varepsilon)$ is the electron/holes density of states (eDOS, pDOS) and

$$f(\varepsilon; E_F, T) = \frac{1}{\exp((\varepsilon - \varepsilon_F)/(k_B T)) + 1} \tag{2.89}$$

is the Fermi-Dirac distribution. A useful approximation can be made in order to obtain an analytical expression for p and n. If we fit the electronic DOS near the VBM/CBM with a parabolic band model and we consider $|\varepsilon_F - \varepsilon_{CVM/VBM}| \gg k_B T$, we can obtain

$$p(\varepsilon_F, T) = 2\left(\frac{2\pi m_h^* k_B T}{h^2}\right)^{3/2} e^{-\frac{\varepsilon_F - \varepsilon_{VBM}}{k_B T}} \tag{2.90}$$

and

$$n(\varepsilon_F, T) = 2\left(\frac{2\pi m_e^* k_B T}{h^2}\right)^{3/2} e^{-\frac{\varepsilon_{CBM} - \varepsilon_F}{k_B T}}, \tag{2.91}$$

with the spin degeneracy factor taken into account. The parameters m_h^* and m_e^* are the effective masses for holes and electrons respectively, and can be fitted for example to the DFT density of states or the band structure near the VBM/CBM. In the further case shallow impurities - that is dopants which energy levels lie very close to the VBM/CBM and thus are easy to ionise - are considered, the effective masses can be estimated with an hydrogenic mass model [75, 76, 68]. In presence of external dopants and considering eq. 2.80, the charge neutrality is given by

$$p(\varepsilon_F, T) - n(\varepsilon_F, T) - \sum_{D_q} e^{-\Delta E_{form.}[D_q;\varepsilon_F]/k_B T} + \Delta N_{def} = 0, \tag{2.92}$$

where ΔN_{def} accounts for defects that are introduced in non-equilibrium conditions between the crystal and the reservoirs. The relation between impurity concentration, temperature and Fermi level drives electronic and atomic diffusion processes inside the crystal when an external field is set on. Whenever there is a concentration gradient $\vec{\nabla} C$, a flux of particles $\vec{J}$ arises according to Fick's law [77]:

$$\vec{J} = -D\vec{\nabla} C, \tag{2.93}$$

where D is the diffusion coefficient. If we include the local conservation of particles and assume a delta-like behaviour for the concentration at time $t = 0$, namely $C(\vec{x},0) = \delta(\vec{x}-\vec{x}_0)$, we can prove that

$$C(\vec{x},t) = \left(\frac{1}{2\pi Dt}\right)^{3/2} \exp\left(\frac{\vec{x}^2}{2Dt}\right). \tag{2.94}$$

We can classify the diffusion processes by evaluating the α - exponent of $\langle \vec{x}^2 \rangle / t \sim t^{\alpha}$. The $\alpha = 0$ case correspond to normal diffusion while $\alpha > 0 (< 0)$ to the super(sub)diffusive case.

The presence of vacancies can activate diffusion processes even in a solid crystal, as the space freed by the removed atoms can be occupied by their neighbours. This can favour the inclusion of substitutional impurities if an external reservoir is coupled to the system. Similarly, also interstitials are free to diffuse due to their reduced size. Specifically, the rate R at which impurities can flow in a crystal is intimately related to both the activation free energy ΔG_m^v - that is the energy barrier an atom needs to cross in order to occupy a neighbour vacant site - and the vacancy formation energy ΔG_{vac} [69]. Indeed, the diffusion rate can be considered as proportional to the product between the probabilities of vacancy formation and activation barrier crossing. We can take an Arrhenius law $R \equiv 1/\tau \propto \exp(-(\Delta G_m^v + \Delta G_{vac})/k_B T)$, where τ is the time required for the system to reach stationary conditions. Given the variance of the diffusion process $\langle \vec{x}^2(\tau) \rangle = 6D\tau$ - with $\sqrt{\langle \vec{x}^2(\tau) \rangle}$ approximated by the (average) lattice constant a - we straightforwardly obtain that:

$$D = D_0 \exp\left(\frac{-\Delta G_m^v + \Delta G_{vac}}{k_B T}\right), \tag{2.95}$$

where D_0 is a material-dependent constant. The last equations unveil the role played by formation energies into the vacancy-driven diffusion process inside crystals. We should note that a similar equation holds in the case of interstitials, with the important difference that we do not need to consider the vacancy formation energies at all in this case as they always have room to diffuse once they are in the system.

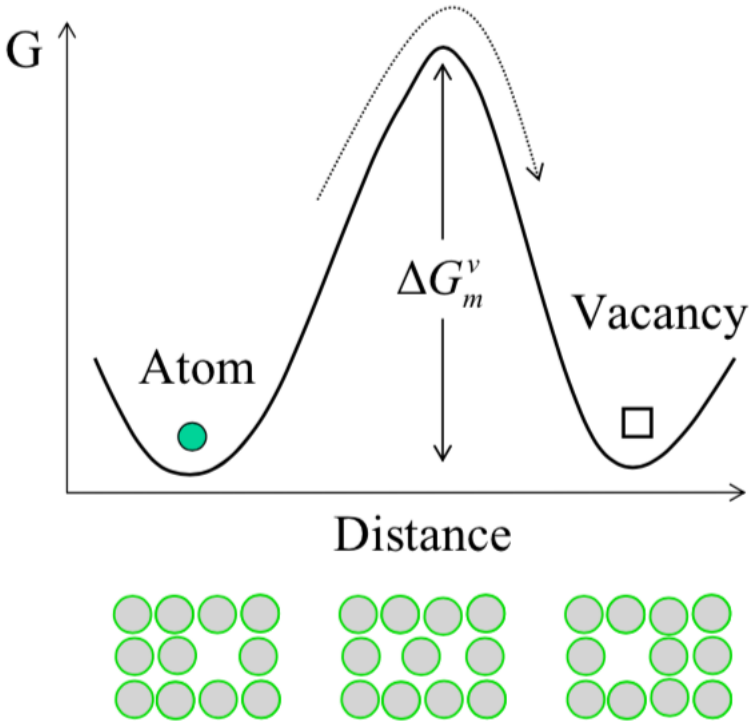

Figure 2.4: Free energy as a function of distance for a vacancy with ΔG_m^v as the activation energy barrier.

2.6 Chapter overview

In this chapter we have introduced basic concepts in solid state physics like the Brilluoin zone (BZ) and the Bloch's theorem. We have given an overview on density functional theory (DFT) and the Born-Oppenheimer approximation used to solve the electronic problem in crystals with first principles accuracy and to effectively decouple the ions and electrons motions. We have shown the concept of normal modes of lattice vibration and their quantum counterpart - i.e. phonons - and the methods that can be used to extract their properties from DFT calculations. In the end we have presented the thermodynamics of defects, showing how to compute *ab initio* their formation energies. We have introduced the concept of electronic charge neutrality which will be important to justify part of our results on doped boron arsenide in chapter 5. In the next chapter, we explain the theory of thermal transport within the linear response and Boltzmann equation theories and we derive the expressions for the phonon scattering rates and thermal conductivity that have been used throughout this thesis.

3

Theory of thermal transport

Let us suppose that we couple a semiconducting crystal to two thermal baths at different temperatures T_1 and T_2. Thermodynamics predicts that a heat flow from the hotter to the colder end of the crystal will be established in order to reinstate thermal equilibrium and a temperature gradient will form. This basic phenomenon of thermal conduction is mathematically expressed by means of the Fourier's law:

$$\vec{J} = -\kappa \vec{\nabla} T, \tag{3.1}$$

where $\kappa \geq 0$ is the crystal thermal conductivity and $\vec{J}$ is the heat per unit time that crosses a unit surface in the material. As soon as a thermal gradient is formed, the amount of heat that traverses the crystal along a particular direction is given by κ. Therefore, to predict and understand the thermal properties of a material it is of paramount importance to model its thermal conductivity. In a crystal the main carriers of heat are phonons and electrons. If we exclude metals from our analysis we can consider the heat flux mainly as being a phonon flow, with a smaller electronic contribution only in the case of highly doped semiconductors. Starting from the relation

$$\delta Q = C dT, \tag{3.2}$$

where δQ is the heat exchanged between the crystal and the reservoir and C is the heat

capacity, we can infer the following relationship:

$$\kappa \sim Cv\langle l \rangle, \tag{3.3}$$

where v and $\langle l \rangle$ are respectively the velocity and the "mean free path" (MFP) of the carriers, i.e. the average distance a phonon or electron can run through before being scattered by the lattice or by impurities. Although eq. 3.3 is too simple to be of actual use for accurate predictions, it clearly shows that a large heat capacity, carrier velocity and MFPs are required to reach a high κ. Thus, scattering mechanisms should be minimised to achieve the last requirement and in the case of phonons as carriers, stiff bonds and small atomic masses (in the monatomic lattice case) should be preferred in order to get high carrier velocities. Analogously, high electron velocity can be achieved for small effective masses in the case of metals.

In this chapter we highlight several techniques that permit the calculation of κ starting from first principles, with particular reference to the case of phonon transport. At first we delve into linear response theory and explain the Onsager relations. Then we study several scattering mechanisms that can influence the phonon MFP and the conductivity with a look to both modern theory and historical perspective. Particular attention is devoted to scattering processes induced by impurities, being the main core of this thesis. Finally we derive the Boltzmann equation in low-field conditions, explaining strategies to achieve its numerical solution.

3.1 Linear response theory

Let us assume we want to compute transport properties in a macroscopic system, for temperatures well above the Debye temperature T_D so that quantum effects can be effectively neglected: the size of the system, combined with a non-equilibrium framework, usually prevents us from applying equilibrium statistical mechanics, since concepts like thermodynamic pressure and temperature are ill defined. Therefore, many approaches have been developed to treat transport properties in the case of small

deviations from equilibrium: linear response theory (LRT) is one of these methods as it allows us to study how external effects influence physical properties of systems at the lowest order in perturbation theory. One of the goals of LRT is to have the system response to a small external perturbation fully computed by statistical mechanics, thus avoiding the non-equilibrium framework.

3.1.1 Onsager and classical Green-Kubo relations

Establishing a heat flow inside a material requires the presence of a temperature gradient. Thus, we may ask how to study space-dependent thermal fields within a thermodynamic framework, where T is a uniquely defined ensemble property. A simple and insightful approach could be to partition our system into sub-ensembles inside which local equilibrium and thermodynamics still hold. We should also take the size of these sub-ensembles to be much smaller than the system volume to ensure the applicability of a field based description. Assuming that this can be done we can obtain a description of a macroscopic system - under local equilibrium conditions - by using extensive thermodynamic variables that can be expressed as integrals over space of well defined densities:

$$A_i[V] = \frac{1}{V}\int a_i(\vec{r})d^3r, \tag{3.4}$$

where A_i is a generic extensive variable and a_i is its associated position-dependent density. Local equilibrium ensures a local conservation law for these densities:

$$\frac{\partial a_i(\vec{r},t)}{\partial t} = -\vec{\nabla}\cdot\vec{J}_i(\vec{r},t). \tag{3.5}$$

It comes natural to ask ourselves what the relationship between macroscopic fluxes of these variables and driving external forces may be. First of all we need a definition for these driving forces. Starting from the first law of thermodynamics we know that, at fixed volume, the following relationship among entropy density, internal energy density and mass density holds:

$$ds = \frac{1}{T}du - \frac{\mu}{T}d\rho, \tag{3.6}$$

where $1/T$ and μ/T are intensive variables, T is the thermodynamic temperature and μ is the chemical potential. If we consider that microscopic processes could be irreversible, the local conservation law for entropy would be

$$\frac{\partial s(\vec{r},t)}{\partial t} + \vec{\nabla}\cdot\vec{J}_s(\vec{r},t) = \left(\frac{\partial s(\vec{r},t)}{\partial t}\right)_{irr.}, \tag{3.7}$$

where the r.h.s. term accounts for irreversible processes that lead to a local violation of the entropy conservation. If we assume we have both a temperature and a density gradients $\vec{\nabla}T$ and $\vec{\nabla}\rho$ - with $|\delta T| << T$ and $|\delta\rho| << \rho$ - the system will experience both energy and matter fluxes $\vec{J}_u$ and $\vec{J}_\rho$, according to eq. 3.1 and Fick's law [77] introduced in the previous chapter:

$$\vec{J}_\rho = -D\vec{\nabla}\rho, \tag{3.8}$$

where D is the material diffusion coefficient. We can also re-write Fourier and Fick's laws as $\vec{J}_u = -kT^2\vec{\nabla}(1/T)$ and $\vec{J}_\rho = D^*\vec{\nabla}(-\mu/T)$, where D^* depends on the thermodynamic state variables, but not on their space gradients and time derivative. In particular the second equation holds in a linear approximation as the chemical potential increases monotonically w.r.t. the mass density when T is kept fixed. Furthermore either a gradient in the chemical potential or temperature can produce a gradient in density. Clearly the thermal and diffusion coefficients do not depend on the gradients as both equations 3.1and 3.8 hold in a linear approximation. We identify these two gradients as the aforementioned thermodynamic forces. Therefore we can immediately see a connection between fluxes of extensive variables and variation of intensive properties, with the latter being the driving fields. We also stress that Fourier and Fick's laws in this context hold in a local sense.

If we take into account heat and mass transport as coupled problems, we can write

$$\vec{J}_u = B_{11}\vec{\nabla}(1/T) + B_{12}\vec{\nabla}(-\mu/T) \equiv \sum_j B_{1j}\vec{\nabla}\Phi_j \tag{3.9}$$

and

$$\vec{J}_\rho = B_{21}\vec{\nabla}(1/T) + B_{22}(-\mu/T) \equiv \sum_j B_{2j}\vec{\nabla}\Phi_j. \tag{3.10}$$

We can now use the first law of thermodynamics in form of eq. 3.6 to write the entropy flux as

$$\vec{J}_s = \frac{1}{T}\vec{J}_u - \frac{\mu}{T}\vec{J}_\rho, \tag{3.11}$$

and if we consider the local conservation laws for energy and mass densities, it is straightforward to prove that

$$\left(\frac{\partial s(\vec{r},t)}{\partial t}\right)_{irr.} = \sum_{i,j=1,2} B_{ij}\vec{\nabla}\Phi_i \cdot \vec{\nabla}\Phi_j. \tag{3.12}$$

The matrix containing the transport coefficients B_{ij} clearly has to be positive definite to satisfy the second law of thermodynamics. The aforementioned argument can be easily generalised in presence of every gradient of intensive thermodynamic variables. If we take both space and time Fourier transform of eq. 3.5 and assume that the time derivative of the densities can be expressed as a linear combination of densities ("weak" deviation), this leads to:

$$\vec{J}_i(\vec{q},\omega) = i\frac{\vec{q}}{q^2}\sum_j \Lambda^{ij}(\vec{q},\omega)a^j(\vec{q},\omega), \tag{3.13}$$

and since we assume local equilibrium, we also need to take the Lambda to vanish in the long-wavelength limit, i.e. $\Lambda^{ij}(\vec{q}\to 0,\omega)\to 0$. Therefore it is reasonable to write

the Lambda matrix expression as $q^2\lambda^{ij}$ in the static $\omega \to 0$ limit, meaning that the macroscopic flux of the i$^{\text{th}}$ variable can be defined as

$$\vec{J}_i[V] = \sum_j \lambda^{ij}\vec{\nabla}A_j[V]. \tag{3.14}$$

As before, for each extensive variable A_i we can define an intensive variable $x_i \equiv \partial S/\partial A_i$ and a susceptibility $\chi^{ij} \equiv (1/V)(\partial A^i/\partial x^j)$. If we define the i$^{\text{th}}$-thermodynamic force $\vec{F}_i$ as the integral over space of the gradient of the intensive variable (density), normalized with the system volume, we can obtain:

$$\vec{J}_i = \sum_k (\sum_j \lambda_{ij}\chi^{jk})\vec{F}_k = \sum_k L_{ik}\vec{F}_k. \tag{3.15}$$

That is, the thermodynamic macroscopic response of a system is given by some coefficients and by "forces" derived from gradients of intensive variables. We recognise these coefficients to be the matrix elements B_{ij} previously identified in the specific case of coupled heat and mass transport. Near equilibrium we can assume a quadratic relation between entropy and extensive variables

$$S(\{A_i\}_i) = -\frac{1}{2}\sum_{i,j}\alpha_{i,j}(A_i - A_{i,eq})(A_j - A_{j,eq}) \tag{3.16}$$

with α_{ij} being positive definite, and we can also assume that at the microscopic level the time reversal symmetry (TRS) holds true, namely $\langle A_i(t)A_j(t+\tau)\rangle = \langle A_j(t)A_i(t+\tau)\rangle$. The probability density for the macroscopic variables $f \sim \exp(S/k_B)$ is clearly Gaussian and this prompts us to derive the following relation:

$$\langle A_i x_j\rangle = -k_B\delta_{ij}. \tag{3.17}$$

Using eq. 3.17 along with a linear evolution for the extensive variables - $\dot{A}_i = \sum_j L_{ij}x_j$ - (see eq. 3.13) and the microscopic TRS leads to the Onsager reciprocal relations [78, 79]:

$$L_{ij} = L_{ji}. \tag{3.18}$$

We can also note that as long as the evolution of the A_is is linear in the intrinsic variables and eq. 3.17 and microscopic TRS are valid, the Onsager matrix is even. Thus it is not explicitly required to have a quadratic entropy although it is a reasonable choice close to equilibrium, which is the regime usually probed by linear response theory. An extension of the Onsager relation to vector and tensor quantities has been given by [80, 81].

We now give a formulation of the thermal transport coefficients in terms of microscopically defined variables, following the argument of [82]. Let us consider a classical N-body system, such that the Hamiltonian H_0 can be written in the kinetic + potential energy form. We can add a small one-particle external perturbation coupled with some intensive variable density a_i of the system, i.e.

$$V_{ext}(\Gamma,t) = \sum_i \int v_i(\vec{r},t) a_i(\vec{r},\Gamma) d^3r, \tag{3.19}$$

where $\Gamma \equiv \{\vec{P}_i, \vec{R}_i\}$ denotes the many-body phase space state and i runs over atomic indices. To understand how a physical observable $B(\Gamma)$ changes because of the perturbation we need to compute $\delta B = B(V_{ext}) - B_0$. Expanding $B(V_{ext})$ in powers of V_{ext} and taking only the first order term give us

$$\delta B = -\beta \int e^{-\beta H_0(\Gamma)} B(\Gamma) V_{ext}(\Gamma,t) d\Gamma = \sum_i \int \left(\int e^{-\beta H_0(\Gamma)} B(\Gamma) a_i(\Gamma,\vec{r}) d\Gamma \right) v^i(\vec{r},t) d^3r. \tag{3.20}$$

Local conservation law for the i-density and a little integral manipulation allow us to get the Green-Kubo (GK) [83, 84, 85] formula:

$$\delta B(\vec{r},t) = -\beta \sum_{i,\alpha} \int \left[\int_{-\infty}^{t} \langle B(\Gamma_t) J^i_\alpha(\Gamma_{t'}) \rangle_0 dt' \right] \partial_\alpha v^i(\vec{r}',t') d^3r', \tag{3.21}$$

where $\langle\rangle_0$ indicates a thermal average over H_0. Assuming $\delta B(\vec{r},t) = J^h_\gamma(\vec{r},t)$, the expression of the heat flux density can be straightforwardly derived. Integration of the flux density over space, space-time homogeneity and the $t \to \infty$ limit give us again an Onsager-like relation where thermodynamic forces are substituted by derivatives of the v_is terms. The TRS symmetry of the correlation functions ensures the validity of the reciprocal relation $L_{ij} = L_{ji}$:

$$\vec{F}^i(\Gamma_{t'}) = \frac{1}{VT}\int \vec{\nabla} v^i(\vec{r},t')d^3r, \tag{3.22}$$

$$\vec{J}^i(\Gamma) = \frac{1}{V}\int \vec{J}^i(\vec{r},t)d^3r, \tag{3.23}$$

$$L_{ij} = \frac{V}{k_B}\int_{-\infty}^{\infty} \langle \vec{J}_i(\Gamma_t) \otimes \vec{J}_j(\Gamma_0)\rangle_0 dt, \tag{3.24}$$

and

$$\Rightarrow \vec{J}_\alpha = \sum_\gamma L_{\alpha\gamma}\vec{F}_\gamma. \tag{3.25}$$

Clearly the previously introduced Onsager coefficients L_{ij} describe the linear response of the system due to external forces. At this point it should be noted that the hereto defined linear theory is valid when both the unperturbed Hamiltonian and the external driving field can be defined at the microscopic level. As temperature has only a statistical ensemble definition, we need some "trick" in order to apply the linear response theory to the heat transport problem. Let's assume that our system, initially at equilibrium, is now in contact with some heat reservoirs such that a temperature field $T(\vec{r}) = T_{eq} - \delta T(\vec{r})$ (with $\delta T << T_{eq}$) arises. Again, we stress that local equilibrium means that each sub-ensemble of our system is characterized by a certain $T(\vec{r})$ although the deviation from T_{eq} is small enough to be treated in a perturbation fashion. The canonical ensemble density takes the form:

$$e^{-\beta H(\Gamma)} \longrightarrow e^{-\int \beta(\vec{r}) e(\Gamma,\vec{r}) d^3 r}, \tag{3.26}$$

where $e(\vec{r},\Gamma)$ is the energy density and $\beta(\vec{r}) = \beta(1+\delta T(\vec{r})/T + O(1/T^2))$. If we take only the first order in $1/T$ and we put the β-expression inside the density expression we obtain $\rho(\Gamma) \propto \exp\{-\beta(H+V)\}$, with $V(\Gamma) \equiv \int e(\Gamma,\vec{r})\delta T(\vec{r}) d^3 r/T$. Having the temperature variation as driving field we can apply the GK formula and get the Fourier's law, with

$$\kappa_{ij} = \frac{L_{ij}}{T^2} \geq 0. \tag{3.27}$$

3.1.2 Heat flux

The computation of the thermal conductivity requires an expression for the heat flux with respect to phase space coordinates. This can be achieved by performing the space integration of the local energy conservation. As the integration by part leads to the evaluation of the flux at the boundary of the system - where it is generally non-zero because of the periodic boundary conditions - we can evaluate the conservation law in the Fourier space, perform a Taylor expansion at finite wavelength (taking only the first order in $\vec{q}$) and finally take the infinite volume limit [82]. Assuming to take the form $\sum_n e_n(\Gamma)\delta(\vec{r}-\vec{R}_n)$ for the energy density with $e_n = \vec{P}_n^2/2m_n + V_n$, an expression for the heat flux is finally derived:

$$\vec{J} = \frac{1}{V}\sum_n e_n \vec{v}_n + \sum_n \sigma_n \vec{v}_n \equiv \vec{J}_c + \vec{J}_v, \tag{3.28}$$

where σ_n is the individual-n atom stress tensor. The "c" part of the flux (so called "convective") is mostly related to thermal transport through the motion of the atomic/molecular constituents of the system and it is relevant for fluids, while the "v" part ("virial") is related to lattice vibrations. It can be noticed that in the case of solids the convective part is many orders of magnitude smaller than the virial part, so that it can be sent to zero without loss of accuracy.

We stress that this definition of heat flux assumes a well defined partition of the energy density into individual atomic components. This assumption can hold for classical systems but does not stand rigorously from a DFT perspective. Furthermore the relationship between heat flux and thermal conductivity is not unique. Indeed, if we define two energy densities $e(\vec{r},t)$ and $\tilde{e}(\vec{r},t)$ so that:

$$e(\vec{r},t) - \tilde{e}(\vec{r},t) = \vec{\nabla} \cdot \vec{p}(\vec{r},t), \tag{3.29}$$

where $\vec{p}$ is a bounded vector field and $\vec{P}(t) \equiv \int \vec{p}(\vec{r},t) d^3r/V$, we get

$$\vec{\tilde{J}}(t) = \vec{J}(t) + \vec{\dot{P}}(t), \tag{3.30}$$

that is, the two macroscopic fluxes differ by the total time derivative of a bounded vector. It can be proven that the two representations give different heat auto-correlation functions but the same thermal transport coefficients. This means they are physically equivalent, i.e. they belong to the same *gauge*. This has profound implication on the theory of thermal transport as it implies that the GK heat flux is gauge dependent (i.e. non-physical), though the measurable thermal conductivity clearly is not. This phenomenon is akin to the reason why the macroscopic polarisation in dielectric crystals is ill defined [86] and it can be exploited to provide a formulation for the energy density in the DFT framework [82]. Finally, and in spite of the previous discussion about the non-uniqueness of $\vec{J}$, we stress that the expression for the virial term $\vec{J}_v$ is anyway always well defined in DFT and thus can be used for crystalline solids where the convective contribution is negligible [87].

Albeit being well defined, several problems can arise during the numerical evaluations of thermal coefficients with the GK theory: first of all, in crystalline solids the short-range nature of interactions and the strength of anharmonic effects at high temperature lead to large self-correlation times, of the order of nanoseconds, thus preventing an

extensive use of *ab initio* techniques - like molecular dynamics - to probe the phase space. Moreover, the numerical evaluation is highly sensitive to either the finite size of the simulated system and to the initial condition of the MD simulation and requires careful volume convergence tests and averages over different initial conditions.

For all practical purpose the numerical evaluation of the thermal conductivity via GK involves computing the heat current auto-correlation function (HCAF), a task that is performed via integration over finite molecular dynamics (MD) simulations:

$$C_{\alpha\beta}(\tau) = \frac{1}{T_{MD} - \tau} \int_0^{T_{MD}-\tau} \vec{J}_\alpha(t+\tau) \otimes \vec{J}_\beta(t) dt, \tag{3.31}$$

where T_{MD} is the length of the MD simulation. Hence it can be expected that when τ approaches T_{MD} this would lead to a rather poor evaluation of the HCAF. Since we can expect $C_{\alpha\beta}(\tau) \longrightarrow 0$ after a certain value of τ, we can impose a cutoff τ_c to regularise the solution. In practice using $T_{MD} \sim 10\tau_c$ is generally required to obtain a reliable convergence of the conductivity w.r.t. the simulation length and before it starts being overcome by numerical noise:

$$k_{\alpha\beta} = \frac{V}{k_B T^2} \int_0^{\tau_c} C_{\alpha\beta}(\tau) d\tau. \tag{3.32}$$

Several strategies to mitigate the HCAF errors have been devised in the recent years to find τ_c rigorously. We mention the work of Chen et al. [88] who proposed a double exponential fitting of the autocorrelation function for crystalline Si and Ge and a criterion for the cutoff time, which is identified as the moment when the HCAF error and mean are equal. The double exponential is phenomenologically justified as it takes into account the large span in the magnitude of phonon relaxation times.

A more recent approach summarised in [82] makes use of the Gaussian nature of the equilibrium heat flux in diffusive processes and applies statistical information based criteria on the so called signal "cepstral" coefficients (discrete Fourier transform of the log - "periodograms", i.e. the spectral coefficients). This has been proven useful

to reduce the error and the computational cost of the simulations in several liquid systems.

While the previous analysis focuses on the application of equilibrium methods - namely equilibrium molecular dynamics (EMD)- the (classical) evaluation of the thermal conductivity in a crystal can also be computed with non-equilibrium tools like the non-equilibrium molecular dynamics (NEMD) [89] where either an energy flux or a temperature gradient is artificially imposed onto the crystal and then the conductivity can be evaluated as $\kappa = |\vec{J}|/|\vec{\nabla}T|$. Applications of this method can be found in [90, 91] where it has been used to study the effect of impurities in Si nanostructures and to extract the conductivity of MgO. A comparison between NEMD and EMD has been recently performed by [92].

We finally remind that the GK and other MD based approaches can be applied even in the case of systems where the translation symmetry is broken, as in glasses or disordered materials. Clearly the numerical and statistical errors are much more negligible within the harmonic theory where the quantum mechanical nature of the heat carriers can be evaluated and analytical expressions can easily be derived. This has prompted the solution of the Green-Kubo formula for disordered systems within the harmonic approximation as a model of thermal transport in disordered materials. Pioneering works on this topic can be found in [93, 94].

3.2 Boltzmann transport equation

If we consider a classical N-particle system in presence of conservative forces, the conservation of the phase-space volume leads to the conservation of the system distribution function $\rho(\{\vec{R}_i\}_{i=1..N}, \{\vec{P}_i\}_{i=1..N}, t)$, a result known as Liouville's theorem [95]. The main achievement of this theorem is the description of how the distribution function of the system evolves in phase space: if we consider a finite volume $d\Gamma \equiv d^N p d^N r$ the explicit variation $\partial\rho/\partial t$ is given by the flux of trajectories that flow continuously and smoothly in and out Γ. Since ρ is a function of 6N degrees of freedom in 3D we seek a description of our system in terms of a single particle distribution $f(\vec{p}, \vec{r}, t)$.

Intuitively, f is not expected to be a conserved quantity when inter-particle interactions are present: indeed, the latter may create or destroy single particle states discontinuously and non-smoothly via scattering mechanisms, thus acting like a source or sink for degrees of freedom. Given that

$$N = \int d^3P_1 ... d^3P_N \int d^3R_1 ... d^3R_N \rho(\{\vec{R}_i\}_{i=1..N}, \{\vec{P}_i\}_{i=1..N}, t), \tag{3.33}$$

it is natural to define f by integrating ρ over all degrees of freedom minus one, namely

$$f(\vec{P}, \vec{R}, t) \equiv \int d^3P_1 ... d^3P_{N-1} \int d^3R_1 ... d^3R_{N-1} \rho(\{\vec{R}_i\}_{i=1..N}, \{\vec{P}_i\}_{i=1..N}, t), \tag{3.34}$$

meaning that

$$N = \int d^3P \int d^3R f(\vec{P}, \vec{R}, t). \tag{3.35}$$

Clearly the total number of degrees of freedom N is a conserved quantity, thus the total variation of f w.r.t. time has to be zero. If we consider a two-body interacting Hamiltonian:

$$H = \sum_i \frac{\vec{P}_i^2}{2m_i} + \frac{1}{2} \sum_{i,j} V(\vec{R}_i, \vec{R}_j) \tag{3.36}$$

we can write

$$\frac{df(\vec{P}_1, \vec{R}_1, t)}{dt} = \int d^3P_2 ... d^3P_N \int d^3R_2 ... d^3R_N \left[\frac{\partial \rho}{\partial t} + \frac{\partial \rho}{\partial R_1} \dot{R}_1 + \frac{\partial \rho}{\partial P_1} \dot{P}_1 \right] \equiv 0. \tag{3.37}$$

If now we rearrange the previous equation by splitting the contribution of particle-1 from the contributions of the remaining degrees of freedom, we obtain the classical Boltzmann transport equation (BTE) for the distribution f:

$$0 = \frac{\partial f}{\partial t} + \left[\frac{\partial f}{\partial R_1}\dot{R}_1 + \frac{\partial f}{\partial P_1}\dot{P}_1\right]_1 + \left[\int d^3P_2 \int d^3R_2 \frac{\partial V}{\partial \vec{R}_1}\frac{\partial f_2}{\partial P_1}\right]_{2,..,N} \tag{3.38}$$

or

$$\frac{\partial f}{\partial t} + \left[\frac{\partial f}{\partial R_1}\dot{R}_1 + \frac{\partial f}{\partial P_1}\dot{P}_1\right]_1 \equiv I_{\text{coll}}[f_2], \tag{3.39}$$

where the subscripts 1,2,...N in eq. 3.38 label the degrees of freedom, f_2 is the two-body distribution function and where the term on the r.h.s. of eq. 3.39 is the "collision integral" which involves a two-body distribution function and is due to interactions between a particle and its environment. We also clarify that on the l.h.s. no degrees of freedom other than particle - 1 appears. We can prove that the BTE is the lowest order equation of the Bogoliubov-Born-Green-Kirkwood-Yvon (BBGKY) hierarchy [95] as it involves only the single and two-body density function. Solving the BTE thus means deriving the collision integral in the first place, which requires the knowledge of f_2. Although an equation similar to the BTE can be derived for f_2 via BBGKY, the recursive appearance of three-, four-, n-body distribution functions imply the need to cut the expansion at some order. For any practical purpose some approximation has to be done to f_2 at the BTE level. A reasonable approximation introduced by Ehrenfest through the name `Stosszahlansatz` (molecular chaos hypothesis) would be to consider the velocities of the particles to be uncorrelated and position independent, thus leading to a factorisation of the two-particle distribution function into the product of two 1-particle distributions, namely

$$f_2^*(\vec{P}_1,\vec{R}_1,\vec{P}_2,\vec{R}_2,t) \approx f(\vec{P}_1,\vec{R}_1,t)f(\vec{P}_2,\vec{R}_1,t) \approx f_2^*(\vec{P}_1,\vec{R}_1,\vec{P}_2,t). \tag{3.40}$$

The collision integral describing the summation over all the four-particle scattering would turn into

$$I_{\text{coll}}[f_2] = \int d^3P_1 \int d^3P' \int d^3P'_1 \int d^3R[f_2^*(\vec{P}',\vec{R},\vec{P}'_1,t) - f_2^*(\vec{P},\vec{R},\vec{P}_1,t)]W_{\vec{P}+\vec{P}_1\to\vec{P}'+\vec{P}'_1}, \tag{3.41}$$

where W is the rate for a scattering process between two particles of momenta $\vec{P}$ and $\vec{P}_1$ resulting into two particles with momenta $\vec{P}'$ and $\vec{P}'_1$. Thereby the evolution of f is dependent on collisions that can increase the number of particles in a given state - thus driving the distribution out-of Equilibrium - or can decrease it. We shall also note that despite having a reversible microscopic dynamics, the Molecular Chaos assumption introduces some non-reversibility in the description of the system ensuing from having both short-ranged interactions and non-correlated velocities. In fact, eq. 3.41 means that the distribution is independent with respect to its past history, i.e. it follows a Markovian dynamics. The presence of scattering processes which decrease the number of particles in a given state in fact ensure that the system will equilibrate to a thermal distribution with maximum entropy, according to Boltzmann's H-theorem. Given the molecular chaos approximation, the simplest way to evaluate the collision integral would be to consider only the (net) decrease of the population in a certain state, thus replacing I_{coll} with

$$I_{\text{coll}}[f_2] = -\frac{f - f_0}{\tau}, \tag{3.42}$$

where f_0 is the single particle distribution in equilibrium conditions. This is the so called relaxation time approximation (RTA). It allows a faster solution of the BTE assuming that the relaxation time τ is known. As the relaxation of the distribution is exponential, this approximation generally does not account for the re-distribution of degrees of freedom during scattering but only for the events that tend to reinstate the equilibrium in the system.

We finally remind that the present formalism is not bounded to treat phonon-mediated heat transport only but also electronic transport and general collision mechanisms. An application of the BTE aimed at finding the electronic transport coefficients like

the electric conductivity, Seebeck coefficient and the electronic contribution to heat transport can be found in refs. [96, 97] where a derivation involving the Onsager reciprocal relations previously introduced does apply.

The previous analysis was meant to be for a classical system. Thus it is natural to extend it to the quantum mechanical case and specifically to obtain a description for an interacting phonon gas, which is our case of interest. In presence of an arbitrary perturbation $\hat{V}$ switched on at time $t = 0$ the equation of motion for the density matrix in the Dirac picture leads to:

$$\left(\frac{\partial n_\lambda}{\partial t}\right)_{\text{sc.}} = \text{Tr}\left[\frac{\partial \hat{\rho}}{\partial t}\hat{n}_\lambda\right]. \tag{3.43}$$

Let's expand the density matrix in the Dirac picture up to the second order:

$$i\hbar\hat{\rho}(t) = \hat{\rho}_0 + \int_0^t dt'[\hat{V}(t'), \hat{\rho}_0] + \int_0^t dt' \int_0^{t'} dt''[\hat{V}(t'), [\hat{V}(t''), \hat{\rho}(t'')]], \tag{3.44}$$

where $\rho_0 \equiv \exp(-\beta\hat{H})$ is the equilibrium thermal density matrix. If we cast eq. 3.44 inside eq. 3.43 and we make the semi-classical assumption that the off-diagonal terms in the density matrix - so called "coherences" - can be neglected, we finally obtain

$$\left(\frac{\partial n_\lambda}{\partial t}\right)_{\text{sc.}} = \sum_{\{\gamma\}}[W_{\{\gamma\}\to\lambda} n_{\{\gamma\}} - W_{\lambda\to\{\gamma\}} n_\lambda], \tag{3.45}$$

where $(\{\gamma\}, n_{\{\gamma\}})$ is a shorthand for the states and populations λ is involved through some scattering mechanism and the W - terms are the scattering probabilities per unit time between non-interacting states. These can be computed according to the Fermi's golden rule (FGR):

$$W_{a\to b} \equiv \frac{dP(|a\rangle \to |b\rangle)}{dt} = \frac{2\pi}{\hbar} |\langle b|\hat{V}|a\rangle|^2 \delta(E_a - E_b). \tag{3.46}$$

We also point out that the n_λ - terms in eq. 3.45 are non-equilibrium distributions. What is left to discuss now are the specific mechanisms that can affect the modes in a phonon gas. In a semiconductor the main intrinsic scattering effects that can influence the MFPs of phonons are due to the higher order terms in the atomic energy series expansion. Beside these, in a real semiconductor we should also consider that the translation symmetry of the pristine crystal is explicitly broken by the presence of isotopes in their natural concentrations and impurities, either wanted or accidentally inserted during the growth process. Also, scattering from boundaries and interfaces may turn out to be important if the system size is very small (sub-micrometric size), given that $\tau^{-1}_{\text{bound.}} \propto L^{-1}$. Moreover, while the electron-phonon interaction can generally be neglected in non-metals - since the phonon energies are much smaller than E_{gap}, they cannot excite the electronic states at the Fermi surface - it has been shown to be relevant in the case of ultra-doped (degenerate) semiconductors [98].

Thereby the effective Hamiltonian for a perturbed phonon gas can be re-written as

$$\hat{H} = \hat{H}_0 + \hat{H}_3 + \hat{H}_4 + \hat{H}_{\text{iso}} + \hat{H}_{\text{def}} + \hat{H}_{\text{eph}} + \hat{H}_{\text{b}} \equiv \hat{H}_0 + \hat{V}_{\text{tot}}, \tag{3.47}$$

where $\hat{H}_3 + \hat{H}_4$ is the contribution from the third and fourth order terms in the series expansion of the pristine system energy, $\hat{H}_{\text{iso}} + \hat{H}_{\text{def}}$ encloses the effect of isotopes and other defects, $\hat{H}_{\text{eph}}$ is the electron-phonon interaction and $\hat{H}_{\text{b}}$ gives the scattering from boundaries. Generally the anharmonic perturbations are much weaker than the quadratic leading order contribution $\hat{H}_0$, thus a treatment within first order perturbation theory is allowed. An exception may occur in the case of impurities as the ensuing effect on the lattice dynamics is generally strong enough to require higher order calculations. To compute the scattering rates for each term except the impurities we will use the FGR, since it permits to retain the quantum mechanical nature of phonons. In the case of defects, we will exploit classical scattering theory along with a Green's function formalism [99, 100].

If we consider a phonon mode $\lambda \equiv (b, \vec{q})$ we can ask ourselves how scattering mecha-

nisms can affect its population. In other words we seek to compute

$$\left(\frac{\partial n_\lambda}{\partial t}\right)_{\text{sc.}} = \left(\frac{\partial n_\lambda}{\partial t}\right)_{\text{incr.}} - \left(\frac{\partial n_\lambda}{\partial t}\right)_{\text{decr.}} \equiv \sum_{\text{processes}} \Gamma(\lambda|\text{processes}), \tag{3.48}$$

where Γ encodes all possible scattering mechanisms that the mode λ can experience. Another simplifying assumption that we will make consists in evaluating separately the contribution from each perturbation instead of using V_{tot} directly. This approximation, known as Matthiessen's rule, is generally acceptable assuming that the coupling between different perturbations is negligible. It can be also proven with variational methods that the Matthiessen's rule provides a lower bound for the lattice thermal conductivity [101].

3.2.1 Three-phonon scattering

Let's first study the case where $\hat{V} \equiv \hat{H}_3$. By using the relation between atomic displacements and phonon creation and annihilation operators - equation 2.52 - we can write the third order contribution to the ion energy in the reciprocal space basis as

$$\hat{H}_3 = \sum_{\lambda_1,\lambda_2,\lambda_3} A_{\lambda_1,\lambda_2,\lambda_3}(\hat{a}_{\lambda_1} + \hat{a}^\dagger_{-\lambda_1})(\hat{a}_{\lambda_2} + \hat{a}^\dagger_{-\lambda_2})(\hat{a}_{\lambda_3} + \hat{a}^\dagger_{-\lambda_3}), \tag{3.49}$$

with

$$A_{\lambda_1,\lambda_2,\lambda_3} \equiv \frac{1}{6}\left(\frac{\hbar}{2N}\right)^{3/2} \sum_{i,j,k,\tau,\tau',\tau''} \sum_{x_1,x_2,x_3} \frac{\Psi_{x_1,x_2,x_3}}{\sqrt{M_\tau M_{\tau'} M_{\tau''}}} \frac{s^{\lambda_1}_{\tau,x_1} s^{\lambda_2}_{\tau',x_2} s^{\lambda_3}_{\tau'',x_3}}{\sqrt{\omega_{\lambda_1}\omega_{\lambda_2}\omega_{\lambda_3}}} e^{i(\vec{q}_1\cdot\vec{R}_i + \vec{q}_2\cdot\vec{R}_j + \vec{q}_3\cdot\vec{R}_k)} \tag{3.50}$$

and

$$A_{\lambda_1,\lambda_2,\lambda_3} \equiv \frac{N}{6}\left(\frac{\hbar}{2N}\right)^{3/2} \Phi_{\lambda_1,\lambda_2,\lambda_3}, \tag{3.51}$$

where i, j and k are points in the direct lattice and τ, τ' and τ'' label the atomic positions inside the unit-cell. The N - factor in eq. 3.51 comes from the translation symmetry of the crystal. The convention $-\lambda \equiv (b, -\vec{q})$ has been adopted. Among all possible processes we consider only those that conserve the energy. The symmetry under translation of the third order IFCs ensures also the conservation of the crystal momentum up to a (reciprocal) lattice vector $\vec{Q}$:

$$\vec{q}_1 + \vec{q}_2 + \vec{q}_3 = \vec{Q}. \tag{3.52}$$

The case $\vec{Q} = 0$ ($\vec{Q} \neq 0$) identifies the so called Normal (Umklapp) processes, meaning that the (quasi)momentum is conserved modulo $\vec{Q}$. The form of eq. 3.49 clearly shows that two general types of processes can emerge, that is the creation of one phonon and annihilation of two or the absorption of one phonon and the creation of two. If we consider three modes λ, λ' and λ'', the possible interactions are summarised in Tab. 3.1. Our purpose now is to understand how the population of a certain mode λ is affected by $\hat{H}_3$. If we consider all the scattering processes a phonon state can go through and sum over the λ' and λ'' modes that satisfy energy and momentum conservation, eq. 3.45 can be recast into the following expression:

$$\frac{\partial n_\lambda}{\partial t} = \sum_{\lambda',\lambda''} \{\Gamma(\lambda' \to \lambda + \lambda'') + \Gamma(\lambda' + \lambda'' \to \lambda) - \Gamma(\lambda \to \lambda' + \lambda'') - \Gamma(\lambda + \lambda'' \to \lambda')\}, \tag{3.53}$$

with

$$\Gamma(\lambda' \to \lambda + \lambda'') = n_{\lambda'} W_{\lambda' \to \lambda + \lambda''}, \tag{3.54}$$

$$\Gamma(\lambda' + \lambda'' \to \lambda) = (n_{\lambda'} + n_{\lambda''}) W_{\lambda' + \lambda'' \to \lambda}, \tag{3.55}$$

	Emission(λ)	Absorption(λ)
Emission(λ'')	$\lambda' \longrightarrow \lambda + \lambda''$	$\lambda \longrightarrow \lambda' + \lambda''$
Absorption(λ'')	$\lambda' + \lambda'' \longrightarrow \lambda$	$\lambda + \lambda'' \longrightarrow \lambda'$

Table 3.1: Schematics of the possible $\hat{H}_3$ vertices.

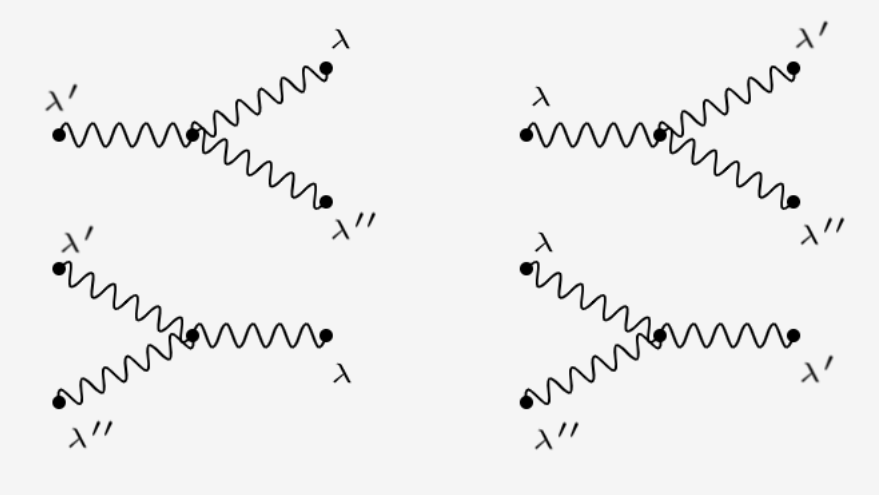

Figure 3.1: Vertex of the three-phonon processes depicted in 3.1, including absorption and emission of a λ state.

$$\Gamma(\lambda \to \lambda' + \lambda'') = n_\lambda W_{\lambda \to \lambda' + \lambda''} \tag{3.56}$$

and

$$\Gamma(\lambda + \lambda'' \to \lambda') = (n_\lambda + n_{\lambda''}) W_{\lambda + \lambda'' \to \lambda'}, \tag{3.57}$$

where additive (subtractive) contributions for creation (annihilation) of λ states are considered and where each amplitude Γ consists of a product between the corresponding scattering probability per unit time for an individual process and the total population for the incoming states. If we focus on the specific case where two phonons λ' and λ'' are absorbed and a phonon λ is emitted, we are looking for a transition where the initial (Fock) state is $|a\rangle \equiv |n_\lambda, n_{\lambda'}, n_{\lambda''}\rangle$ and the final state is $|b\rangle \equiv |n_\lambda + 1, n_{\lambda'} - 1, n_{\lambda''} - 1\rangle$. Since

the tensor elements $A_{\lambda_1,\lambda_2,\lambda_3}$ of the perturbation are symmetric under index exchange, we have six equivalent ways to describe the transition. Thus we can write

$$\langle b|\hat{H}_3|a\rangle = 6\frac{\sqrt{(n_\lambda+1)n_{\lambda'}n_{\lambda''}}}{\sqrt{\omega_\lambda\omega_{\lambda'}\omega_{\lambda''}}}A_{-\lambda,\lambda',\lambda''} \tag{3.58}$$

and finally, the FGR:

$$W_{a\to b} = \frac{\pi\hbar^2}{4N}\frac{(n_\lambda+1)n_{\lambda'}n_{\lambda''}}{\omega_\lambda\omega_{\lambda'}\omega_{\lambda''}}|\Phi_{-\lambda,\lambda',\lambda''}|^2\delta(\hbar\omega_\lambda-\hbar\omega_{\lambda'}-\hbar\omega_{\lambda''}). \tag{3.59}$$

Similar expressions can be computed for the remaining three types of scattering processes. By looking at tab. 3.1 and fig. 3.1 we can also understand that for each process $\lambda' \longrightarrow \lambda+\lambda''$ there is another process $\lambda+\lambda'' \longrightarrow \lambda'$, which can be seen as its time reversal. A similar relationship holds for $\lambda \longrightarrow \lambda'+\lambda''$ and $\lambda'+\lambda'' \longrightarrow \lambda$ scattering mechanisms. Thus we aim at evaluating the following non-equilibrium amplitudes $\Delta^1_{\lambda,\lambda',\lambda''} \equiv \Gamma(\lambda'+\lambda''\to\lambda)-\Gamma(\lambda\to\lambda'+\lambda'')$ and $\Delta^2_{\lambda,\lambda',\lambda''} \equiv \Gamma(\lambda'\to\lambda+\lambda'')-\Gamma(\lambda+\lambda''\to\lambda')$. Since in equilibrium conditions we expect them to be zero in virtue of the principle of detailed balance, if we switch on a small temperature gradient - and assume a non-equilibrium phonon distribution linear in $\vec{\nabla}T$ - we can approximate

$$\Delta^1_{\lambda,\lambda',\lambda''} \approx (n_{\lambda'}+n_{\lambda''}-n_\lambda)W^0_{\lambda\to\lambda'+\lambda''}, \tag{3.60}$$

$$\Delta^2_{\lambda,\lambda',\lambda''} \approx -(n_\lambda+n_{\lambda''}-n_{\lambda'})W^0_{\lambda+\lambda''\to\lambda'}, \tag{3.61}$$

where the 0-superscript in the scattering rates means the equilibrium distribution is used. Therefore we can write

$$\left(\frac{\partial n_\lambda}{\partial t}\right)_{\text{sc.}} = \sum_{\lambda',\lambda''}\left[\frac{1}{2}(n_{\lambda'}+n_{\lambda''}-n_\lambda)W^0_{\lambda\to\lambda'+\lambda''}-(n_\lambda+n_{\lambda''}-n_{\lambda'})W^0_{\lambda+\lambda''\to\lambda'}\right], \tag{3.62}$$

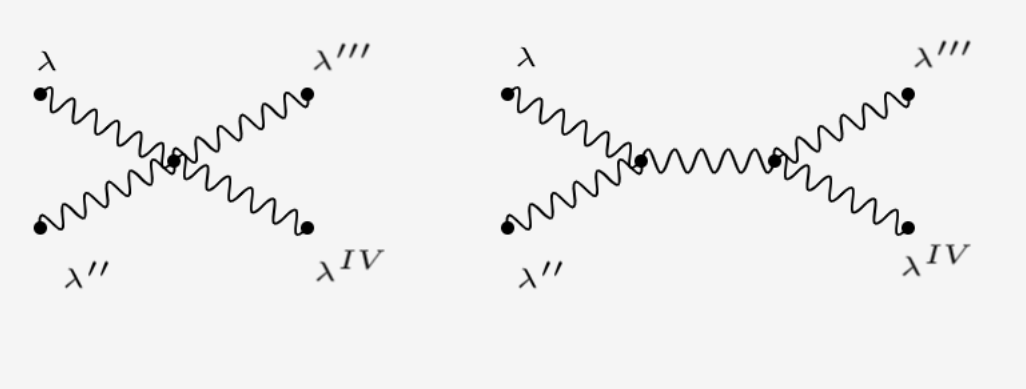

Figure 3.2: Four-phonons vertex and second order three phonons diagram.

where the $1/2$ factor in $(\partial n_\lambda/\partial t)_1$ has been added to avoid double counting, due to the interchangeability of λ' and λ'' states. The newly introduced expressions allow the calculation of the rate of the phonon population in terms of equilibrium quantities and scattering rates. We can proceed analogously for the remaining perturbations.

3.2.2 Four-phonon scattering

In a crystalline solid well below the melting temperature it is commonly assumed that higher order (beyond the third) terms in the ion energy expansion can be neglected. Despite this being truthful for most materials, it has been proven wrong - even at relatively low temperature - in those cases where the contribution of three-phonon scattering is relatively weak [102], thus magnifying the effect of other mechanisms. The scattering between four phonons at lowest order receives contributions from two terms. On one hand it can be treated by considering the fourth order IFCs within the FGR, with the interaction treated at the vertex level in the Feynman diagrams. On the other hand it can be calculated with the third order IFCs within second order perturbation theory, see fig. 3.2. The reciprocal space representation of $\hat{H}_4$ is:

$$\hat{H}_4 = \sum_{\lambda_1,\lambda_2,\lambda_3,\lambda_4} A_{\lambda_1,\lambda_2,\lambda_3,\lambda_4}(\hat{a}_{\lambda_1} + \hat{a}^\dagger_{-\lambda_1})(\hat{a}_{\lambda_2} + \hat{a}^\dagger_{-\lambda_2})(\hat{a}_{\lambda_3} + \hat{a}^\dagger_{-\lambda_3})(\hat{a}_{\lambda_4} + \hat{a}^\dagger_{-\lambda_4}). \tag{3.63}$$

We will not delve into an explicit derivation of contribution of the four-phonon scattering processes into the BTE, although a good reference can be found in [103] where

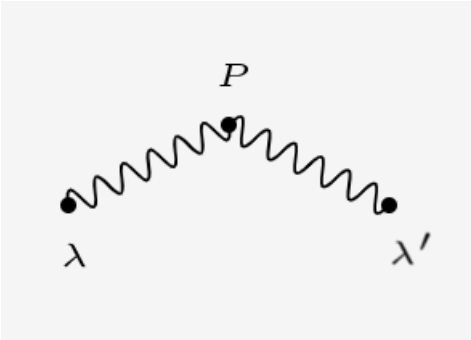

Figure 3.3: Scattering of a phonon λ into a λ' due to isotopes or other impurities. The total energy is conserved but the quasimomentum is not.

both the self-consistent and single mode RTA are presented and in [104]. It suffices to say that $\tau^{-1}_{\lambda;4} \sim T^2\omega^4$, meaning that the importance of the four-phonon vertex increases at high temperatures and frequencies.

3.2.3 Isotope and point-defect scattering

Scattering of phonons by impurities stems from two kinds of perturbations to the crystal Hamitonian: through a change in the mass, which prompts a variation in the kinetic energy, and through a local variation of the interatomic bonds near the defect site. Normally in a crystal even in absence of external defects the translation symmetry is broken at the kinetic level by the random concentration of mass impurities, due to the presence of isotopes. Indeed we can write

$$\hat{K}' = \sum_{i\tau\alpha} \frac{\hat{P}^2_{i\tau\alpha}}{2m_{i\tau}} = \sum_{i\tau\alpha} \frac{\hat{P}^2_{i\tau\alpha}}{2m_{0\tau}} + \sum_{i\tau\alpha} \frac{\hat{P}^2_{i\tau\alpha}}{2m_{i\tau}} \left(\frac{m_{0\tau} - m_{i\tau}}{m_{0\tau}} \right) \equiv \hat{K}_0 + \Delta\hat{K}, \tag{3.64}$$

where the subscript 0 indicates terms that fulfill the translation symmetry. For every type of atom - τ in the unit cell we can take $m_{0\tau} \equiv \sum_j m_{j\tau} f_{j\tau}$, with $f_{j\tau}$ being the natural concentration of the isotope - j. The latter is a parameter that cannot be inferred from calculations, rather its value should be determined from the natural occurrence of isotopes. The perturbation herein defined is quadratic with respect to the phonon creation and annihilation operators, therefore energy conservation allows for elastic processes where a given mode λ is scattered into a mode λ' with different wavevector

but same energy, see fig. 3.3. Following the work of Tamura [105, 106], if we apply the FGR with $\hat{V} \equiv \Delta\hat{K}$ we get

$$W^{\text{iso}}_{\lambda,\lambda'} = \frac{\pi}{2}\omega_\lambda^2 n_\lambda (n_{\lambda'}+1)\sum_\tau g(\tau)|\vec{s}_{\tau\lambda}\cdot\vec{s}_{\tau\lambda'}|^2\delta(\omega_\lambda-\omega_{\lambda'}), \tag{3.65}$$

where the randomness of the distribution of the isotopes has been taken into account. The introduced parameter g accounts for the isotope distribution, namely

$$g(\tau) = \sum_j f_{j\tau}\left(1-\frac{m_{j\tau}}{m_{0\tau}}\right)^2. \tag{3.66}$$

For example, the value of g in the case of As is 1.97×10^{-4}. Thus, the phonon population rate due to isotopes only is

$$\left(\frac{\partial n_\lambda}{\partial t}\right)_{\text{iso.}} = \sum_{\lambda'} W^{\text{iso},0}_{\lambda,\lambda'}[n_{\lambda'}-n_\lambda], \tag{3.67}$$

where again the superscript 0 means that the Bose-Einstein distribution is employed and where the first order relation $W^{\text{iso},0}_{\lambda,\lambda'} = W^{\text{iso},0}_{\lambda',\lambda}$ is used. It is worth to consider that eq. 3.67 can be treated within a single mode RTA formalism as it can be proven that the term $\sum_{\lambda'} W^{\text{iso},0}_{\lambda,\lambda'} n_{\lambda'}$ is constrained to vanish because of symmetry properties [107]. In particular it vanishes as ω_λ and $|\vec{s}_{\tau\lambda}\cdot\vec{s}_{\tau\lambda'}|$ are invariant under inversion while $\vec{q}$ is obviously not. Thus using a relaxation time is a well suited and rigorous approach in this case.

Since isotopes involve only a mass perturbation, the kinetic part alone is affected. However, more general impurities involve the making and breaking of inter-atomic bonds. Therefore, a bond perturbation encoded by a change in the IFCs should be included in these cases. As the latter may be non-perturbative, an all-order treatment is required, which can be achieved through the theory of Green's functions.

The classical linear equation of motion for a supercell with an impurity in a harmonic potential is:

$$\left(m_{j\tau'}\partial_t^2 + \sum_{i,\tau,\alpha}\Phi_{i,\tau,\alpha}^{\prime j,\tau' m\beta}\right)u_{j,\tau',\beta}(t) = 0, \tag{3.68}$$

which can be written in a matrix form

$$\left(M'\omega^2 - \Phi'\right)\vec{u} = 0, \tag{3.69}$$

where M' (M) and Φ' (Φ) are the mass and second order ICFs matrices for the doped (pristine) system. If we define the matrix perturbations V_M and V_K, i.e. mass and IFCs perturbations as

$$V_M^{ij,\alpha\beta}(\omega_\lambda) \equiv -\omega_\lambda^2 \frac{M'_i - M_j}{M_j}\delta_{ij}\delta_{\alpha\beta} \tag{3.70}$$

and

$$V_K^{ij,\alpha\beta} \equiv \frac{\Phi'^{ij,\alpha\beta} - \Phi^{ij,\alpha\beta}}{\sqrt{M_i M_j}} \tag{3.71}$$

with $V \equiv V_M + V_K$, we can rewrite Eq. 3.69 as

$$[\omega^2 I - M^{-1/2}\Phi M^{1/2} - V]\vec{u'} = 0. \tag{3.72}$$

The solution of $[\omega^2 I - M^{-1/2}\Phi M^{1/2}]\vec{u'} = 0$ is the usual harmonic one but with the dynamical matrix extended to the whole crystal. The resolvent for the unperturbed system is the bare harmonic retarded Green's function G_0^+ defined by

$$\langle i\alpha|\, G_0^+(\omega^2)\,|j\beta\rangle \equiv \sum_\lambda \langle i\alpha|\,\lambda\rangle\langle\lambda\,|j\beta\rangle\left(\omega^2 - \omega_\lambda^2 + i0^+\right)^{-1}. \tag{3.73}$$

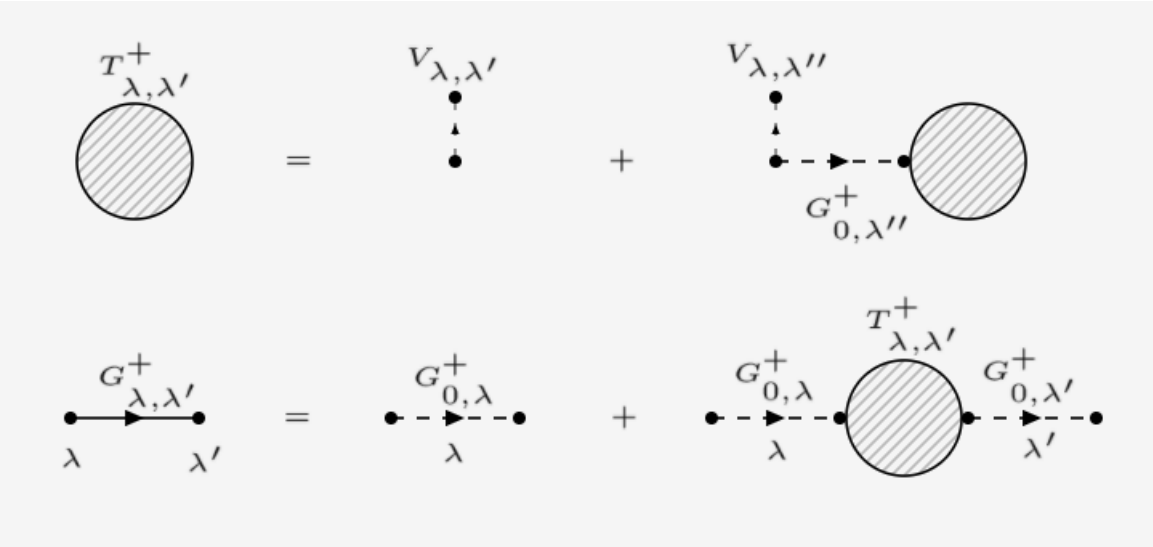

Figure 3.4: Feynman diagrams for the T-matrix and interacting Green's function. In presence of impurities or disorder the T-matrix plays the role of the self-energy in many body systems.

Once we have the resolvent in the $V = 0$ - case we can make use of the Lippmann-Schwinger equation to find the retarded defective system T-matrix and Green's function G^+:

$$T^+ = (1 - VG_0^+)^{-1}V, \tag{3.74}$$

$$G^+ = G_0^+ + G_0^+ T^+ G_0^+, \tag{3.75}$$

where the perturbation is included at all orders. The Feynman diagram representations for the T-matrix and total Green's function are given in fig. 3.4. Cutting the expansion at the second order defines the Born approximation, namely $T^+ \approx V + VG_0^+V$. It is possible to extract the relaxation time from the optical theorem [108] to obtain

$$\frac{1}{\tau_{\lambda,\mathrm{def}}} = -\frac{V_{\mathrm{uc}}}{\omega_\lambda} \mathrm{Im}\,\langle\lambda|\,T^+\,|\lambda\rangle\,, \tag{3.76}$$

where V_{uc} is the unit cell volume. We stress that the λ-states have been extended to the whole supercell. The formulation introduced insofar allows us to cast an arbitrary impurity distribution inside the perturbation V. However, this can be proven to be numerically unfeasible with first principles calculations, where the employed supercells contain a few hundred atoms at most. If we consider

$$V = \sum_j V_j, \tag{3.77}$$

where j indicates an individual impurity site, the expression for the T-matrix turns into

$$T^+ = (1 - VG_0^+)^{-1}V = \sum_j V_j + \Big(\sum_i V_i\Big) G_0^+ \Big(\sum_k V_k\Big) + O(V^3). \tag{3.78}$$

Here, off-diagonal terms connecting defects at two different sites appear. If we neglect this correlation by assuming that $V_i G_0^+ V_i \gg V_i G_0^+ V_j$ for every $j \neq i$, we can write

$$T^+ \equiv \sum_i \chi_i T_i^+, \tag{3.79}$$

where χ_i is the concentration of type - i impurity and

$$\frac{1}{\tau_{\lambda,\mathrm{def}}} = -\chi \frac{V_{\mathrm{uc}}}{\omega_\lambda} \operatorname{Im} \langle \lambda | T^+ | \lambda \rangle \tag{3.80}$$

if a single kind of dopant is considered. In this thesis we will use this approach. We can try to understand the limitations that this approximation presents by evaluating in a qualitative way the $V_i G_0^+ V_j$ - term. We follow the argument proposed by Mott and Massey [109, 110] in the case of a two - mass defect in a crystal. It can be proven that the off-diagonal terms become relevant if the amplitude of the scattered state at a neighboring defect is large, i.e. if $\sqrt{\sigma}/R \geq 1$ where σ is the cross-section and R is the distance between the two defect centers. This relation can be rewritten as $1/|\vec{q}| \geq R$ or

$\lambda \geq R$, where λ is the wavelength, if we consider the optical theorem. In this case the inter-site correlations can be safely neglected for most of the modes with the possible exception of long - wavelengths phonons, if we consider only dilute impurity concentrations. Furthermore at non-cryogenic temperatures the $\vec{q} \to 0$ modes generally account for a small fraction of the transported heat in a crystal as shorter wavelengths have a non - negligible contribution to the material heat capacity. Although we are mainly interested in studying the thermal conductivity of semiconductors in the low-doping limit by mean of the independent defect approximation, it is worth to mention that several theoretical treatments have been developed in order to overcome its limitations, as neglecting the correlation between defects can lead to strong inaccuracies in strongly-doped, disordered and alloy systems at low temperature. A list of these methods includes the virtual crystal approximation (VCA), the coherent potential approximation (CPA) [111, 110] and the application of special quasirandom structures (SQSs) [112] to study the effect of force constant disorder in semiconductor alloys [113].

3.2.4 Electron-phonon scattering

Electron-phonon coupling can be one of the most relevant interactions in solids, especially in the case of metals. Although in weakly doped semiconductors it can be neglected, this is not the case when the doping concentration exceeds a value of $\sim 10^{20}$ cm^{-3} [98]. Since the masses of ions M are much larger than the electron mass m_e, it is possible to write the ion-electron Hamiltonian in power series for m_e/M. The lowest order corresponds to the Born-Oppenheimer Approximation, which assumes a partial decoupling between ionic and electronic degrees of freedom. The first order of the expansion, instead, gives the vertex of the electron-phonon interaction: as the atoms are displaced out of their equilibrium positions, this triggers a change δV in the potential felt by the electrons. This allows transitions between different Bloch states, i.e. $\langle \psi_{n\vec{k}} | \, \delta V \, | \psi_{m\vec{k}'} \rangle$. If we assume a linear relation between δV and the ion displacements we can write

$$\delta V = \vec{u} \cdot \varepsilon^{-1} (\vec{\nabla} V)_{eq.}, \tag{3.81}$$

where the gradient is evaluated in the minimum energy equilibrium configuration, $\vec{u}$ is the ion displacement and ε here is the dielectric matrix. The latter serves the purpose of screening the interaction inside a crystal. References about the Thomas-Fermi and Lindhard (RPA) screening can be found in [114]. Since δV is the source of electron-phonon interaction, hereafter we will evaluate it in its second quantization form:

$$\hat{H}_{eph} = \sum_{\vec{k},n,m} \sum_{\sigma} \sum_{\lambda} g^{\vec{k},m}_{\vec{k}+\vec{q},n}(\lambda) \hat{c}^{\dagger}_{\vec{k}+\vec{q},n\sigma} \hat{c}_{\vec{k},m\sigma} (\hat{a}_{\lambda} + \hat{a}^{\dagger}_{-\lambda}), \tag{3.82}$$

where σ represents the electron spin and λ is a short for the phonon wavevector $\vec{q}$ and polarisation b as always. The operators $\hat{c}$ and $\hat{c}^{\dagger}$ are the fermionic annihilation and creation operators such that $\{\hat{c}_{\vec{k}\sigma}, \hat{c}^{\dagger}_{\vec{k}'\sigma'}\} = \delta_{\vec{k}\vec{k}'}\delta_{\sigma\sigma'}$, $\{\hat{c}_{\vec{k}\sigma}, \hat{c}_{\vec{k}'\sigma'}\} = 0$ and $\{\hat{c}^{\dagger}_{\vec{k}\sigma}, \hat{c}^{\dagger}_{\vec{k}'\sigma'}\} = 0$. The matrix elements g are the electron-phonon couplings:

$$g^{\vec{k},n}_{\vec{k}+\vec{q},m}(\lambda) = \sum_{\alpha,b} A^{\lambda}_{\alpha,b} \left\langle \psi_{m,\vec{k}+\vec{q},\sigma} \middle| \delta^{\vec{q}}_{b\alpha} V \middle| \psi_{n,\vec{k},\sigma} \right\rangle, \tag{3.83}$$

where α is the Cartesian direction and the A - elements relate the atomic displacements to the phonon creation and annihilation operators in eq. 2.52. These g - couplings describe the transition between different electronic states triggered by a lattice vibration λ. We can use the herein defined $\hat{H}_{eph}$ along with a single-particle electron Hamiltonian $\hat{H}_e = \sum_{n\vec{k}\sigma} \varepsilon_{\vec{k},n} \hat{c}^{\dagger}_{\vec{k},n,\sigma} \hat{c}_{\vec{k},n,\sigma}$ to write

$$\hat{H} = \hat{H}_0 + \hat{H}_e + \hat{H}_{eph}. \tag{3.84}$$

This is the Frölich Hamiltonian [115] with the electronic bands treated as stationary solutions in a perfect periodic lattice. It is possible to include at the DFT level the effects of the electron-electron Coulomb interaction inside the energy terms $\varepsilon_{\vec{k},n}$. Whereas the electrons are mostly influenced by lattice vibrations near the Fermi level, phonon frequencies on the other hand experience strong renormalization due to screening effects.

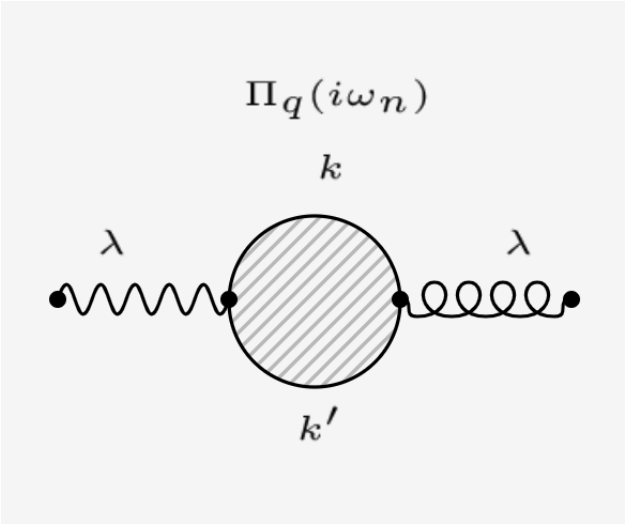

Figure 3.5: Electron-phonon bubble diagram with virtual electron-hole pairs created inside the loop.

Thereby it is reasonable to start the description of their mutual interaction from a bare-electron point of view. time-dependent perturbation theory can be used to include the effect of electrons on the phonon states in a Green's function perspective. As we are mainly interested in modeling the phonon relaxation time due to electron scattering, the phonon self-energy Π at the lowest order in the Matsubara representation is:

$$\Pi_\lambda(i\omega_n) = \frac{1}{N_{\vec{k}}} \sum_{\vec{k},\vec{k'}} |g^{\vec{q}}_{\vec{k},\vec{k'}}|^2 \frac{f(\varepsilon_{\vec{k}}) - f(\varepsilon_{\vec{k'}})}{i\omega_n + \varepsilon_{\vec{k}} - \varepsilon_{\vec{k'}}}, \tag{3.85}$$

where f is the Fermi-Dirac distribution and where the Matsubara summation has been performed. The Feynman diagram representation of the self-energy is depicted in fig. 3.5. We can derive the phonon relaxation time as $\tau_\lambda^{-1} = -2\mathrm{Im}\{\Pi_\lambda(\omega_\lambda)\}$, which requires the analytic continuation $i\omega_n \to \omega + \delta\eta$:

$$\tau_\lambda^{-1} = \frac{2\pi}{N_{\vec{k}}} \sum_{\vec{k},\vec{k'}} |g^{\vec{q}}_{\vec{k},\vec{k'}}|^2 [f(\varepsilon_{\vec{k}}) - f(\varepsilon_{\vec{k'}})] \delta(\omega_n + \varepsilon_{\vec{k}} - \varepsilon_{\vec{k'}}). \tag{3.86}$$

This equation only allows for a single mode RTA treatment of the phonon Boltzmann equation and it can be further simplified if we take the low-T limit or double delta ap-

proximation [116], so that $f(\varepsilon_{\vec{k}}) - f(\varepsilon_{\vec{k}'}) \longrightarrow -f'(\varepsilon_{\vec{k}})\omega_{\vec{q}}$. More sophisticated treatments that include the possibility of mode re-population can be found in [117]. The *ab initio* evaluation of eq. 3.86 is generally cumbersome, especially in the case of complex unit cells, thus it is customary to make simplifying assumptions in order to reduce the computational burden, like fitting first principles calculations to deformation potential models [118, 119]. These quantify how the electronic bands are affected by lattice displacements through the perturbative evaluation of a Hamiltonian of the type [120]:

$$\hat{H}^d_{ij} = \sum_{\alpha,\beta=1\ldots3} D^{\alpha\beta}_{ij}\varepsilon_{\alpha\beta}, \tag{3.87}$$

where $D^{\alpha\beta}_{ij}$ is the deformation potential operator (second rank tensor) and $\varepsilon_{\alpha\beta}$ is the strain tensor. Under simplifying assumptions on the electronic and phononic dispersions, using a deformation potential of the form $D_a q$ (D_o) for acoustic (optical) branches in the long-wavelength limit leads to an analytical expression for the relaxation times [98]. In the end we mention a recent theoretical development that consists into finding a Wannier functions representation of the Bloch states, so that it is possible to interpolate them to a tight reciprocal space mesh [13]. This in turn improves the numerical accuracy of the relaxation times and transport coefficients from first principles and without resorting to deformation potential models.

3.2.5 Boundary scattering, size-related effects and interfaces

In finite size systems an additional scattering term appears, as phonons interact with the boundaries and are reflected by them. The corresponding scattering rates can be modelled as [121]:

$$\tau^{-1}_{\lambda;\text{bound.}} = \frac{v_\lambda}{L}(1 - p_\lambda), \tag{3.88}$$

where L is the length of the crystal and p_λ is the so called "specularity parameter":

$$p_\lambda = \exp\left[-16\pi^3\eta^2 q^2\right] \tag{3.89}$$

which takes the value of one for a perfectly smooth surface (corresponding to a specular reflection) and the value of zero in the case of a completely rough surface, corresponding to totally diffusive scattering. The latter case is also known as "Casimir limit" [122]. In eq. 3.89 an empirical parameter η - to be fitted to first principles calculations or experimental data - has also been introduced. The presence of this additional term is particularly important at low-temperature: indeed, it dominates the phonon physics in the T$\longrightarrow$0 limit as the remaining scattering processes vanish, leading to a scaling of the transport coefficients with L [123]. Furthermore, it is generally important in low-dimensional systems (2D crystals like graphene) and nanostructures, since its presence is often the sole mechanism that can lead to a finite mean free path for long-wavelength acoustic modes.

Boundary scattering can be used to design the phonon-related transport properties in nanostructures, as they are dependent on the system geometry. Indeed, it was observed that the introduction of a serpentine structures in Si nanowires decreases the thermal conductance by 40% below 5 K [124]. In ref. [125] a T-matrix based first principles formulation which included the effect of the boundaries at the harmonic level has been proposed to study the surface roughness of silicon nanowires, showing that the conductivity can take lower values than those obtainable from the application of the Casimir limit ($p_\lambda \equiv 0$).

It has also been shown that the scattering from boundaries, along with the intrinsic three-phonon interactions and disorder, marks the difference between alloys and single crystals cross-plane heat conduction. In particular, the presence of Rayleigh scattering in alloys leads to a quasiballistic behaviour for the cross-plane conductivity $\kappa_{\text{cross}} \sim L^{2-\alpha}$ [126], where $1 < \alpha < 2$ is the Lévy exponent [127]. The specific value of α is determined by the dominant scattering mechanism ($\tau^{-1} \sim \omega^n, n > 3 \Longrightarrow \alpha \equiv 1 + 3/n$). On the other hand, single crystals have a logarithmic scaling [126] with respect to the size. Another interplay between boundary, intrinsic and disorder-related scattering has been

theoretically evaluated in $Mg_2Si_xSn_{1-x}$ nanowires [128]. Since alloying reduces the number of phonons with high mean free path with respect to the parent compounds, this can explain the differences in the ballistic-to-diffusive crossover between pure Mg_2Si / Mg_2Sn and their alloys.

Size effects in phonon transport have been highlighted in carbon nanotubes, where it was proven that they leads to a power law scaling of the conductivity with respect of the nanotube length, namely $\kappa \sim L^{1/3}$ [129]. This power law was also predicted to saturate, for a length of 10 μm at 300 K, to an approximate value of ~ 4000 W·K^{-1}·m^{-1} if the three-phonon scattering is included beyond the first order only in perturbation theory.

Regarding isotope-enriched boron nitride nanotubes, it has been suggested [130] that a finite size may lead to the Anderson localisation for phonons. However, the possibility of using thermal transport measurement to observe it was disproved by theoretical calculations [131]. Indeed, in the 0 K - 50 K temperature range the transport is ballistic, with a size-independent transmission function, while for higher temperatures an eventual localisation regime should coexist with the diffusive scattering induced by anharmonicities. Rather, a reduction of the conductivity is better explained in terms of phonon-isotope scattering [132]. Nevertheless, in more recent times Anderson localisation detection at the thermal transport level has found some positive confirmation in theoretical calculations on aperiodic Si/Ge superlattices [133] - where it was predicted to quench the conductivity to a value of 1.3 W·K^{-1}·m^{-1} at room temperature (reduction of 98%), with a non-monotonic trend of κ as a function of the system size - and in experiments on GaAs/AlAs superlattices with embedded ErAs nanodots, where a maximum in the size-dependent conductivity has been detected at 30 K [134].

In the case of interfaces between materials, the description of the "surface roughness" - namely, how coherent are the scattering and propagation of phonons - is a major modelling hurdle. The need to find how the transmission function of phonons behaves at the interfaces from first principles has prompted the development of the acoustic mismatch model (AMM) [135] and of the diffusive mismatch model (DMM) [136, 137]. The AMM

assumes a coherent transport regime with the modes behaving at the boundary according to the Snell's law, and is generally more accurate at low temperatures. The DMM on the other hand takes the phonon propagation to be completely diffusive, and performs better at high T (> 30 K according to measurements by Swartz and Pohl [136]). None of these these approaches can reliably model the thermal transport at the interface in the whole low-T / high-T crossover, and the acoustic (diffusive) mismatch model rather constitutes an upper (lower) bound for the conductance. Improving these two models is possible by mean of molecular dynamics calculations, which, however, completely neglect the quantum effects for phonons. Other methods involving the use of atomistic Green's function techniques (AGF) have been suggested [138, 139]. Although harmonic models are usually employed to study interfaces and nanostructures within AGF, extensions that include anharmonic effects [140] via Keldysh formalism [141] have been developed. The inclusion of anharmonicities in the modelling of interfaces has also been proposed by [142] in the so called "anharmonic inelastic model" (AIM), which shows an improvement with respect to the DMM for Pb/diamond and Au/diamond interfaces since the temperature dependence of the phonons populations is taken into account. Finally, we mention the development of Monte Carlo methods [143] to study from first principles the boundary scattering in thin film and interfaces under the DMM, including also the elastic mode conversions. This approach has been combined with AGF techniques to study the thermal transport at GaN/AlN graded interfaces [144].

3.2.6 Phonon Boltzmann equation and thermal conductivity

Once the scattering rates have been evaluated, we can use them to solve the Boltzmann equation for phonons. If we assume that a thermal gradient $\vec{\nabla}\mathrm{T}$ is switched on and a stationary state is obtained,there is a balance between the collision and diffusion terms of the BTE where the latter can be written as

$$\left(\frac{\partial n_\lambda}{\partial t}\right)_{\text{diff.}} = \vec{v}_\lambda \cdot \vec{\nabla}\mathrm{T}\frac{\partial n^0_\lambda}{\partial \mathrm{T}}. \tag{3.90}$$

We have assumed that the thermal gradient is coupled with the spatial dependence of the distribution function in low - field condition. Specifically we have taken $n_\lambda \approx n^0_\lambda + \vec{F}_\lambda \cdot \vec{\nabla}\mathrm{T}$ with the gradient appearing only linearly in the equation, so that any higher order term in $\vec{\nabla}\mathrm{T}$ can be neglected. With this assumption the BTE is linearised, if we include three-phonons and impurity-mediated two-phonons interactions in the collision part we obtain:

$$B_\lambda \vec{F}_\lambda = \vec{v}_\lambda \frac{\partial n^0_\lambda}{\partial \mathrm{T}} + \sum_{\lambda',\lambda''} \left[\frac{1}{2}(\vec{F}_{\lambda'} + \vec{F}_{\lambda''}) W^0_{\lambda,\lambda'+\lambda''} + (\vec{F}_{\lambda'} - \vec{F}_{\lambda''}) W^0_{\lambda+\lambda'',\lambda'} \right], \tag{3.91}$$

with

$$B_\lambda \equiv \sum_{\lambda',\lambda''} \left[\frac{1}{2} W^0_{\lambda,\lambda'+\lambda''} + W^0_{\lambda+\lambda'',\lambda'} \right] + \sum_{\lambda'} W^{\mathrm{iso},0}_{\lambda,\lambda'} + \frac{1}{\tau_{\lambda,\mathrm{def}}}. \tag{3.92}$$

Other scattering mechanisms can be included in a similar way. We can notice that only the three-phonon mediated interaction is considered beyond the RTA, while scattering from impurities and isotopes only contribute to decrease the population of the modes. The solution of eq. 3.91 can be found self-consistently starting from the RTA solution, namely

$$\vec{F}_{\lambda,0} \equiv \vec{v}_\lambda \frac{\partial n^0_\lambda}{\partial \mathrm{T}} \frac{1}{B_\lambda}. \tag{3.93}$$

A different formulation based on the variational method instead has been proposed by [145]. Once the solution of the BTE is known, the thermal transport coefficients can be evaluated. The heat flux carried by a phonon population in non-equilibrium stationary condition is

$$\vec{J} = \frac{1}{V_{uc}} \sum_\lambda \hbar \omega_\lambda \vec{v}_\lambda n_\lambda = \frac{1}{V_{uc}} \sum_\lambda \hbar \omega_\lambda \vec{v}_\lambda (\vec{F}_\lambda \cdot \vec{\nabla}\mathrm{T}), \tag{3.94}$$

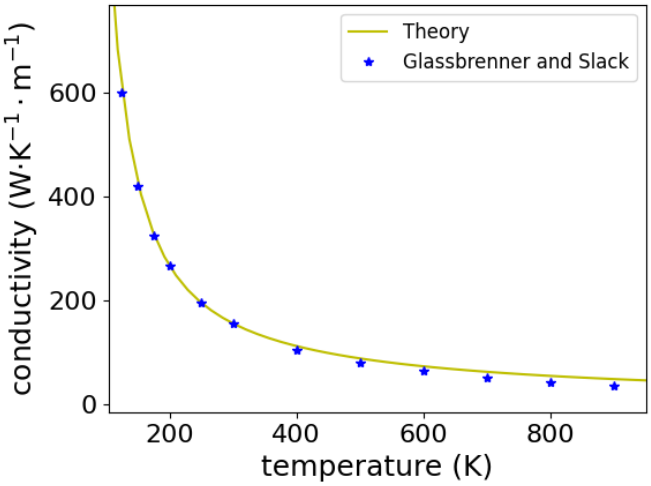

Figure 3.6: Thermal conductivity of silicon as a function of temperature, theoretical vs experimental results. Continuous line: self consistent calculation according to eq. 3.95 and 3.96 carried out with the *almaBTE* software. Stars: measurements with 5% uncertainty taken from ref. [7].

where the term containing the equilibrium distributions vanishes as $\vec{v}_\lambda = -\vec{v}_{-\lambda}$. We can therefore identify the phonon contribution to the thermal conductivity as

$$\kappa^{\alpha\beta} = \frac{k_B}{V_{uc}} \sum_\lambda \left(\frac{\hbar\omega_\lambda}{k_B T}\right)^2 n_\lambda^0 (n_\lambda^0 + 1) v_\lambda^\alpha L_\lambda^\beta, \tag{3.95}$$

where we have defined an effective directional mean free path L_λ^β from

$$F_\lambda^\beta \equiv F_{\lambda,0}^\beta + \Delta[F_\lambda^\beta] \equiv -\frac{\partial n_\lambda^0}{\partial \mathrm{T}} L_\lambda^\beta. \tag{3.96}$$

The nomenclature "effective" derives from the full solution of the BTE which assumes a non - exponential relaxation of the phonon populations. The lattice thermal conductivity as a function of temperature in the example case of pure silicon is plotted in figure 3.6. The *ab initio* theoretical calculation - involving three- and isotope mediated phonon scattering only - is in good agreement with the measured values reported by Glassbrenner and Slack [7], particularly at low temperature (where the contribu-

tions from other mechanisms - above all, four- and electron- phonon - can be safely neglected).

The present formalism does not allow us to distinguish explicitly between Normal and Umklapp processes and thus to define an RTA in the sense that inelastic processes are explicitly considered. Nevertheless it can be intuitively understood that when the U - processes dominate, the true solution of eq. 3.91 will not differ much from the single mode RTA case where phonons tend to relax exponentially. The iterative procedure couples different phonon modes together, whereby the magnitude of $|\vec{F}_\lambda - \vec{F}_{\lambda,0}|$ tells us how much different phonon modes interact while evolving towards equilibrium. If the transport is dominated by long - wavelength phonons, most of the processes these phonons undergo are Normal as the outgoing states from a scattering event are unlikely to exit the Brillouin zone. These processes contribute to keep the phonon gas adrift and in the stationary non-equilibrium state, with a distribution that behaves like

$$n_{\vec{q}}(\omega;\mu) = [\exp(\beta(\hbar\omega - \vec{\mu}\cdot\vec{q})) - 1]^{-1}, \tag{3.97}$$

where $\vec{\mu}$ is the total crystal quasimomentum of the distribution associated with the drift velocity of the flow and linear in the thermal gradient. But as long as the iterative procedure continues, more and more states with higher $\vec{q}$ will be formed to have, in the end, Umklapp processes that will equilibrate the system. It can be seen that in the limit where the U processes vanish, the thermal conductivity diverges. Indeed, this is equivalent to inducing a finite heat flux response for a distribution of the form of eq. 3.97, despite having a zero thermal gradient.

Despite being out of the scope of this thesis, we can mention that before the advent of first principles based calculations it was common strategy to employ the relaxation time approximation to evaluate the thermal conductivity with analytical formulae for the scattering rates. Common relaxation times include the Callaway model [146] which assumes a linear phonon dispersion $\omega_{\vec{q}} = v|\vec{q}|$ and a deviation from equilibrium that is proportional to $-\tau_T \vec{v}\cdot\vec{\nabla}T$, with $\tau_T \equiv \tau_c(1 + a/\tau_N)$. The definition of τ_c includes the

separate contribution from Normal and Umklapp processes, i.e. $\tau_c^{-1} = \tau_N^{-1} + \tau_U^{-1}$. This model further separates the conductivity into two contribution κ_1 and κ_2 where:

$$\kappa_1 \equiv \frac{k_B^4}{2\pi^2\hbar^3 v}\int_0^{T_D/T} dx \frac{x^4 e^x}{(e^x-1)^2}\tau_c, \tag{3.98}$$

$$\kappa_2 \equiv \frac{a k_B^4}{2\pi^2\hbar^3 v}\int_0^{T_D/T} dx \frac{x^4 e^x}{(e^x-1)^2}\frac{\tau_c}{\tau_N} \tag{3.99}$$

and

$$a \equiv \left[\int_0^{T_D/T} dx \frac{x^4 e^x}{(e^x-1)^2}\frac{\tau_c}{\tau_N}\right] \Bigg/ \left[\int_0^{T_D/T} dx \frac{x^4 e^x}{(e^x-1)^2}\frac{1}{\tau_N}\left(1-\frac{\tau_c}{\tau_N}\right)\right]. \tag{3.100}$$

If no Umklapp scattering is present we can easily see that both a and κ diverge as expected. The analytical formulas for the relaxation times take $\tau_U^{-1} = A\omega^2 T^3 \exp(-T_D/bT) + c/L$ and $\tau_N^{-1} = B\omega^2 T^3$ where A, B and b are parameters to be determined experimentally and where c/L represents the boundary scattering (c is the speed of sound and L the size of the system). A complete discussion about improved versions of the Callaway model can be found in Refs. [147, 148]. Finally, we mention that in more recent times the linearity of the BTE has led to the development of the so called "relaxon theory" [101] where the collision operator is diagonalised and the thermal conductivity can be written in terms of "relaxons", i.e. linear combinations of phonon modes that, by construction, relax exponentially towards equilibrium. The latter methodology has proven particularly useful to study transport in low - dimensional materials, and concerning hydrodynamic thermal transport properties like phonon second sound, Poiseuille flow and thermal viscosity [149]. Since for the latter the transport is dominated by Normal processes, it is clearly impossible to study them with accuracy from a single mode RTA perspective.

3.3 Measuring the thermal conductivity

In this section we review the main methods devised to measure the thermal transport coefficients in bulk materials. Thermal conductivity measurement techniques in materials can generally be categorised as static or steady-state and dynamics. For more detailed information the reader can look at the review of Zhao et al. [150].

3.3.1 Steady-state methods

In steady-state measurements a temperature difference $\Delta T = T_h - T_c$ is established at the boundaries of a system of width d and section S and then left unchanged. Then the ensuing heat flux $\vec{J} \equiv \dot{Q}\vec{n}/S$ crossing the material surface is measured with temperature sensors, with the thermal conductivity given by $\kappa = \dot{Q}d/S\Delta T$. This method is well suited for systems with rectangular or cylindrical geometries. It is important to notice that several sources of errors may hamper the correct evaluation of the conductivity. One of them is the precise evaluation of ΔT: this is usually performed by means of thermocouples with an experimental associated error that can be smaller than 1 %.

The most important hurdle concerning the measurement of κ with the steady-state approach is related to the evaluation of $\dot{Q}$. Indeed, the measured value of $\dot{Q}$ not only includes the heat flux generated by the established temperature difference but also a contribution from dissipative mechanisms like parasitic currents or convection flows and loss of heat even by conduction itself as the system keeps interacting with the surrounding environment. Also, a source of error could be the thermocouples themselves, as heat could potentially flow through them, thus perturbing the measurement. Moreover a substantial contribution to the heat flux can be generated by radiation related mechanisms, especially when the operating temperature of a sample is above ~ 1000 K. Thus, the extra-contributions to $\dot{Q}$ not directly related to ΔT have to be evaluated and subtracted to properly assess the value of the thermal conductivity. While the contribution from parasitic currents should be controlled to be less than 2% of the total flux, convection/radiation phenomena can be reduced if the sample is put in a shielded vacuum chamber. To minimise the effect of the thermocouples, low thermal

conductivity and small diameter wires are preferred. We finally mention the comparative methods where two samples of different composition are cast in series and the thermal conductivity of one of them can be extracted if the other material conductivity is known.

3.3.2 Frequency/time domain methods

Steady-state methods present drawbacks like the aforementioned ones concerning the correct evaluation of $\dot{Q}$. Furthermore, a sample could take a relatively long time to reach a stationary state to begin with. Therefore several methods that involve the evaluation of a time-dependent ΔT have been developed. We will review some of these approaches.

The pulsed power technique developed by Maldonado [151] involves an *ac* electric current passed through the heat source ($T = T_h$), while the temperature of the heat sink T_c changes slowly. A time-dependent difference $\Delta T(t) = T_h(t) - T_c$ is therefore established and can be measured with a calibrated gold-ferrochrome thermocouple. Thus, the heat flow must satisfy the non-linear equation

$$\dot{Q} = C(T_h)\frac{dT_h}{dt} = R(T_h)I^2(t) - \kappa\left(\frac{T_h + T_c}{2}\right)\Delta T(t), \tag{3.101}$$

where C, R and κ are the heat capacity, electrical resistance (at the source) and thermal conductance of the sample. If we can assume $\Delta T(t)$ to be small, T_h can be replaced by T_c (considered a constant) in the C, R and κ expressions: this turns the previous equation linear and easier to solve. By knowing or measuring the value of the heat capacity and resistance at the sink temperature and the *ac* current, the thermal conductivity can be extracted from the solution of the linearised eq. 3.101 and from the thermocouple measurements of ΔT. Maldonado [151] reports a measurement error smaller than 3%.

Another time domain approach is the hot wire method [150]. In this case, a metallic wire (usually Ta or Pt) is embedded inside a sample with cylindrical geometry and a constant electric bias is applied, so that the heat generated via Joule effect sets off a

time-dependent thermal field. The heat flow is considered to be radial with respect to the linear source, whose diameter has to be much smaller than the sample size and where the conductivity is assumed to be isotropic. Also, if it is assumed that the wire length is infinite so that boundary effects can be neglected, then κ can be extracted by measurements of the temperature at different times performed at the external surface of the sample. This method can attain a high precision, i.e. with an error lower than 1-2 % and is usually employed for low thermal conductivity materials.

Other time domain methods worth mentioning are the transient plane source (TPS) where the thermal response is induced by inserting a metal strip (or a disk) between two sample slabs to then let a current flow through [152] and the laser flash method [153, 154] where an optical stimulus is used instead. The latter method is deemed to be particularly apt to reduce the error induced by interface resistance between samples. Both techniques extract the thermal conductivity by fitting thermal profiles to analytical models which extract the thermal diffusivity α. In particular, independent measurements of the specific heat are required to extract κ from the knowledge of α in the case of the laser flash method. Of particular importance are also the 3-ω method introduced by Cahill et al. [155, 156] and thermoreflectance techniques [157, 158] in both time [159] and frequency domains [160] (time domain/frequency domain thermoreflectance or TDTR/FDTR) which have been developed in the context of thin films measurements but also applied for bulk materials.

In the 3-ω approach a film is positioned between a substrate (usually Silicon or Sapphire) and a metallic strip. Then an *ac* current flows through the strip which acts both like a heater and a thermal sensor. The resulting detectable voltage includes a term proportional to $\cos(3\omega t + \phi)$ - where ω is the frequency of the driving *ac* current and ϕ is a phase - and contains the information pertaining to the film thermal transport coefficients. Temperature profile models are fitted to the thermal sensor data to extract the in-plane and cross-plane thermal conductivities. This method usually assumes isotropic thermal coefficients or the alignment between the Cartesian axes of film, strip and substrate - although a version that overcome this limitation has been proposed [161] - and has the advantage to reduce heat loss by radiation with an experimental error

less than 2%, although the need of strip micro-fabrication can be challenging.

In the TDTR/FDTR techniques the samples are coated with a metallic thin film. A pump laser beam is then used to heat the film and a probe beam to detect its reflectance coefficient which contains the information about the sample thermal properties. More specifically the TDTR method measures the temperature decay as a function of the delay δt between the pump and the probe signal while in the FDTR the delay is fixed and the response with respect to a change in the pump modulation frequency is measured. A photodiode is used to collect the data from the probe signal. The thermoreflectance response at modulation ω_0 can be expressed by:

$$Z(\omega_0, \delta t) = V_{in} + iV_{out} = \tilde{\beta}\Delta_s \sum_n h(n\Delta + \delta t) e^{-i\omega_0(nT_0+\delta t)}, \tag{3.102}$$

where ω_0 is the pump modulation frequency and V_{in} (V_{out}) is the in - (out - of) phase TR signal. The function $h(t)$ is the unity impulse response $\Delta \equiv 2\pi/\omega_s$ is the time interval between two pulses (at frequency ω_s) and $\tilde{\beta}$ is a quantity that depend on the power of both the pump and the probe lasers, on the reflectivity at both pump and probe wavelengths and on the gain of photodetect. If we take the Fourier transform of eq. 3.102 the quantity $\tilde{h}(\omega_0 + l\omega_s)$ can be interpreted as the thermoreflectance response of the system when heated by a (continuous) Gaussian beam modulated at frequency $(\omega_0 + l\omega_s)$. The latter contains information about the thermal conductivity which can can be extracted by fitting the thermoreflectance response phase $\tan^{-1}(V_{in}/V_{out})$ to a model [162]. Following [163], in a typical experiment a pump laser heats a surface with an angle-independent intensity field $p_0(r) \sim A\exp\left(-2r^2/w_0^2\right)$, which induces a thermal response $\theta(r)$ in the sample. The latter can be evaluated by means of a probe beam with intensity $p_1(r) \sim \exp\left(-2r^2/w_1^2\right)$. Specifically, the probe laser measures an average temperature variation $\Delta T = E[\theta(r)]$ over the p_1 distribution. Thus we can write:

$$\Delta T = 2\pi A \int_0^\infty kG(k;\kappa,\alpha) e^{\pi^2 k^2 (w_0^2 + w_1^2)/2} dk, \tag{3.103}$$

where $G(k;\kappa,\alpha) = \kappa(q^2 + (2\pi k)^2)^{-1/2}$ is the Hankel transform of the solution of the heat

conduction equation in cylindrical coordinates for a semi-infinite plane - heated by a periodic and point-like source of unit power and angular frequency ω - and $q^2 \equiv i\omega/\alpha$. In the frequency domain, the individual components of the response are picked up with a lock-in amplifier. If we define the quantities $S(m) \equiv \Delta T(m\omega_s + \omega_0) + \Delta T(m\omega_s - \omega_0)$ and $D(m) \equiv \Delta T(m\omega_s - \omega_0) - \Delta T(m\omega_s + \omega_0)$ with m integer [164], we can write the variation of the reflectivity as:

$$\Delta R(t) = \frac{dR}{dT}\left(\sum_m S(m)e^{im\omega_s t} + \sum_m D(m)e^{im\omega_s t}\right) = \frac{R\sqrt{2}}{VQ}V_f(t), \tag{3.104}$$

where Q is the quality factor of the resonant circuit, V is the average voltage output of the detector and $V_f(t)$ is the (complex) *rms* voltage measured by the lock-in amplifier. The phase of the measured signal can be extracted from

$$\frac{V_{in}(t)}{V_{out}(t)} = i\frac{\sum_m S(m)e^{im\omega_s t}}{\sum_m D(m)e^{im\omega_s t}}. \tag{3.105}$$

3.4 Chapter overview

Summarising this chapter, we have derived the Onsager reciprocal relations for transport coefficients and the Green-Kubo (GK) formula for thermal conductivity within the linear response theory formalism, discussing the hurdles for its numerical implementation, and we have given an introduction to the Boltzmann transport equation (BTE). Then we have explained the details about the most relevant phonon scattering mechanisms in the contest of thermal transport. Finally, we have obtained the expression of the lattice conductivity with respect to the linearised BTE. We have concluded with a summary on the most relevant methods to extract the value of κ from experimental measurements. This chapter marks the end of our discussion about the theoretical methods employed during this thesis. In the next chapter we are going to present recent development on pristine and intrinsically doped boron arsenide transport properties, to then show our results concerning the effect of impurities on the BAs thermal conductivity in chapter 5.

4

Introduction to boron arsenide

High thermal conductivity materials are of paramount importance for thermal management applications in electronic devices, especially in case of an increased power density.

Boron arsenide (BAs) is a binary semiconductor with a cubic zincblend fcc structure (space group F43m), a reported lattice constant of 4.78 Å and the experimentally reported (indirect) electronic band gap is (1.8) 1.5 eV. First principles calculations also show that the n and p - types mobilities of BAs are respectively 1400 and 2110 $cm^2/(V \cdot s)$ [165], a result that stems from polar scattering suppression and reduction of inter-valley transition mediated by large-wavevector optical phonons [165], the latter being related to its large phonon acoustic-optical (a-o) band gap.

Although the first attempts to synthesise BAs date back to the 1950's, only in recent years have high quality crystals been produced [166]. If the first measurements of the defect laden BAs room temperature thermal conductivity reported values around $\sim$ 200 $W \cdot K^{-1}m^{-1}$ [167], high purity crystals present a value near $\sim$ 1300 $W \cdot K^{-1}m^{-1}$, i.e. one order of magnitude larger [168, 169, 170] and in agreement with several *ab initio* calculations [171, 102, 170].

Thus, the thermal conductivity of BAs is comparable with the one of diamond and this make it a promising candidate for thermal management and electronic applications along with its high n and p mobility. The comparison between old and new κ at room temperature raises two questions:

- Why is the pristine κ of BAs so high?
- How is κ affected by impurities?

Related to the first question, the failure of the Slack's model [172] in the case of high quality crystals can be attributed to how phonon scattering is treated. This strongly depends on the large mass mismatch between boron and arsenic and has profound consequences upon heat transport, as we will see in the following section. Related to the second question, we would like to understand what kind of mechanisms make difficult to achieve high values of the thermal conductivity and how defects, either intrinsic or extrinsic, affect the thermal transport coefficient.

In this chapter we review the recent findings about the behaviour of the pristine BAs κ and then summarise previous results about the effects induced by intrinsic defects on phonon thermal transport. We reserve the analysis about relevant extrinsic dopants - one of the main results of this thesis - to the next chapter. Since the main contribution to the boron arsenide conductivity comes from phonons, for the rest of this and the next chapter we refer to it as κ_{ph}. Finally, we recommend to the reader the work of Kang et al. [166] for a general overview of the experimentally measured electronic, optical, thermodynamical and mechanical properties of pristine boron arsenide.

4.1 Phonon band structure and pristine conductivity

Theoretical calculations and experiments have identified a set of rules that an insulator or semiconductor needs to follow in order to have a large thermal conductivity. These rules can be summarised into the effective model developed by Slack [172]:

$$\kappa_{\text{ph}} = A \frac{\langle M_a \rangle \theta^3 \delta}{\gamma^2 n^{2/3} T}, \tag{4.1}$$

where $\langle M_a \rangle$ is the average atomic mass inside the unit cell, δ^3 is the volume per number of atoms, θ is the Debye temperature, γ is the averaged Grüneisen parameter and n is the number of atoms in the unit cell. The value of A depends on γ and is roughly of the

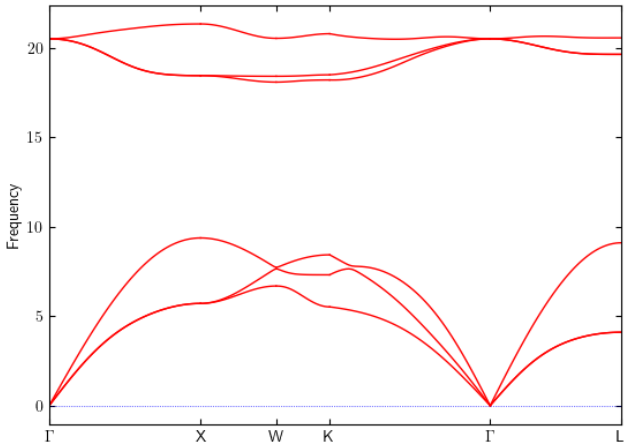

Figure 4.1: Phonon band structure obtained through application of the VASP [8, 9, 10] and Phonopy [1, 2] packages. The bunching of acoustic frequencies is noticeable at the K point.

order of $\sim 10^{-8}$. Slack's Model is very instructive as it clearly shows that to have high values of κ_{ph} at a given temperature we need few atoms per unit cell, small Grüneisen parameter, large volume per atom and high Debye temperature. From a first principles perspective small γ and n means weak anharmonicities and few channels for scattering events at the same time. Also, high θ and δ imply stiff bonds and light atoms.

In boron arsenide the phonon spectrum presents a large acoustic-optical band gap and acoustic phonon bunching - namely, the grouping of different frequencies near a certain wavevector - as a consequence of the large mismatch between the B and As masses, see figures 4.1 and 4.2. This has profound influence on the thermal properties.

Having a large a-o gap reduces the contribution from high frequency optical modes to the heat transport (as they are exponentially suppressed by the heat capacity) and more importantly it decreases their importance in suppressing the acoustic phonons lifetimes. To prove the latter, we can define the scattering phase space for the three-phonon anharmonicity as [173]:

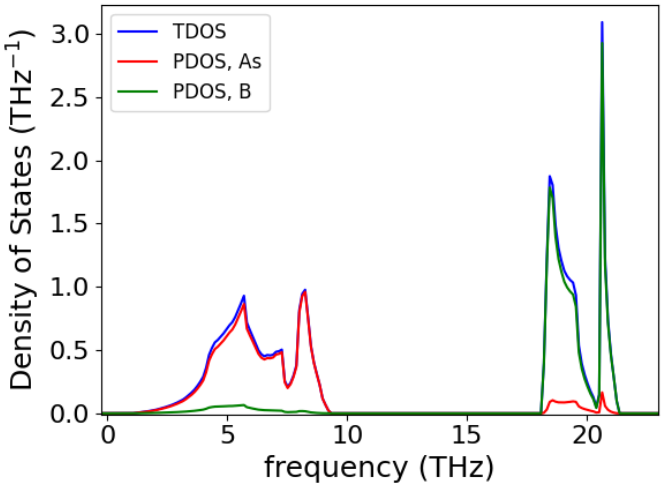

Figure 4.2: Total and projected phonon density of states obtained through application of the VASP [8, 9, 10] and Phonopy [1, 2] packages. In the acoustic range As dominates the phDOS behaviour in virtue of its much larger mass.

$$P_3 = \frac{2}{3\Omega}\sum_b \int d^3q \left[\frac{1}{2}D_\lambda^- + D_\lambda^+\right] = \frac{1}{\Omega}\sum_b \int d^3q D_\lambda^+, \tag{4.2}$$

with

$$D_\lambda^\pm \equiv \sum_{b',b''} \int d^3q' \delta(\omega_{b,\vec{q}} \pm \omega_{b',\vec{q}'} - \omega_{b'',\vec{q}\pm\vec{q}'-\vec{G}}), \tag{4.3}$$

where $\Omega = n_j V_{\mathrm{BZ}}$ is a normalisation factor, with n_j being the number of branches with Brillouin zone volume V_{BZ}. The herein defined P_3 measures the number of channels available for scattering according to the energy conservation principle. We also recognise that the expressions for $D_\lambda^\pm$ contribute to define $(\partial n_\lambda/\partial t)_{sc.}$, see eq. 3.62. Clearly having a small scattering phase space does increase the thermal conductivity as there are less states phonons can scatter into via third order anharmonic processes. This has been explored in [173] where a negative correlation between κ_{ph} and P_3 has been found for several binary compounds through an adiabatic bond charge model of the dispersion relations. In BAs in particular the $a + a \longleftrightarrow o$ and the $a + o \longleftrightarrow o$ processes are prevented and largely reduced, respectively, with the transport dominated by

$a + a \longleftrightarrow a$ events instead. This can be further understood in terms of the simple Debye-Eistein model. If we take take the dispersions to be linear isotropic ($\omega_{ac,\vec{q}} \equiv v|\vec{q}|$) and constant ($\omega_{opt,\vec{q}} = \omega_o$) for acoustic and optical modes respectively and with a cutoff for integration q_D, we obtain:

$$P_3[a + a \longleftrightarrow o] = \frac{9}{\omega_o}\left[\frac{2\omega_0}{5q_D v} - \frac{\omega_o^2}{(q_D v)^2} + \frac{2\omega_o^3}{3(q_D v)^3} - \frac{\omega_o^6}{30(q_D v)^6}\right]. \tag{4.4}$$

In a realistic situation ω_o represents the highest optical frequency. Taking $(\omega_o', v') = \beta(\omega_0, v)$, we can see that $P_3 \longrightarrow P_3/\beta$. In a binary compound it can be easily noticed that the scaling factor β grows with the mass ratio between the two elements of the unit cell and this explains the role played by the mismatch between As and B masses in leading to low three-phonon scattering rates. Furthermore the bunching of acoustic phonons prevents them from decaying into other acoustic phonons by anharmonic N and U processes due to a general theorem that states that modes cannot scatter into other states with higher phase velocity [174].

Scattering from isotopes is also reduced: in a binary semiconductor, the fact that the square norm of a phonon state grows with the atomic mass makes the boron contribution to the phonon-isotope interaction much smaller than for the arsenic. Moreover As appears to be isotopically pure.

The iterative solution of the BTE for BAs also shows that most of the three-phonon processes are not resistive, i.e. they increase the thermal conductivity. These considerations also hint that other interactions where U-processes are dominant might play a relevant role into establishing the experimentally measured value of the BAs κ_{ph}. If we consider three-phonon and phonon-isotope interaction only, the calculated room temperature thermal conductivity of BAs is about $\sim 2500\ \text{W}\cdot\text{K}^{-1}\cdot\text{m}^{-1}$ which is almost twice the experimentally reported value as shown in fig. 4.3 and previously computed in ref. [171].

It has therefore been suggested that other mechanisms may reduce the conductivity further. Of particular relevance are the four-phonons scattering processes, for reasons

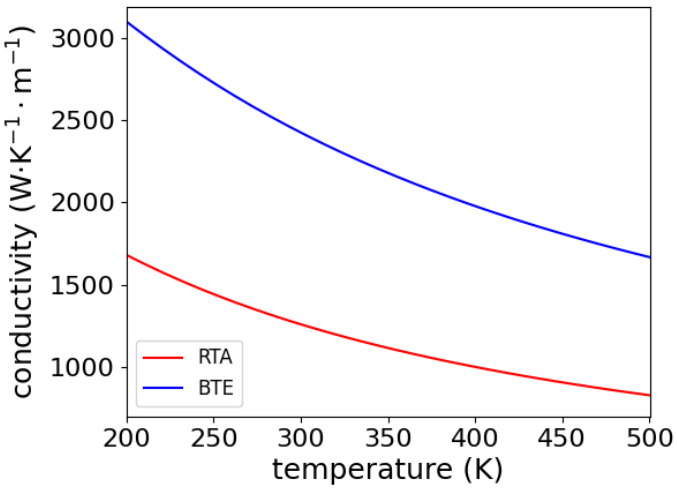

Figure 4.3: Thermal conductivity as a function of temperature, RTA and full iterative solution. Only three-phonon and phonon-isotope scattering are considered.

that can be summarised as follows. First of all their importance is expected to increase at medium and high temperature, since the corresponding rates w_4 grows as T^2 ($w_4/w_3 \sim T$). Furthermore, the conductivity of several materials like diamond, silicon and germanium present a decrease of 30% at 1000K which has been attributed to the four-phonon rates [103]. This reduction is even larger in the case of Lennard-Jones argon (60% at 80 K). In the particular case of optical phonons, high order ($n \geq 4$) scattering events can dominate the suppression of the heat carrier lifetimes even at low - T as also suggested by normal mode analysis.

We need to stress that although the four-phonon processes can be important, their relevance is mostly related to the vertices constructed with the fourth anharmonicity of the energy expansion. Although the second-order three-phonon events possess the same order of magnitude as the four-phonon, they are generally forbidden by energy and momentum conservation as either the ingoing and outgoing states must belong to the K - mesh. Since $N(3;2nd)/N(4;1st) \sim 10^{-3} - 10^{-5}$, we can generally neglect these second order processes.

In the particular case of boron arsenide, calculations performed by Feng et al. [102] and experiments from Tian et al. [170] have proven that four-phonon scattering is of

paramount importance as it reduces the conductivity from $\sim 2500\,\mathrm{W\cdot K^{-1}\cdot m^{-1}}$ to about the experimentally observed value. Feng et al. performed their calculations under the single mode RTA assumption, where the four-phonon events are dominated by inner interband Umklapp scattering while the three-phonon processes are dominated by intraband Normal scattering. Also, in BAs the optical phonons lifetimes are reduced by 60 % at 1000 K when fourth order anharmonicity is included. The reason behind the importance of the four-phonons events is largely due to the small third-order scattering phase space. Indeed, while the aforementioned large a-o band gap and phonon bunching strongly restrict the number of available states that phonons can scatter into through the three-phonons vertex, these restrictions do not occur at the four-phonons level. For example at 21 THz we have $N(3\mathrm{ph})/N(4\mathrm{ph}) \sim 20/10^7$. This behaviour is generally expected for binary semiconductors and insulators where a large difference between the masses of the constituent atoms is present. A thorough analysis that shows when this is the case has been performed by Ravichandran and Broido [175] where the importance of selection rules has been highlighted.

It has also been shown that the interplay between three- and four-phonons scattering processes is also responsible for the non-monotonic pressure dependence of the BAs thermal conductivity [176]. If only the third order anharmonicity is included we have $d\kappa_{\mathrm{ph}}/dP < 0$ in boron arsenide [177]. This result stems from the large m_{As}/m_B ratio, which in turn is responsible for the de-bunching of the acoustic phonons at high pressure (different frequencies increase differently with pressure) and consequently of the increase of the (dominant) *aaa* scattering phase space, something that *per se* cannot be predicted with the Slack's model. When the fourth anharmonicity is included the *aaoo* and *aaao* processes weaken for pressures lower than 50 GPa, thus leading to $d\kappa_{\mathrm{ph}}/dP > 0$, while at pressure higher than 50 GPa the behaviour is dominated by the three-phonon *aaa* scattering which decreases the conductivity. A temperature dependent maximum of $\kappa(P)$ is observed in BAs.

The lattice thermal conductivity of cubic BAs can be evaluated efficiently with the methodology introduced in the previous chapter, see Eq. 3.95:

$$\kappa_{\rm ph} = \frac{1}{3}\,{\rm Tr}\Big[\kappa^{\alpha\beta}\Big] = \frac{k_B}{\Omega_s}\sum_{\lambda}\left(\frac{\hbar\omega_\lambda}{k_B T}\right)^2 n^0_\lambda(n^0_\lambda+1)v_\lambda L_\lambda\,, \tag{4.5}$$

with

$$L_\lambda \equiv \tau^0_\lambda(v_\lambda + \Delta_\lambda[F_\lambda]) \tag{4.6}$$

and

$$\tau^0_\lambda = \left[\frac{1}{\tau^{\rm 3ph}_\lambda} + \frac{1}{\tau^{\rm 4ph}_\lambda} + \frac{1}{\tau^{\rm iso}_\lambda} + \frac{1}{\tau^{\rm def}_\lambda}\right]^{-1}, \tag{4.7}$$

where three-, four-, and defect-mediated two-phonon scattering processes [178, 103] are considered. Three-phonon scattering is included in the self-consistent part Δ_λ, while the remaining processes are present only in the expression of τ_λ (single mode relaxation time approximation or SMRTA). We repeat that the third order anharmonicity is dominated by Normal processes while the four-phonons involve mostly Umklapp processes [102]. The anharmonic three- and four-phonon scattering rates can be evaluated from first principles by computing the third and fourth-order force constants [103, 102] while to evaluate the phonon-isotope and phonon-substitutional interactions we use the formulation introduced in the previous chapters, refs. [106] and [99, 100] respectively, along with a distribution of uncorrelated substitutional defects.

4.2 Intrinsic defects

Obtaining high quality BAs crystals is not a simple task due to impurities that hinder the thermal transport in samples, We can ask what kind of defects are present in boron arsenide and how they affect its thermal conductivity. In recent years the role played by several intrinsic impurities have been explored [167, 179, 180]. Here we will review the literature concerning vacancies and antisites.

4.2.1 Vacancies and antisites

Ab initio calculations highlighting the role of vacancies in reducing the thermal conductivity of boron arsenide have been reported by Protik et al. [181]. One peculiarity that sets vacancies apart from other point defects is the nature of their associated perturbation. Previous models [182, 183] treated the scattering from vacancies at the Born approximation level and with the corresponding perturbation split in mass and bond parts. In particular, the last term was split in two contributions. The first one was the difference - treated at the harmonic lattice level - between the energies of the defect-laden and the pristine systems, with the supercell taken as in the non defective case. The lack of methods - at that time - to reliably compute the interatomic force constants was overcome with the virial theorem, so that this term could be reformulated as a kinetic energy difference. The second contribution was due to lattice relaxation, parametrised empirically and assumed to be small. These approximations resulted in a vacancy perturbation containing only a mass part. However, realistic calculations without empirical parameters have proven that this cannot be done in the case of BAs [181]. In particular it has been observed that a careful treatment of vacancies requires the consideration of the induced bond perturbation V_K only ($V_M \equiv 0$), since the detached atom does not contribute to thermal transport [184]. This can be proven mathematically if we consider the classical equation of motion for a vacancy:

$$m_i \ddot{u}_i = -\sum_j \tilde{K}_{ij} u_j = -\sum_j K^0_{ij} u_j - \sum_j (\tilde{K}_{ij} - K^0_{ij}) u_j. \tag{4.8}$$

We assume that the vacancy is in site-0 so that $m_0 \ddot{u}_0 = \tilde{K}_{0,j} = 0 \; \forall j$ meaning that all the linkages have been removed. The matrices $\tilde{K}_{ij}(K^0_{ij})$ are the IFCs for the defect laden (pristine) system. Thus the perturbation near the removed atom is $\sim K^0_{ij}$ meaning that a low-order perturbation theory is unsuited to study this kind of defects. In particular for the case of BAs the complete T-matrix approach has to be used as the Born approximation underestimates (overestimates) the scattering rates at low (high) frequencies, hence leading to incorrect predictions of the effects on the thermal conductivity for concentrations higher than 0.01 %. Finally it can be seen that the

previously mentioned RK mass model devised by Klemens and Ratsifaritana strongly overestimates (underestimates) the impact of As (B) vacancies because of its unrealistic ω^2 behaviour, because the effect of lattice relaxation around the removed atom is neglected and because the mass difference between arsenic and boron results in a much larger projection of the (average) phonon eigenvector components on the former than on the latter [185].

Concerning antisites, experiments and first principles calculations [180] have delved into their role in suppressing the BAs thermal conductivity. Aberration-corrected scanning transmission electron microscopy has shown an increased (decreased) intensity in the B (As) concentration in samples, which suggests the presence of As_B and B_{As} antisites in appreciable concentrations. This analysis has been supported and deepened by first principles calculations proving that the formation energy for antisite pairs (~ 2 eV) is much smaller than for vacancies or single antisites in p-doping conditions. This suggests that pairs As_B-B_{As} may be present in high concentrations: from STEM analysis the defect concentration has been estimated to be $\sim 6.6{\cdot}10^{20}$ cm^{-3}. The calculated thermal conductivity in presence of this concentration of correlated antisites is about 100 $W \cdot K^{-1} \cdot m^{-1}$ at room temperature, much lower than the pristine value but also sensibly lower than the defected conductivity value reported in ref. [167].

5

Substitutional impurities in boron arsenide

[1] The role played by intrinsic defects has been summarised in the previous chapter where it has been highlighted that κ_{ph} may be reduced by one order of magnitude at typical doping concentrations. Harnessing the high p- and n- mobilities of a boron arsenide for electronic applications requires doping it with external impurities. Since this may have a detrimental effect on the thermal properties of the material itself, extrinsic dopants with possibly a low impact on BAs κ_{ph} should be identified.

At the present date there is no comprehensive study about the effect of external substitution atoms, although many defects in their neutral and charged state have been explored with reference to their stability and energy of formation [187, 188]. Impurities belonging to the column IV of the periodic table are interesting because of their relatively low formation energies and because they can behave either as donors or as acceptors, depending on whether they replace As or B. In particular, the high p-dopability of BAs has been recently studied [188, 189].

First principles calculations, photoluminescence and electron paramagnetic resonance experiments have been used to study if dopants like C and Si, when behaving as acceptors, might affect the BAs-conductivity. These elements might be present as impurities in boron precursor powders and boride based compounds. Here we show how each dopant in group IV (C, Si, and Ge), in its neutral and charged forms, affects the thermal conductivity of BAs. This unveils a general trend, where neutral defects reduce

[1] The content of this chapter has also been addressed in ref. [186].

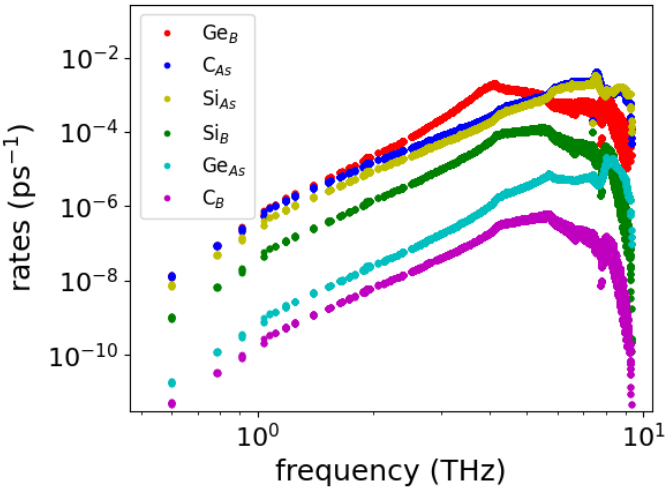

Figure 5.1: Acoustic phonon-impurity scattering rates vs phonon frequency, including only the mass effect contribution. The doping concentration is fixed at $3.26 \cdot 10^{18}$cm^{-3}.

the thermal conductivity more strongly than charged ones. We offer an interpretation in terms of the change in orbital occupation between the original and substituted system. We also highlight the initially counter-intuitive fact that, even for substitutions involving a large mass-difference value, the mass-difference scattering can be small. Finally, we show that in BAs excessive doping beyond the Fermi level pinning point activates phonon-donor scattering events, which can either slow down the decrease of thermal conductivity or cause it to plummet, depending on the type of impurity. This should be considered in future applications of BAs. Remarkably, we find that phonon scattering by C_B and Ge_{As} dopants is exceptionally weak. As a result, high BAs κ_{ph} values can be achieved even for high defect densities. This makes C_B and Ge_{As} impurities ideal n-type and p-type dopants respectively.

5.1 V_M - scattering

Phonon transport in BAs is peculiar in the sense that it is dominated by phonons in a narrow window of frequencies between 4-8 THz. This is due to several features in BAs including a large frequency gap between acoustic and optic phonons, a narrow optic phonon bandwidth, a bunching together of acoustic phonon branches and exception-

	C	Si	Ge
B	0.1	1.6	5.7
As	0.8	0.6	0.03

Table 5.1: Absolute mass difference for the three impurity atoms (C, Si and Ge) normalized by the host atom mass (B or As).

ally weak four-phonon scattering. This combination of features gives rise to unusually large contributions to κ_{ph} from acoustic phonons in this particular range [171, 170]. Let us first look at the scattering produced by the mass difference, eq. 3.70. The absolute mass difference normalized by the host atom mass is shown in table 5.1. Ge_{As} and C_B substitutions correspond to the smallest mass differences, since Ge and As and C and B are contiguous in the periodic table. For the rest of the substitutions the mass difference is large.

In contrast with the case of single-species compounds, the magnitudes of the scattering rates in fig. 5.1 do not follow a monotonic behavior with respect to the normalized mass difference: in binary compounds with a large mass ratio of the constituent atoms, like BAs, almost all acoustic phonon modes throughout the Brillouin zone involve dominant motion of the heavy As atoms, while the light B atoms remain relatively stationary. As a result, mass defects placed on the heavy atom sites lead to strong phonon scattering while those placed on the light atom site become almost invisible to phonons and provide only weak scattering [185]. An approximated analytical expression for the mass-difference scattering rate in large mass-ratio binary compounds was given by Lindsay et al. [185], and experimentally verified by Chen et al. [190].

5.2 V_K - scattering

Figure 5.2 shows the V_K - only (eq. 3.71) scattering rates at the concentration of 3.26 $\cdot$ 10^{18} cm^{-3}. The frequency range between 4 and 8 THz is highlighted with dashed vertical bars. The plots show that (i) the phonon scattering rates are consistently larger for bond distortions involving C, Si and Ge impurities in their neutral states compared

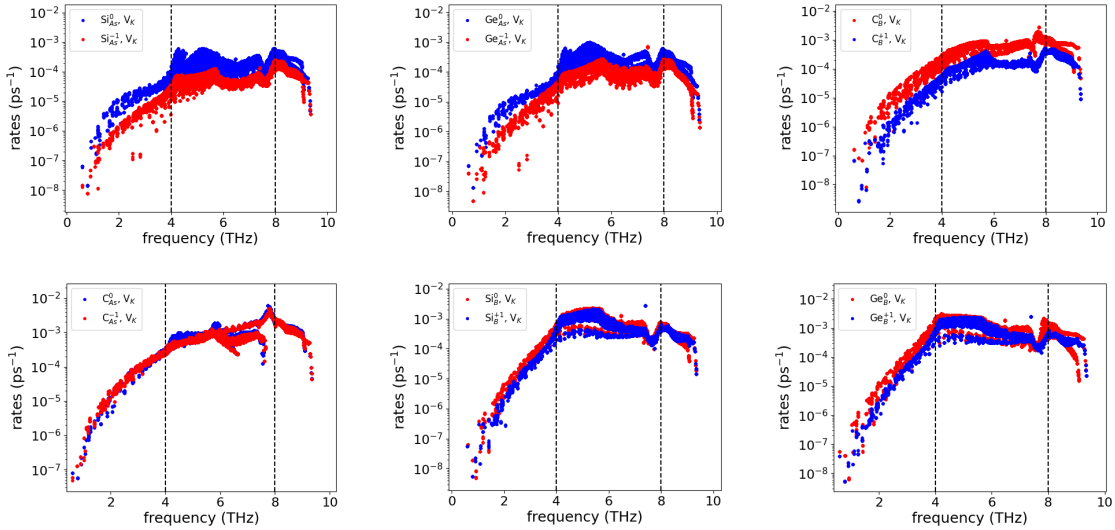

Figure 5.2: Acoustic phonon-impurity scattering rates in BAs including only the bond distortions to isolate differences between neutral and charged dopants. Red (blue) points are for charged (neutral) impurities. Dashed vertical lines at 4 THz and 8 THz identify the main frequency region where phonons contribute to the thermal conductivity of pristine BAs. Impurity density is $3.26 \cdot 10^{18}$ cm^{-3}.

with those in their charged states, and (ii) Si_{As}, Ge_{As} and C_B dopants lead to noticeably weaker bond defect scattering than do C_{As}, Si_B and Ge_B. Since Ge and C also result in weak small mass differences when replacing host atoms As and B, the plots confirm the unusually weak total phonon-defect scattering rates for Ge_{As} and C_B dopants.

To assess the importance of V_K and better summarise the phonon-defect scattering rates results we find useful to define and evaluate the following descriptor for both charged and neutral states:

$$D_{\text{def};K} \equiv \frac{1}{N} \sum_{\lambda} \tau^{-1}_{\lambda;K} [\theta(\omega_\lambda - \omega_1) - \theta(\omega_\lambda - \omega_2)], \tag{5.1}$$

where N is the number of $\vec{q}$ - points per branch in the reciprocal space grid, ω_1 and ω_2 are 4 and 8 THz, respectively, θ is the Heaviside step-function and $\tau^{-1}_{\lambda;K}$ is the phonon-defect scattering rate evaluated by including the V_K perturbation only. In Eq. 5.1 we consider an impurity concentration of one defect per unit cell, as using a more dilute

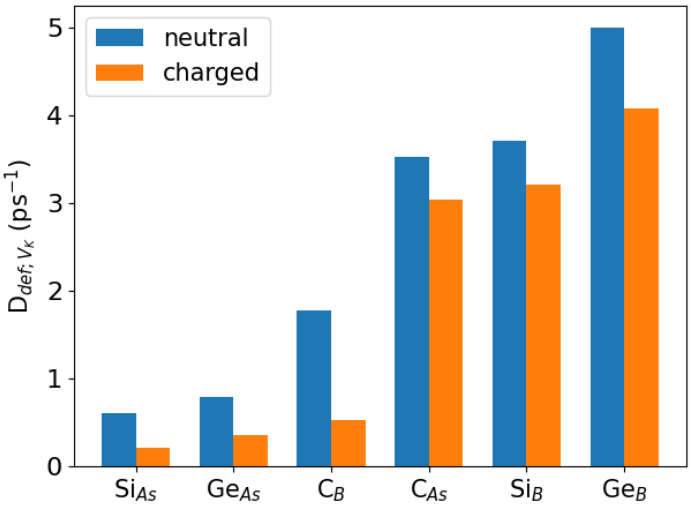

Figure 5.3: V_K - descriptor for charged and neutral rates.

value would only scale $D_{\text{def;K}}$ by a χ factor. The evaluated descriptor is shown in fig. 5.3 for dopants in the neutral and charged states.

We find that phonon scattering by neutral defects is generally stronger than that by charged defects. We can possibly attribute this general phenomenon to the fact that the ionised charged states more closely resemble the electronic structure of the original host: when an atom in column IV replaces an As (B) atom, it tends to get charged by accepting (donating) an extra electron, thus becoming iso-electronic with the original atom it has substituted. If the impurity remains neutral, however, the extra hole (electron) present at the defect site is responsible for bond perturbations on the crystal structure that do not take place when dealing with ionised states. This effect is most noticeable in Ge_{As}, C_B and Si_{As}, as shown in fig. 5.3. These three impurities also have weaker bond-defect scattering than do Ge_B, Si_B and C_{As}.

5.3 Total scattering

In Figures 5.4-5.9 we report the phonon-defect scattering rates at concentration 10^{18}cm^{-3} for C, Si and Ge-doped BAs (either acceptors and donors). We evaluate the contribution of the total and bond perturbation alone for both neutral and charged states.

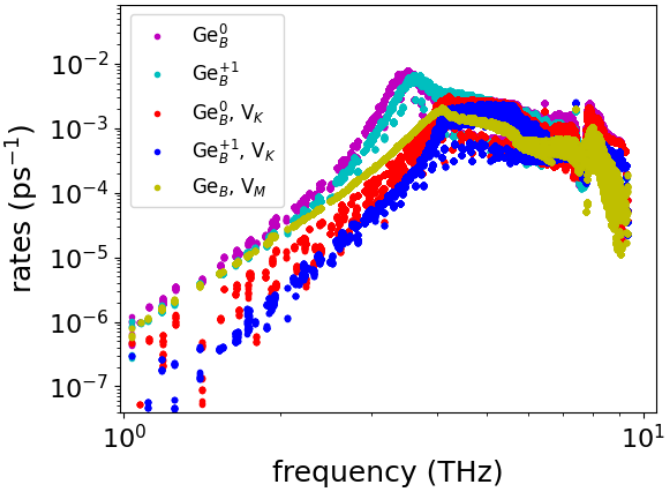

Figure 5.4: Acoustic phonon-defect scattering rates vs phonon frequency at $3.26 \cdot 10^{18}$ cm^{-3}, Ge_B case.

In the Ge_B case, see fig. 5.4, the V_K - rates are slightly smaller (larger) than those resulting from V_M at low (medium) frequency. The combined effect of the two perturbation gives an overall scattering that reaches 10^{-2} ps^{-1} in the medium ω-range. We note, also, a non monotonic behaviour of τ_V^{-1} as a function of the frequency. The C_{As} bond perturbation also produces phonon-defect scattering that can be compared with the mass-only effect, as we can see in figure 5.5. The rates behave monotonically with respect to frequency and the maximum value is slightly smaller than for Ge_B.

For the Si impurity (acceptor) in fig. 5.6, as in the carbon replacing arsenic case, the rates monotonically increase with the frequencies. However, they generally present a different behaviour with respect to the previous dopants. A large mass perturbation is here accompanied by a small change in the local bonds in either neutral or charged states and this is reflected on the interaction with phonons. V_M and V_K differ by about two orders of magnitude in the charged case. On the other hand a strong effect on the IFCs can be inferred from the donor Si rates in figure 5.7, where the impact of V_K is particularly noticeable in the medium frequency range. Like for the Ge-donor substitution, also in this case the trend with respect to ω is not monotonic.

Finally in figs. 5.8 and 5.9 we present the phonon-defect scattering rates upon donor-C

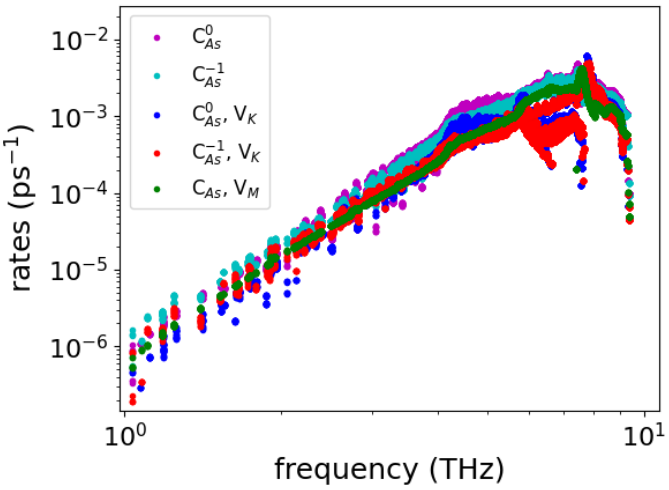

Figure 5.5: Acoustic phonon-defect scattering rates vs phonon frequency at $3.26 \cdot 10^{18}$ cm^{-3}, C_{As} case.

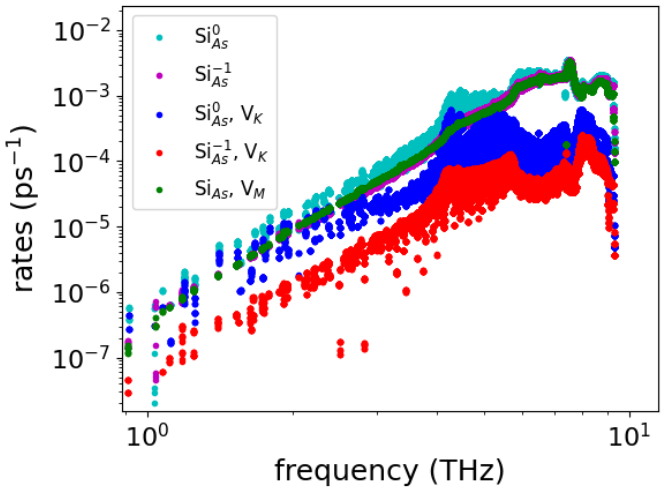

Figure 5.6: Acoustic phonon-defect scattering rates vs phonon frequency at $3.26 \cdot 10^{18}$ cm^{-3}, Si_{As} case.

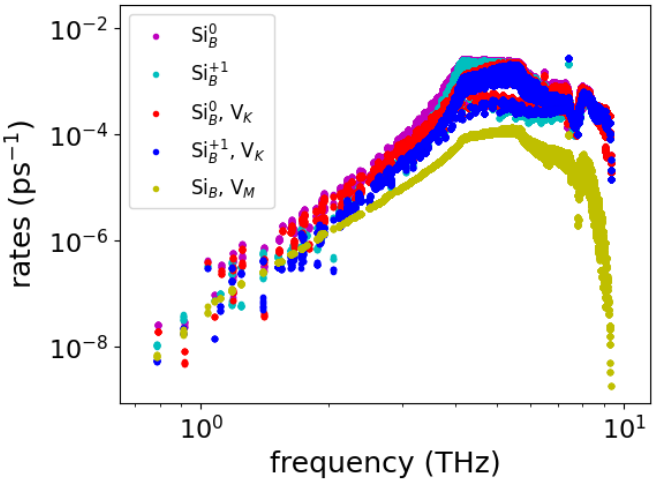

Figure 5.7: Acoustic phonon-defect scattering rates vs phonon frequency at $3.26 \cdot 10^{18}$ cm^{-3}, Si_B case.

and acceptor Ge substitutions respectively. In both cases the very weak effect of V_M is overcome by a much larger contribution from the IFCs variation such that total and pure V_K cases are not distinguishable. The global effect is anyway much smaller than for the remaining dopants with the maximum of $\tau^{-1}_{\lambda,\mathrm{def}}$ being $\sim 10^{-3}$ ps^{-1} in both cases and with C_B^{+1} producing a slightly bigger impact than Ge_{As}^{-1}. As seen in the Ge and Si substituting boron cases, the rates produced by C-donor are not monotonic with respect to the phonon frequencies as opposite to those from the Ge-acceptor.

5.4 Frequency shift

Point defects are a source of scattering and affect the lifetimes of phonons, but they can also potentially lead to a frequency renormalization. The shift induced by impurities is generally not considered in the weak doping limit, although it is expected to play a major role when considering the formation of alloys. To quantify the shift in the phonon frequencies we consider, in terms of the retarded Green's function G_0^+ of the the pristine system [110]:

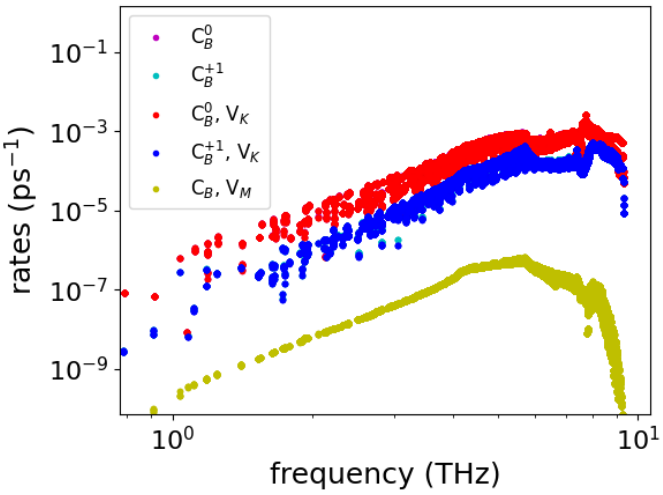

Figure 5.8: Acoustic phonon-defect scattering rates vs phonon frequency at $3.26 \cdot 10^{18}$ cm^{-3}, C_B case.

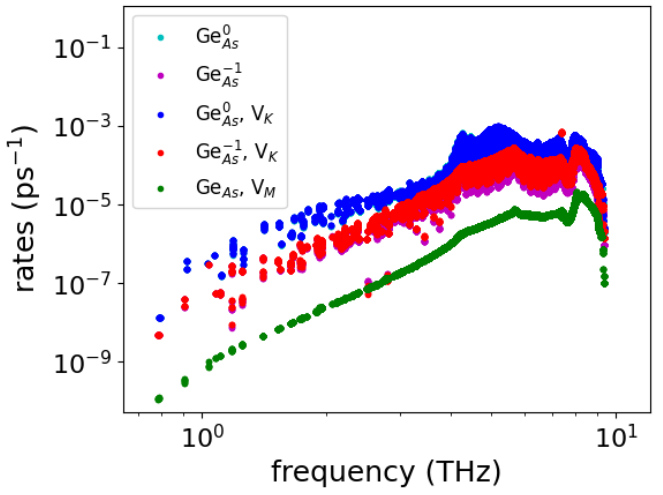

Figure 5.9: Acoustic phonon-defect scattering rates vs phonon frequency at $3.26 \cdot 10^{18}$ cm^{-3}, Ge_{As} case.

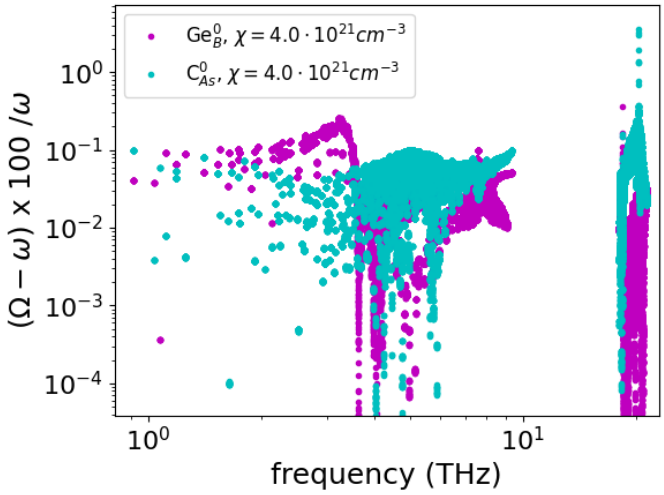

Figure 5.10: Frequency shifts normalised by the pristine BAs phonon frequencies and multiplied by a factor 100 for a concentration of $4.0 \cdot 10^{21}$ cm^{-3} in the case of neutral C_{As} and Ge_B.

$$\Omega_\lambda^2 = \omega_\lambda^2 + \chi \, \mathrm{Re} \left[\frac{\langle \lambda | \, T^+ \, | \lambda \rangle}{\langle \lambda | \, 1 + G_0^+ T^+ \, | \lambda \rangle} \right], \tag{5.2}$$

which stems from the Dyson equation $V = G_0^{-1} - G^{-1}$ where G is the Green's function for the defective system, G_0^+ is the retarded pristine Green's function, T^+ is the retarded T-matrix and Ω_λ are the renormalized frequencies. We assume that Ω_λ^2 scales linearly with the impurity concentration, in line with the dilute defect approximation adopted to compute the phonon-defect scattering rates. We evaluate the quantity $(\Omega_\lambda - \omega_\lambda) \cdot 100 \cdot \omega_\lambda^{-1}$, namely the percentage of how frequencies are shifted in virtue of doping, in fig. 5.10 and in the case of of neutral C_{As} and Ge_B at the concentration of $4.0 \cdot 10^{21}$ cm^{-3}, with the latter impurities presenting the strongest mass and bond perturbation. It is found that even at such large concentration the shift amounts to less than 1% of the frequencies and thus can be safely neglected.

5.5 Thermal conductivity

Figure 5.11 shows plots of the BAs thermal conductivity at room temperature (300 K) as a function of doping concentration for each of the six impurities considered. Solid lines correspond to the neutral impurity cases, while dotted lines are for the charged defects. At low concentrations, all curves merge to the pristine thermal conductivity value of around $\kappa_{ph} = 1200\,W \cdot m^{-1} \cdot K^{-1}$, where only three- and four-phonon scattering occurs [170, 171, 102]. With increasing impurity concentration, the behaviour of the thermal conductivity clearly reflects the behaviour of the phonon-defect scattering rates: at a given dopant density, the reduction of κ_{ph} is larger for impurities in their neutral states compared with those in their charged states. Colored horizontal arrows in fig. 5.11 indicate the differences between charged and neutral impurity concentrations that produce a 50% reduction in the BAs κ_{ph}. The consistently larger densities achieved for each of the charged impurities compared with their neutral counterparts highlight the weaker scattering of phonons for impurities in their charged states. The C_{As} and Ge_B defects suppress the thermal conductivity the most, with a 50% reduction to $\sim$ $600\,W \cdot m^{-1} \cdot K^{-1}$ at a defect concentration of $\sim 10^{19}$ cm^{-3}; Si_{As} closely follows, because its large mass variance dominates over the otherwise weak bond defect scattering. Since Si and C are known contaminants in BAs growth [188], the present finding that they strongly reduce the BAs κ_{ph} motivates synthesis approaches that minimize their presence, if maximum thermal conductivity is desired. Interestingly, Si_B does provide quite a large reduction of κ_{ph} in both the neutral and charged cases despite having relatively weak low frequency mass defect scattering rates, because the scattering induced by the bond perturbation is quite high between 4 and 8 THz, similar to both C_{As} and Ge_B. This effect clearly cannot be captured by a pure mass defect perturbation. The opposite holds for Ge_{As}: it gives the smallest reduction to the BAs thermal conductivity for both charged and neutral cases, where phonon-impurity scattering rates are about an order of magnitude smaller than those for the C_{As} substitution in the critical 4-8 THz range.

In the C_{As}, Ge_B and Si_{As} cases, see figs. 5.13, 5.12 and 5.14, the mass variance hides the effect produced by the structural relaxation and by the change in the local bonds to such

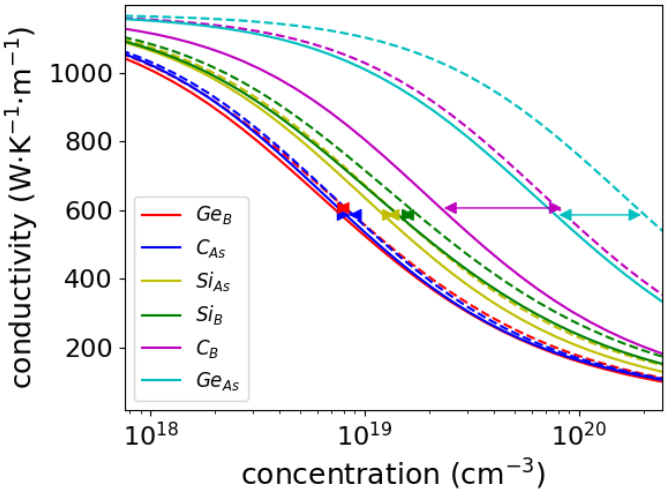

Figure 5.11: Lattice thermal conductivity of BAs vs doping concentration at 300 K. Solid lines: neutral impurities. Dotted lines: charged impurities.

degree that the difference between neutral and charged states cannot be appreciated at the κ_{ph}-level, especially in the Si_{As} case where the bond perturbation is already weak. Instead, the effect of V_K plays a much more relevant role when the mass variance is weak, that is in the Si_B, C_B and Ge_{As} cases as also reported in figures 5.15, 5.16 and 5.17. In particular, in the latter two it constitutes the largest component of the perturbation and the difference between neutral and charged states is more marked. Moreover, for the Si_B substitution, relatively weak rates at low frequency ($\sim<$ 4 THz) in the charged case are compensated by a much stronger perturbation at high frequency.

5.6 Effect of compensation

In fig. 5.11, each curve corresponds to the reduction of the BAs thermal conductivity assuming that the density of a particular impurity can be varied independently. We now consider a more complex behavior that might occur if the BAs growth process were governed by equilibrium thermodynamics. For low densities of the three dopants D=C, Si, Ge, the calculated formation energies for the charged acceptors, Si_{As}^{-1} , Ge_{As}^{-1} and C_{As}^{-1} , are much lower than those for charged donors [188, 187] so these impurities will form first. As the doping density increases and the Fermi level, ε_F, shifts towards

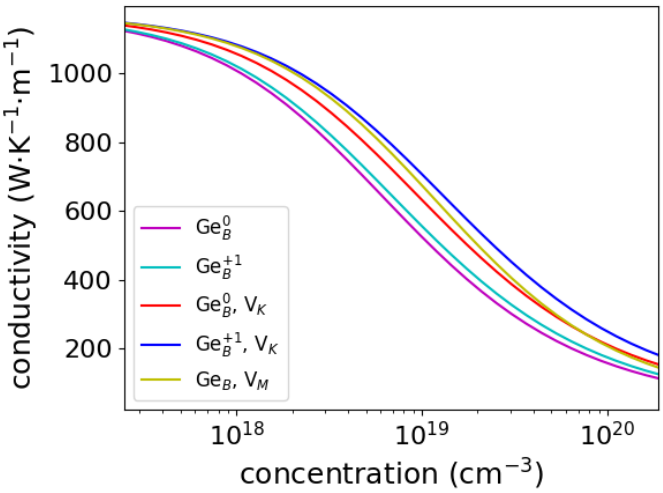

Figure 5.12: Ge_B doped thermal conductivity as a function of concentration at T = 300 K.

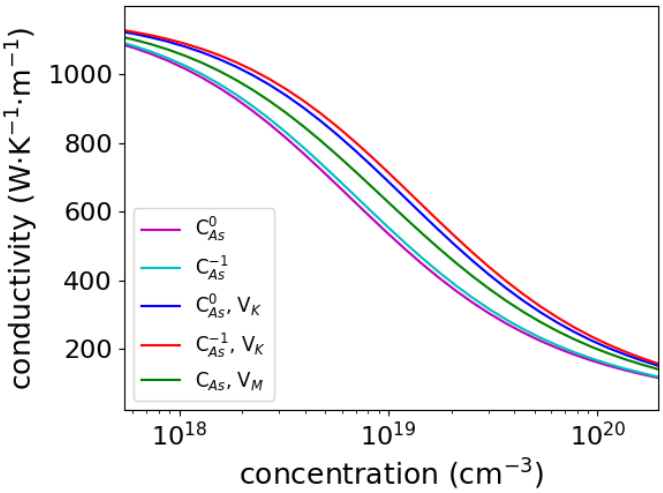

Figure 5.13: C_{As} doped thermal conductivity as a function of concentration at T = 300 K.

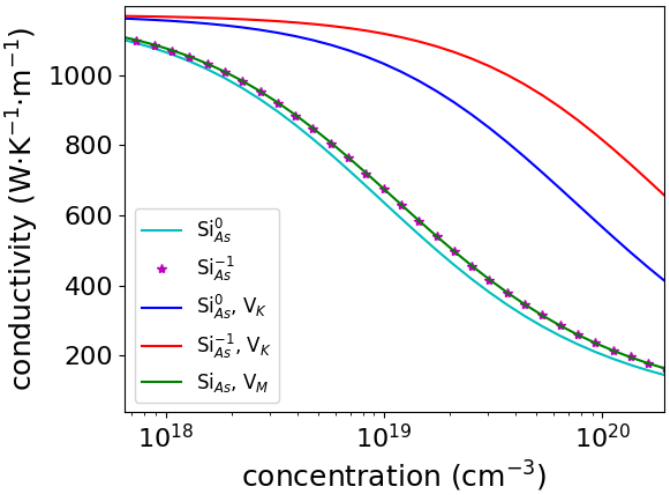

Figure 5.14: Si_{As} doped thermal conductivity as a function of concentration at T = 300 K.

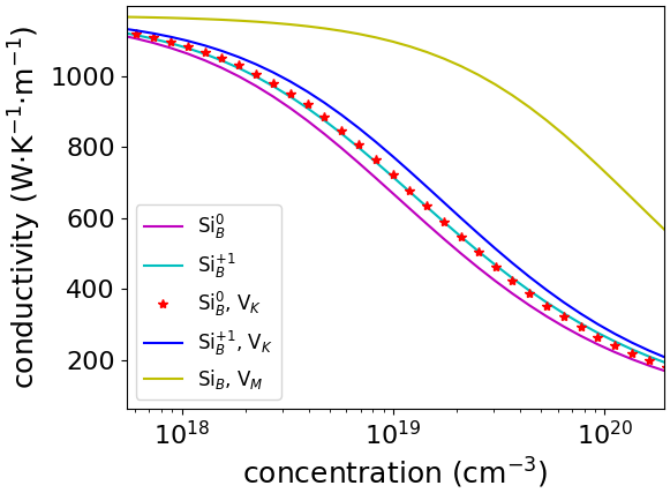

Figure 5.15: Si_B doped thermal conductivity as a function of concentration at T = 300 K.

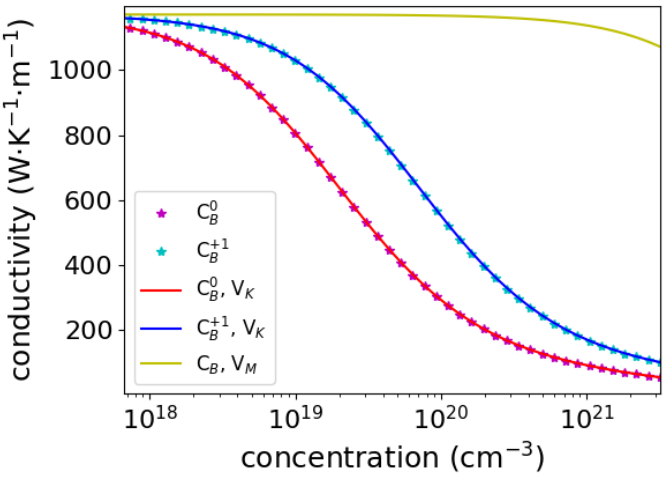

Figure 5.16: C_B doped thermal conductivity as a function of concentration at T = 300 K.

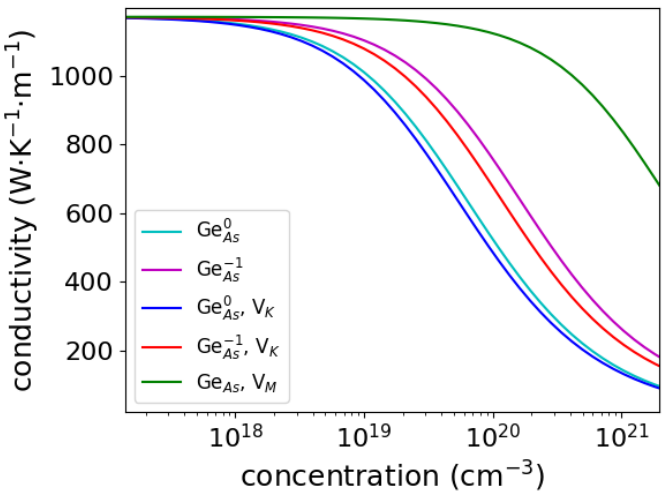

Figure 5.17: Ge_{As} doped thermal conductivity as a function of concentration at T = 300 K.

the valence band edge, the D-acceptor formation energies increase while D-donor formation energies decrease thereby increasing the probability of D-donor formation. At the crossing point of the acceptor and donor formation energies, acceptors and donors form with equal probability and ε_F becomes pinned. Thus, equilibrium growth thermodynamics mandates that beyond a certain concentration, adding more D-impurities will form not only D-acceptors but also compensating D-donors. In addition, temperature dependent mixtures of charged and neutral acceptors coexist because of the finite acceptor ionization energy. Therefore, understanding how donor compensation and the differences between neutral and charged defect scattering rates could shape the $\kappa(\chi)$ profile should be considered.

To model the effect of compensation we combine the effects of the neutral and ionised acceptors and of the donors to a single rates expression using Matthiessen's rule. To estimate the concentrations of charged and neutral impurities and compensating donors formed during growth, we impose the charge neutrality condition (previously defined in equation 2.86):

$$p - n = N_A^- - N_D^+, \tag{5.3}$$

where p, n, N_A^- and N_D^+ are, respectively, the hole, electron, ionised acceptor and ionised donor concentrations. We take the following pinning ε_F^*-values (in eV) for As-rich (B-rich) conditions: C: 0.4 (0.15), Si: 0.15 (-0.05), Ge: 0.25 (0.0) [187]. From equations 2.87 and 2.88, the standard expressions for p and n are:

$$p(\mu, T) \equiv \int_{-\infty}^{\varepsilon_{VBM}} D_h(\varepsilon)(1 - f(\varepsilon; \varepsilon_F, T))d\varepsilon \tag{5.4}$$

and

$$n(\mu, T) \equiv \int_{\varepsilon_{CBM}}^{\infty} D_e(\varepsilon) f(\varepsilon; \varepsilon_F, T) d\varepsilon, \tag{5.5}$$

where $D_h(\varepsilon)$ and $D_e(\varepsilon)$ are the hole and electron density of states (DOS), $\varepsilon_{\mathrm{VBM}}$ and $\varepsilon_{\mathrm{CBM}}$ are the valence band maximum and conduction band minimum, ε_{F} is the Fermi level and $f(\varepsilon;\varepsilon_{\mathrm{F}},T)$ is the equilibrium Fermi-Dirac distribution. A simple isotropic parabolic band model can be employed to evaluate the hole- and electron- DOS near the gap:

$$D_h(\varepsilon) = \frac{1}{2\pi^2}\left(\frac{2m_h^*}{\hbar^2}\right)^{3/2}\sqrt{\varepsilon_{\mathrm{VBM}}-\varepsilon}, \tag{5.6}$$

$$D_e(\varepsilon) = \frac{1}{2\pi^2}\left(\frac{2m_e^*}{\hbar^2}\right)^{3/2}\sqrt{\varepsilon-\varepsilon_{\mathrm{CBM}}}. \tag{5.7}$$

We take averaged effective masses $m_h^* \sim 0.56$ and $m_e^* \sim 0.4$ [188]. Now, given the acceptor and donor electronic levels ε_{A} and ε_{D} we consider

$$N_{\mathrm{A}}^- = \frac{N_{\mathrm{A}}}{1+4\cdot\exp((\varepsilon_{\mathrm{A}}-\varepsilon_{\mathrm{F}})/k_BT)} \equiv f_{\mathrm{A}}\cdot N_{\mathrm{A}} \tag{5.8}$$

and

$$N_{\mathrm{D}}^+ = \frac{N_{\mathrm{D}}}{1+2\cdot\exp((\varepsilon_{\mathrm{F}}-\varepsilon_{\mathrm{D}})/k_BT)} \equiv f_{\mathrm{D}}\cdot N_{\mathrm{D}} \tag{5.9}$$

along with $N_{\mathrm{A}}+N_{\mathrm{D}}=\chi$, where χ is the total concentration of impurities, and we define $g \equiv N_{\mathrm{D}}/N_{\mathrm{A}}$. The value of f_D can be safely assumed to be equal to one, since $(\varepsilon_{\mathrm{D}}-\varepsilon_{\mathrm{F}}) \gg k_BT$ for all the considered doping range. Therefore we have $N_{\mathrm{A}} = \chi/(1+g)$ and $N_{\mathrm{D}}^+ \simeq N_{\mathrm{D}} = g\chi/(1+g)$.

The definition of g is of paramount importance for the determination of the fraction of donors and acceptors. Here we have assumed that impurities are incorporated into BAs at growth - temperature $T_{\mathrm{growth}} = 1163$ K [170] and that diffusion processes are negligible, which results in fixed N_{A} and N_{D} when the temperature is lowered. To do this, we have first solved Eq. 5.3 by taking g at T_{growth} with

$N_{\mathrm{D}}^{+}/N_{\mathrm{A}}^{-} = \exp\left[-(E_{\mathrm{D}} - E_{\mathrm{A}})/(k_B T_{\mathrm{growth}})\right]$, where E_A and E_D are respectively the formation energies for the charged acceptor and charged donor state taken from [187]. The expression for g stems from the Gibbs free energy for the doped system, where the contribution from vibrational entropy has been neglected. The ensuing and fixed values of $N_{\mathrm{A}}(T_{\mathrm{growth}})$ and $N_{\mathrm{D}}(T_{\mathrm{growth}})$ have been utilised for each value of χ to evaluate f_A at $T = 300$ K.

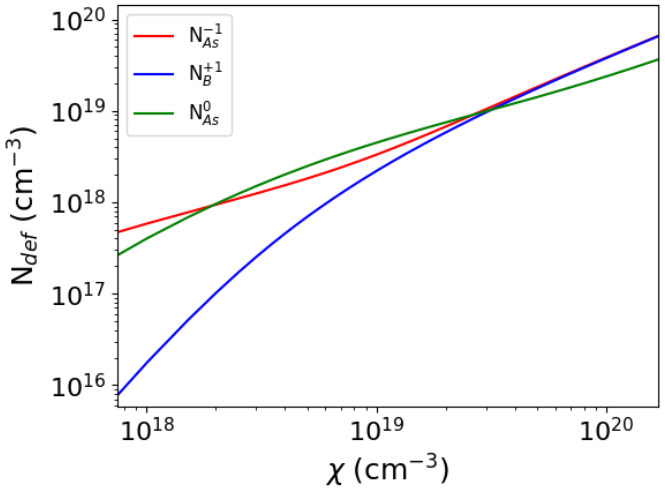

Figure 5.18: Charged and neutral acceptor and donor concentrations as a functions of the total concentration of impurities at 300 K, Ge-doping case.

The presence of three doping "regimes" can be noticed in the Ge case in fig. 5.18. For $\chi < 10^{18}$ cm^{-3} most of the defects are charged acceptors while for $\chi > 10^{19}$ cm^{-3} both donors and acceptors (charged state) increase linearly with the total concentration. We note also a χ-window in the $10^{18} - 10^{19}$ cm^{-3} range where Ge is present in large amounts as a neutral acceptor. If figure 5.19 we report the hole concentration with and without considering the compensation by donor impurities, in the stable As-rich growth conditions. It can be noted that the maximum hole doping is achieved in the case of Si impurities ($p > 10^{18}$ cm^{-3}), with the Ge case closely following. In the case of C defects the maximum of the hole concentration stabilises near 10^{17} cm^{-3}, i.e. one order of magnitude smaller, in virtue of its larger ionisation energy with respect to Si and Ge.

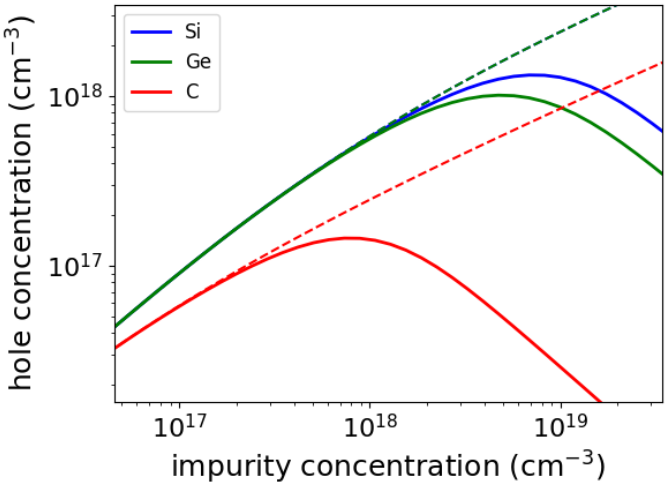

Figure 5.19: Hole concentration in As-rich conditions for Si, Ge and C impurities at 300 K. Continuous (dashed) lines include (neglect) the presence of donor compensation effects.

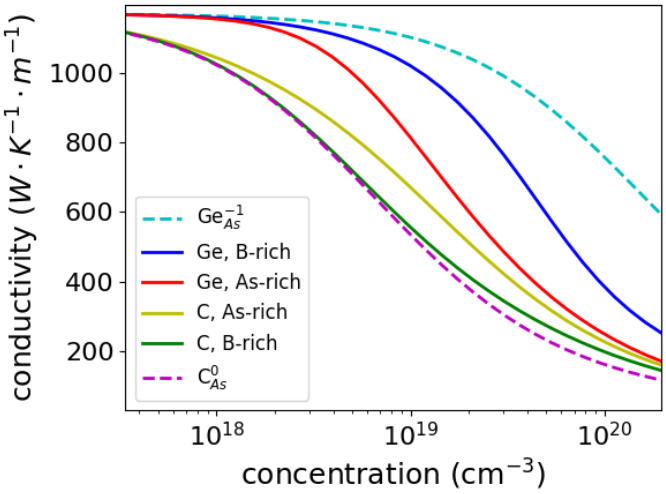

Figure 5.20: Lattice thermal conductivity of BAs vs impurity concentration at 300 K. Dotted lines: Ge_{As}^{-1} and C_{As}^{0} curves have been included from fig. 5.11 for comparison. Continuous lines: scattering from charged acceptors, neutral acceptors and charged donors has been included according to equation 5.10.

Finally, if we define the shorthand $V_{\text{uc}}\,\text{Im}\langle T^{+}_{\text{DEF}}\rangle_{\lambda}/\omega_{\lambda} \equiv \text{B}^{\text{DEF}}_{\lambda}$ for each type and state of defect, we have:

$$\frac{1}{\tau^{\text{def}}_{\lambda,\text{tot}}(\chi)} = N_A^- \text{B}_\lambda^{\text{ch.,acc.}} + N_A^0 \text{B}_\lambda^{\text{ne.,acc.}} + N_D^+ \text{B}_\lambda^{\text{ch.,don.}}. \tag{5.10}$$

In light of the generally different magnitudes of the phonon-defect scattering rates for As and B substitutions, casting eq. 5.10 in the κ_{ph} expression induces relevant changes. In the case of Ge doping, at lower densities $\text{Ge}_{\text{As}}^{-1}$ defects reduce κ_{ph} only slightly. But once $\text{Ge}_{\text{B}}^{+1}$ starts to form, κ_{ph} will decrease more rapidly due to the much larger scattering rates of the latter. The opposite behavior occurs for C doping since $\text{C}_{\text{As}}^{-1}$ scatters phonons more strongly than C_{B}^{+1}.

By including the scattering rates for charged and neutral acceptors and the compensating donors at the temperature of 300 K we have calculated the BAs κ_{ph} vs. impurity concentration curves in fig. 5.20. Solid lines show the Ge doping and C-doping cases for B-rich and As-rich growth conditions. The change of dependence in the case of Ge doping is particularly evident. When grown in B-rich conditions, BAs could in principle be p-doped with Ge to nearly 10^{19} cm^{-3}, without much decrease in the thermal conductivity, with somewhat smaller but still high κ_{ph} values achieved for the As-rich case. Beyond this doping level, the thermal conductivity would decrease more rapidly compared with the $\text{Ge}_{\text{As}}^{-1}$ - only case, with detrimental consequences for device heating. We note that As-rich conditions are known to be more favorable for growth, whereas growth of B-rich BAs can be hampered by formation of the subarsenide phase B_6As [188].

5.7 Discussion

With increasing Si, Ge and C impurity densities, free hole densities first increase, then saturate and finally decrease due to compensation from electrons ionized from increasingly large concentrations of donor atoms, as shown in fig. 5.19. Maximum hole densities of $2.0 \cdot 10^{18}$ cm^{-3}, $1.0 \cdot 10^{18}$ cm^{-3}, and $1.5 \cdot 10^{17}$ cm^{-3} are obtained for Si, Ge and C, respectively. The lower value for C results primarily from its larger acceptor ionization of 0.09 eV compared with the corresponding value of 0.03 eV for both Ge and Si, as calculated from first principles [187]. These results are for impurity

formation energies for the As-rich growth conditions expected to apply in current BAs synthesis. Ignoring donor compensation gives similar results for Si and Ge up to impurity densities of around 10^{19} cm^{-3}. These finding suggest that there is not much gain in hole density for impurity concentrations much above a few times 10^{18} cm^{-3}, especially when high thermal conductivity is desired.

For the experimentally achievable As-rich growth, Ge doping shows a clear advantage over C and Si doping as donor compensation starts to be important only at concentrations approaching 10^{19} cm^{-3}. More broadly, for all three dopants, the BAs κ_{ph} exceeds 600 W $\cdot$ m^{-1} $\cdot$ K^{-1} even at high dopant densities, thus retaining values far above those of common semiconductors such as Si (140 W $\cdot$ m^{-1} $\cdot$ K^{-1}) and GaAs (45 W $\cdot$ m^{-1} $\cdot$ K^{-1}). This could be a great advantage in applications where efficient heat dissipation is crucial. Furthermore, the results in fig. 5.20 suggest a complementary experimental way to determine if compensation doping is occurring by directly measuring the thermal conductivity. Further calculations and experiments may be envisaged in this way, to evaluate the effect of compensation on the thermal transport properties in semiconductors. Finally, we note that while charged C_B substitutions in the absence of C_{As} would give only minimal reduction of the BAs κ_{ph} up to high densities, use of C as an n-type dopant would be hindered by the large C_B formation and ionization energies [187, 188].

In conclusion, we have evaluated the thermal conductivity reduction induced by doping BAs with C, Si and Ge. Ge_{As} and C_B substitutions give exceptionally small reductions to the BAs thermal conductivity even at high densities. However, the large formation and ionization energies of C_B donors hinder their utility as n-type dopants and motivates a search for other candidates. Both Si and Ge achieve reasonably high hole densities while retaining high BAs thermal conductivity. Importantly, even at high impurity densities the BAs κ_{ph} significantly exceeds those of common semiconductors, highlighting its potential as a next-generation self-cooling functional material. An observable drop (enhancement) in thermal conductivity with respect to the charged D-acceptor case is predicted and explained upon Ge(C)-doping if we consider compensating donor scattering centers and the temperature/doping dependence for the acceptor activation. This imposes practical limitations to be considered when design-

ing BAs - based devices. It also suggests a direct alternative way to experimentally determine if a sample suffers from compensation doping. Finally, we have computationally identified a general phenomenon whereby charged impurities isoelectronic with the substituted species scatter phonons noticeably more weakly than their corresponding neutral counterparts. This phenomenon deserves further investigation in other systems with thermodynamically stable neutral impurities.

5.7.1 Computational details

We used the VASP [8, 9, 10] DFT code employing the PAW [20, 191] pseudopotentials in the PBE [192, 193] approximation for the phonon calculations. First, the second order force constants (IFC2) are calculated for a relaxed $5 \times 5 \times 5$ (250 atom) supercell with and without a substitution defect, using the small displacement method. Helper code `Phonopy` [1, 2] is used to create the supercells with small displacements, and to read off force constants following DFT calculations. To calculate V_K, we first proceeded by taking the difference between the IFC2s of the pristine and the defective system.

Whereas our procedure is implemented in real space, to reduce the computational workload we consider the local nature of the bond perturbation and we choose two cutoffs, namely r_{cut} and R_{cut}. Here r_{cut} represents the maximum interaction distance between a pair of atoms, where both of them belong to the sphere of radius R_{cut} and centered at the defect site. After convergence tests we have chosen the "pair-" and the "neighbour list-" cutoffs as 0.6 nm and 0.8 nm. Once these values are defined, it is necessary to reinforce the acoustic sum rule: this is done by projecting away the degrees of freedom corresponding to rigid translations [194]. Despite the insulating nature of BAs, we can observe that the character of the state when introducing neutral impurities is metallic. In this case we must use a certain care when evaluating the interatomic forces and force constants: if the VASP smearing parameters were chosen to be as for insulators, this would lead to long range interactions and thus absence of convergence for the phonon-defect scattering rates w.r.t. the cutoffs. In this work we used the default VASP smearing parameters (ISMEAR $= 1$, SIGMA $= 0.2$), comparing with volume-relaxation and spin-relaxation (non-collinear) calculations as well and

finding that the latter do not affect rates and thermal conductivity. A converged value for r_{cut} and R_{cut} was found in all the calculations.

The scattering T-matrix is then calculated using $V = V_K + V_M$ and the Green's function using our home-grown code [195, 184, 196, 194, 197]. Once the T-matrix is known, the phonon-substitution defect scattering rates are calculated for various defect concentrations. To calculate the three-phonon scattering rates, we use the *thirdorder_vasp.py* code [128] in conjunction with *VASP* and *almaBTE* [143]. The calculation of the four-phonon scattering rates is rather expensive and it has been performed with the code developed by prof. Ravichandran [104]. This program is currently set to work only with the *Quantum Espresso* [198] suite. We interpolated these scattering rates on the wave vector mesh used in the current study from a previously published calculation [170]. The phonon-substitution defect scattering rates are combined with the three- and four-phonon, and phonon-isotope scattering rates at the relaxation time approximation level using Matthiesen's rule inside the *almaBTE* code. *AlmaBTE* finds the full solution of the linearised phonon BTE, and outputs the thermal conductivity κ_{ph}. A converged $28 \times 28 \times 28$ transport wave vector mesh is used to solve the phonon BTE, whilst the Green's function is evaluated on a $16 \times 16 \times 16$ grid.

6

Introduction to half-Heusler compounds

In presence of a thermal gradient, some compounds, called "thermoelectrics", can develop a significant electric potential. A closed circuit comprising two thermoelectric materials with different Seebeck coefficients can generate an electric current under a temperature difference between the two junctions [121], and the efficiency of this conversion is directly related to the value of the thermoelectric figures of merit [199]. For a single material, the figure of merit is defined as

$$zT = \frac{S^2 \sigma T}{\kappa}, \tag{6.1}$$

where S is the Seebeck coefficient, σ is the electrical conductivity and $\kappa = \kappa_{\text{el}} + \kappa_{\text{ph}}$ is the thermal conductivity, split into electronic and phononic contribution. The zT factor defines the maximum working efficiency of a thermoelectric device, latter being defined as:

$$\eta = \frac{T_h - T_c}{T_h} \frac{\sqrt{1+ZT}-1}{\sqrt{1+ZT}+T_c/T_h}, \tag{6.2}$$

where T_h and T_c are the hot and cold end of the device respectively. Maximising the zT requires materials with a high power factor $S^2\sigma$ - which can be achieved by searching for compounds with high Seebeck coefficients - and a low thermal conductivity.

The thermoelectric efficiency varies with temperature. Therefore different materials

are suitable for zT optimisation depending on the operating T [200]. For example, in the range between room temperature and 200 °C, Te-B compounds reach zT $\sim$ 1.5, while above 800 °C this value is reached by Si-Ge alloys. Heat sources like industrial waste heat and car exhaust range between 500 and 800 °C. Thus, to convert them into electricity it is better to seek for materials that optimize zT in this range. Thence lead chalcogenides like PbTe and PbSe, skutterudites and half-Heuslers (HHs) are the most promising compounds studied so far. All the mentioned systems reach zT values ranging between 1.1 and 1.5 in the aforementioned temperature range, however lead based materials are known to be either toxic and with poor mechanical strength and skutterudites are characterised by a low stability and presence of rare-earth elements with limited supply which increase the costs.

If we consider the HHs instead, we can find that although reaching an efficiency slightly lower than the previously mentioned materials (zT $\sim$ 1 between 500 and 800 °C for both *n* and *p* type doping) their thermo-mechanical properties are well suited for applications and the impact on the environment is much lower. These factors make them of large interest in the quest of thermoelectric materials for practical applications. The chemical composition of half-Heuslers comprises three elements A, B and X with 1:1:1 stoichiometry. The two atoms A and B are in equivalent positions and form a rocksalt sublattice AB. The element X is in the inequivalent position and forms a zincblend structure AX along with element A [201]. B can either be a transition, a noble or a rare-earth element, X can be a transition or noble metal (*d*-type electronic structure) and A is the main group element (*p*-type configuration). The global structure is of the face-centered-cubic type and the space group is F43m. The hybridization between d-states is generally strong between elements B and X and is responsible for the electronic band gap [202, 203, 204, 200]. Moreover the valence electron count sums up to either 8 or 18, see [205, 206, 207], for those stable HHs compounds with optimal zT factor at intermediate temperatures. The stability ensuing from these elecron counts comes from the unfilled anti-bonding states [208]. The *spd* and atomic decomposed electronic DOS (eDOS) is shown in Figs. 6.1-6.7 for a set of stable $p-$type HHs [208], namely VFeSb, TaFeSb, NbFeSb, TaCoSn, NbCoSn, HfCoSb and ZrCoSb. In particular the d-

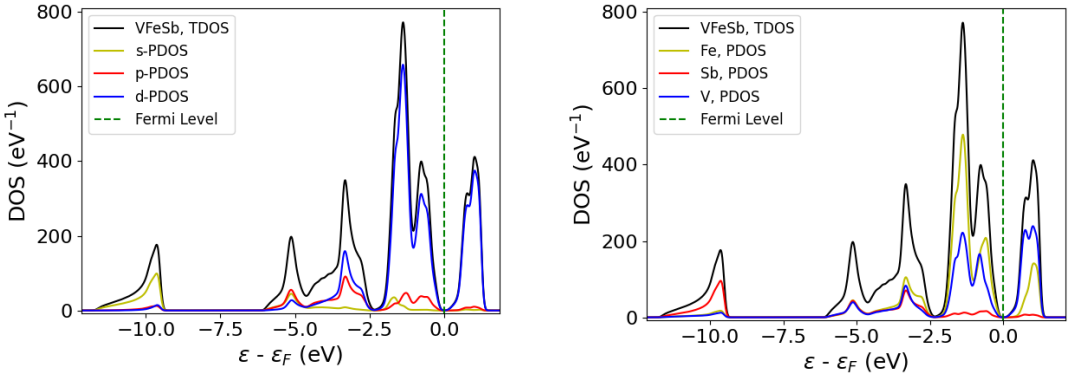

Figure 6.1: Supercell electron density of states for VFeSb. The *spd* orbital (atomic) decomposition is on the left (right) side.

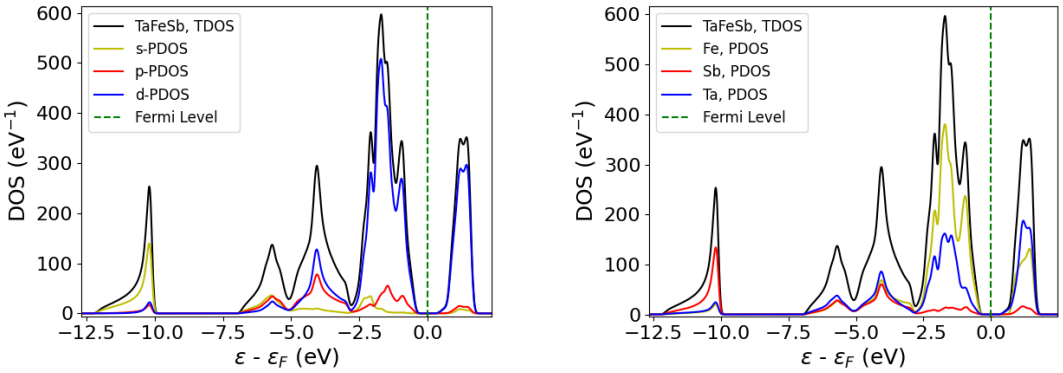

Figure 6.2: Supercell electron density of states for TaFeSb. The *spd* orbital (atomic) decomposition is on the left (right) side.

character of these materials near the Fermi level can be appreciated and it is noticeable that the *p* element of the structure, either Sb or Sn, does give a little contribution to the eDOS while most of the spectral weight near the valence band maximum can be attributed to either cobalt of iron.

Previous experimental [12, 209] and theoretical publications on half-Heusler compounds have mainly focused on the electronic components of the zT formula, with a particular interest in the power factor $S^2\sigma$, the analysis of the correlation between bonding properties and the carriers mobilities [210], and the treatment of the electronic relaxation times [211], which requires going beyond the constant relaxation time ap-

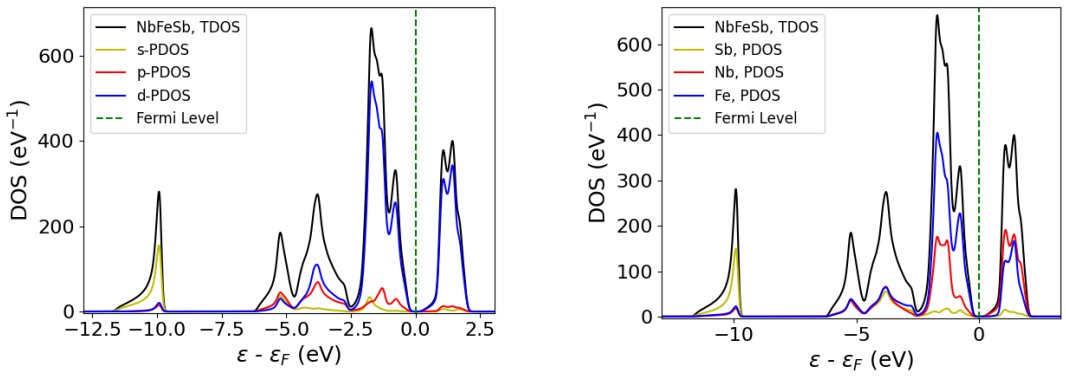

Figure 6.3: Supercell electron density of states for NbFeSb. The *spd* orbital (atomic) decomposition is on the left (right) side.

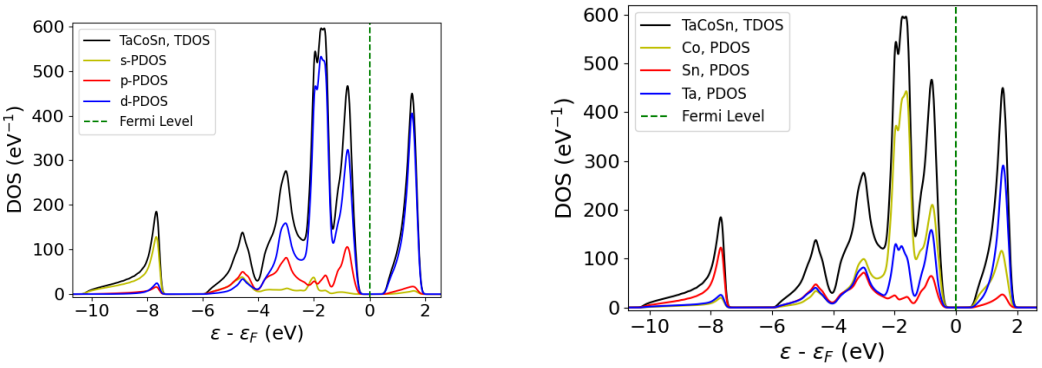

Figure 6.4: Supercell electron density of states for TaCoSn. The *spd* orbital (atomic) decomposition is on the left (right) side.

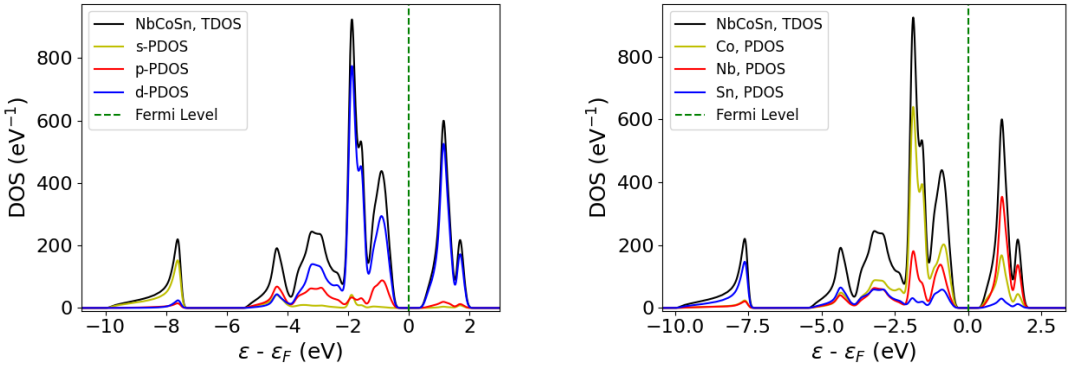

Figure 6.5: Supercell electron density of states for NbCoSn. The *spd* orbital (atomic) decomposition is on the left (right) side.

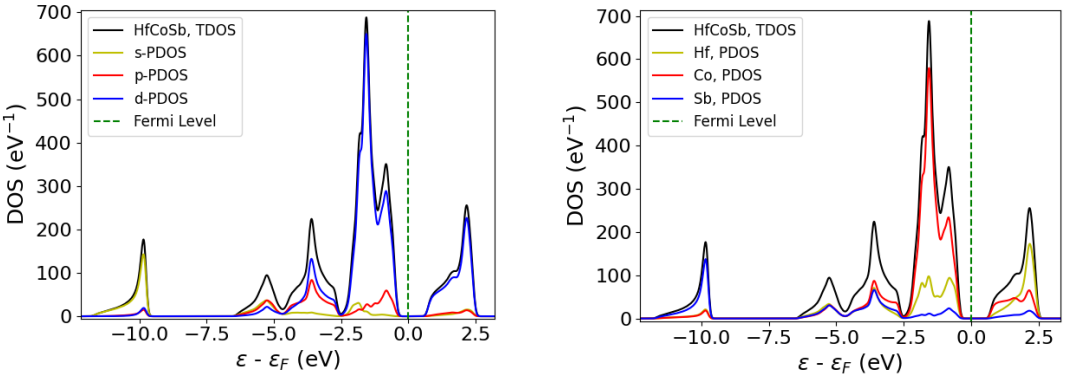

Figure 6.6: Supercell electron density of states for HfCoSb. The *spd* orbital (atomic) decomposition is on the left (right) side.

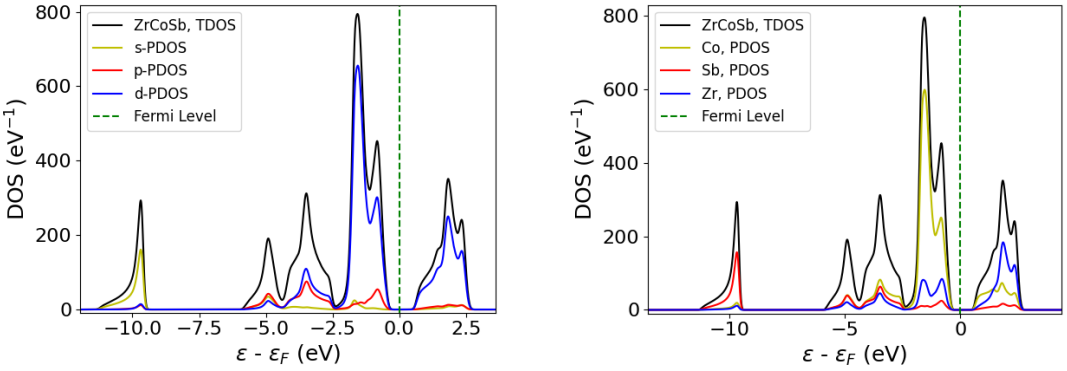

Figure 6.7: Supercell electron density of states for ZrCoSb. The *spd* orbital (atomic) decomposition is on the left (right) side.

proximation often employed in the case of simple metals. In particular Zhou et al. have pointed out that the Seebeck optimisation through electronic band structure engineering - which usually happens for low σ materials - is possible in the case of HHs even though these materials possess a non-small electrical conductivity, and they proved that symmetry-protected interactions between orbitals are likely to be responsible for this. Specifically the electron-acoustic phonon coupling is largely reduced because of the presence of electronic states with strong non-bonding character which decrease the acoustic deformation potential. These states stem from atomic orbitals belonging to different symmetry group representations and thus are forbidden to interact.

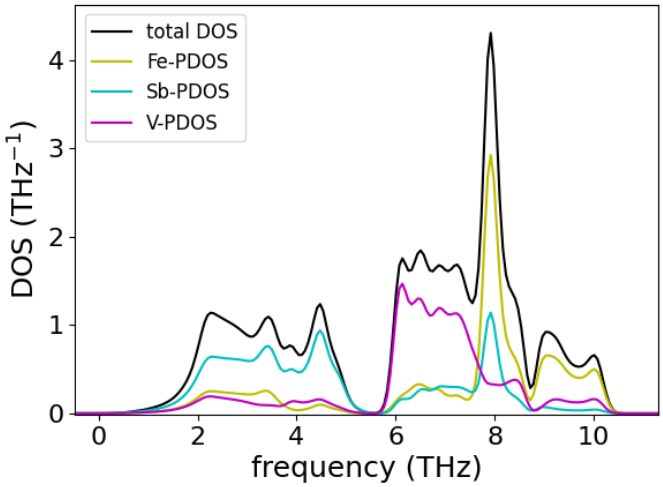

Figure 6.8: Phonon density of states, VFeSb case.

To extract κ_{el} the Wiedemann-Franz law is usually employed. However the effect of phonons on heat transport is generally less known, with the calculation of their contribution to the thermal conductivity often relegated to simple or semi-empirical models, partially due to the computationally demanding task of finding accurate relaxation times for charge and heat carriers. Since a low thermal conductivity is required to maximise the thermoelectric ZT factor, it is of paramount importance to be able to reduce κ_{ph} along with maximising the electronic power factor σS^2. This optimization can be achieved by nanostructuring and/or doping. Concerning the lattice conductivity, a computational screening of compounds with optimal phonon trasport properties has been made by [206], who employed machine-learning based techniques (random forests) to find and study a set of 75 mechanically and thermodynamically stable HHs from the AFLOWLIB.org database [212]. A set of descriptors - including atomistic, structural, electronic and thermodynamic properties - was employed to study the thermal properties of these compounds. An inverse correlation between conductivity and average Pauli electronegativity and atomic radii of the atoms in equivalent positions has been found. Also, κ_{ph} is positively correlated with the Pettifor scale [213].

In Figs. 8-14 we present the phonon total and atomic projected density of states for the aforementioned set of half-Heuslers. As a general rule we realise that the spectral

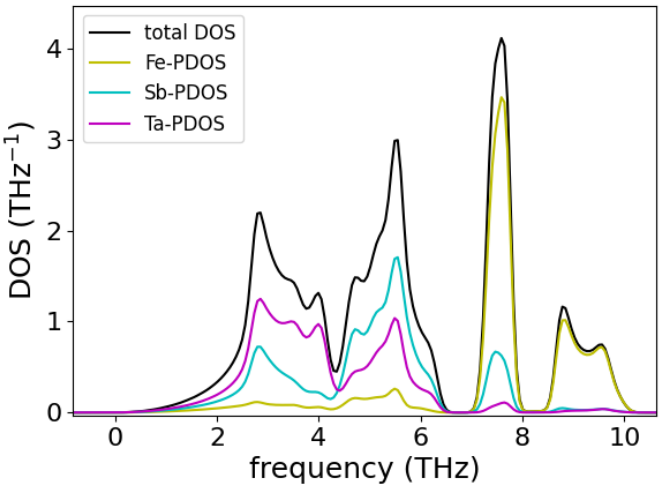

Figure 6.9: Phonon density of States, TaFeSb case.

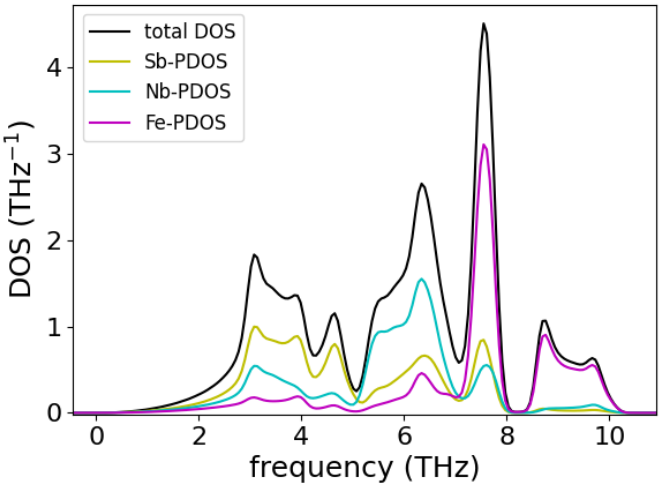

Figure 6.10: Phonon density of states, NbFeSb case.

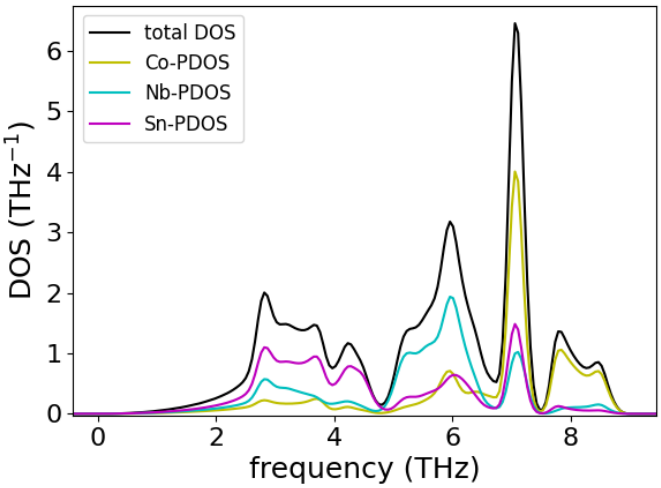

Figure 6.11: Phonon density of states, NbCoSn case.

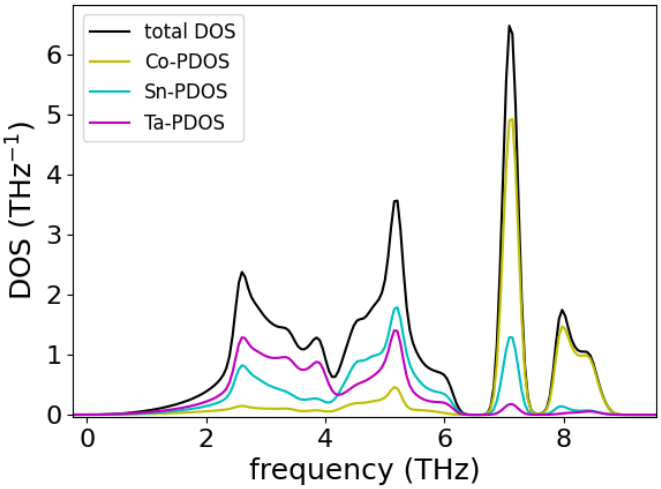

Figure 6.12: Phonon density of states, TaCoSn case.

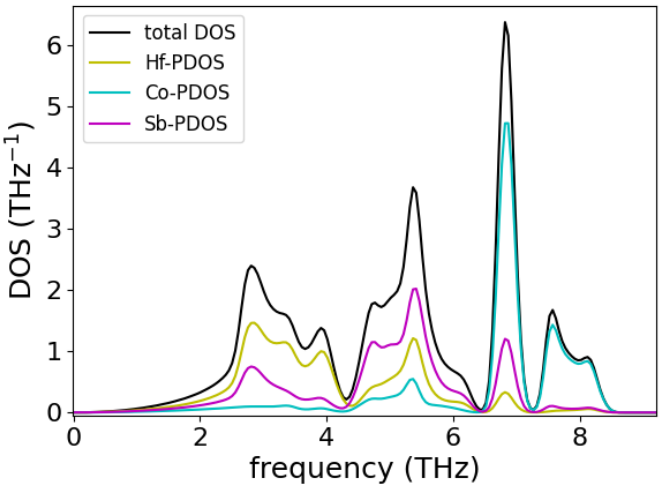

Figure 6.13: Phonon density of states, HfCoSb case.

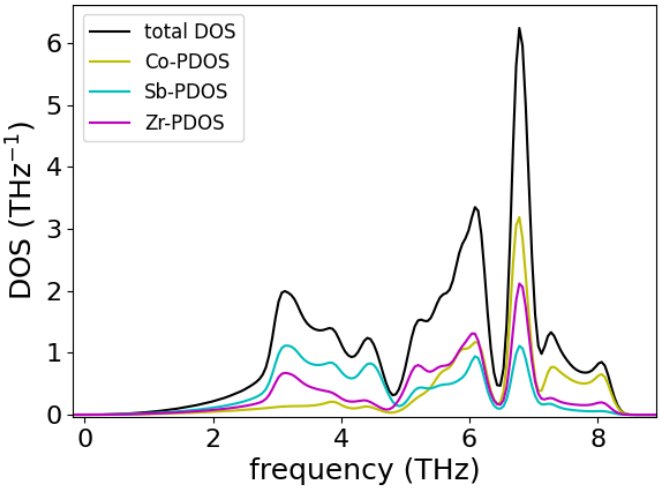

Figure 6.14: Phonon density of states, ZrCoSb case.

weights of cobalt and iron is generally weak at low frequencies and present a peak in the optical range. This fact is due to the smaller masses of Co and Fe w.r.t. the other atoms in the HHs unit cell.

The lattice contribution to the thermal conductivity in a crystal with cubic symmetry reads:

$$\kappa_{\text{ph}} = \frac{k_B}{\Omega_s} \sum_{\lambda} \left(\frac{\hbar \omega_\lambda}{k_B T} \right)^2 n_\lambda^0 (n_\lambda^0 + 1) v_\lambda F_\lambda \,, \tag{6.3}$$

where λ represents the wavevector and branch ($\vec{q}$,b), ω_λ and v_λ are the phonon frequency and group velocity respectively and n_λ^0 is the equilibrium Bose Einstein distribution. The quantity $F_\lambda \equiv \tau_\lambda (v_\lambda + \Delta_\lambda [F_\lambda])$ represents an effective mean free path that includes a coupling between phonon states [178], with τ_λ being the phonon relaxation time and Δ_λ a functional of F_λ itself. In case Umklapp processes dominate the scattering, we can neglect the coupling between modes and work under the single mode relaxation time approximation (SMRTA) by taking $\Delta_\lambda \equiv 0$ as explained in subsection 3.2.6 of chapter 3. The relaxation time can be computed by inverting the total scattering rate for a phonon mode, which in turn can be computed by applying Matthiessen's rule to the main scattering processes. Here we consider anharmonic three-phonon and two-phonon interactions, where the latter comprise both the contribution from isotopes of the elements of the pristine compounds and from substitutional impurities. Therefore we have:

$$\frac{1}{\tau_\lambda} = \frac{1}{\tau_\lambda^{\text{3ph}}} + \frac{1}{\tau_\lambda^{\text{iso}}} + \frac{1}{\tau_\lambda^{\text{def}}} . \tag{6.4}$$

The importance of the phonon-defect scattering for substitutional impurities can be expected to be due to two different main mechanisms, namely the strength of the perturbation induced by the dopant and the spectral weight of the replaced atom. We will see these effects in action in the next chapter.

7

Substitutional impurities in half-Heusler compounds

[1] Half-Heusler semiconductors have been studied throughout the years as promising thermoelectric materials but relatively little work has been done to understand how the introduced impurities would affect the lattice part of the thermal conductivity. Past works on doped and alloyed half-Heusler compounds [12, 209], used simplified phonon-defect scattering models for the computation of κ_{ph}. Several of these works considered only the mass difference between host and substituted atoms [215] as source of phonon scattering, others included the defect-induced change in the local chemistry at the empirical model level [216, 217, 218], or did not consider at all the role played by impurities [210]. Therefore, a proper understanding of how dopants affect κ_{ph} in these materials - considering the perturbation induced by changes in bonds and force constants - is still lacking.

A first step to optimise thermoelectric properties is to identify the most suitable materials. A recent high-throughput study identified a stable set of charged dopants that allow for p-dopability in several promising half-Heusler compounds [208]. Here we use theoretical methods to study the effects of this set of defects in their charged states on the lattice thermal conductivities of VFeSb, TaFeSb, NbFeSb, TaCoSn, NbCoSn, ZrCoSb and HfCoSb. Although it is generally assumed that the amount of κ_{ph} reduction is correlated with the normalized mass difference between host and defect atoms, we show that this is not generally true when the substituted atom is a transition metal.

[1] The content of the present chapter is also available in ref. [214].

Instead, we identify a strong effect due to the local bond perturbation induced by dopants. This effect must be taken into account in order to get an accurate description of phonon thermal transport as a function of the impurity concentration. We explain how bonds are affected by impurities in terms of the electronic structure of the pristine compounds. We also compare our results with recent measurements and finally we present an empirical model of the lattice thermal conductivity as a function of temperature and concentration for the considered set of defects and containing the overall effects of change of mass and bonds.

7.1 Classification of the compounds and the considered substitutions

Here we consider compounds with electron count = 18. Possible ways of constructing these compounds are sketched in fig. 7.1. The half-Heusler structure comprises three species in the 1:1:1 stoichiometry. The two geometrically equivalent sites are labelled as A and A', and the inequivalent one is labeled as B. Following ref. [208], we consider compounds involving periodic table columns 8 or 9 for the B site, 4 or 5 for the A site, and IV or V for the A' site. Species on sites A and B are transition metals, but the one on A' is not. Thus we can define three groups of compounds, in terms of the columns involved: 4-9-V, 5-9-IV, and 5-8-V.

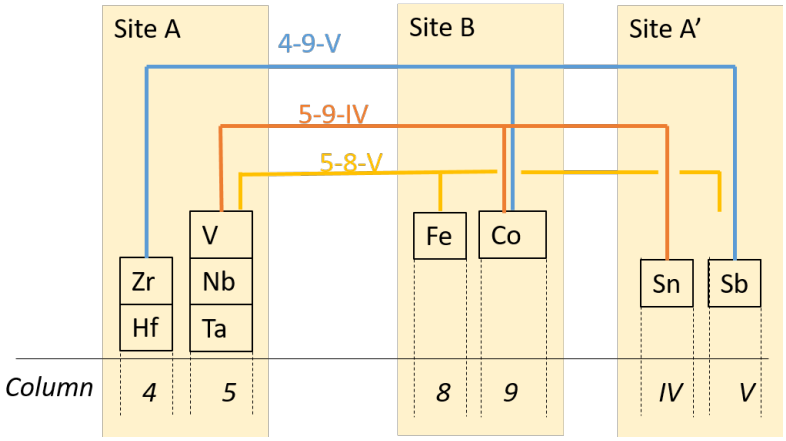

Figure 7.1: Ways of combining the species to construct the 18 electron count compounds considered.

Substitution scheme	Cases
3_4-9-V	$Sc_{(Zr,Hf)}$-Co-Sb
4_5 – 9-IV 8-V	$(Ti,Zr,Hf)_{(V,\ Nb,\ Ta)}$ – Fe-Sb Co-Sn
5-7_8-V	(Nb, Ta)-Mn_{Fe}-Sb
4-9 5-8 – IV_V	(Zr, Hf)-Co (V, Nb, Ta)-Fe – Sn_{Sb}

Table 7.1: Stable substitution schemes considered.

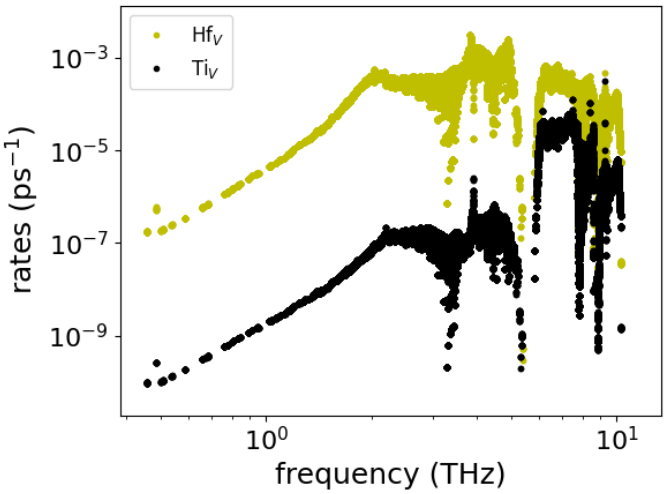

Figure 7.2: V_M perturbation scattering rates at $\chi = 10^{18}$ cm^{-3} for VFeSb.

For each of these groups, p-doping substitutions can in principle be carried out on either of the sites, replacing a species by another one from the column on its left hand side. The possibilities that yielded stable substitutions in ref. [208] are shown in table 7.1.

7.2 Phonon-defect scattering

In figs. 7.12-7.6 we report the mass perturbation induced scattering rates for each impurity in the set with a concentration of 10^{18} cm^{-3}. The observed behaviour can be straightforwardly explained in terms of $\Delta M/M_0$, see table 7.2. In the case of VFeSb,

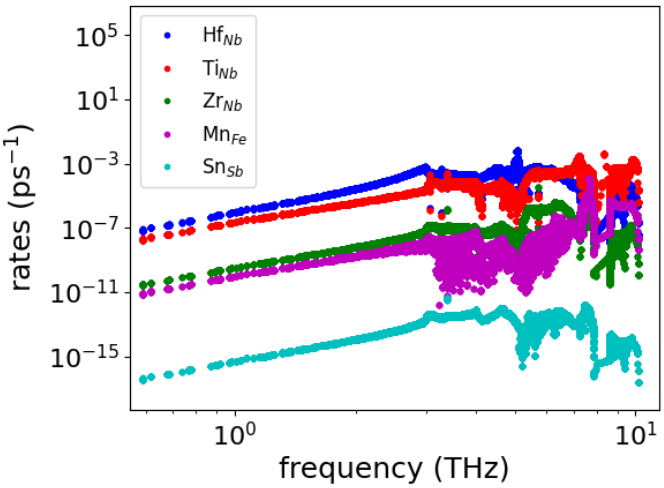

Figure 7.3: V_M perturbation scattering rates at $\chi = 10^{18}$ cm^{-3} for NbFeSb.

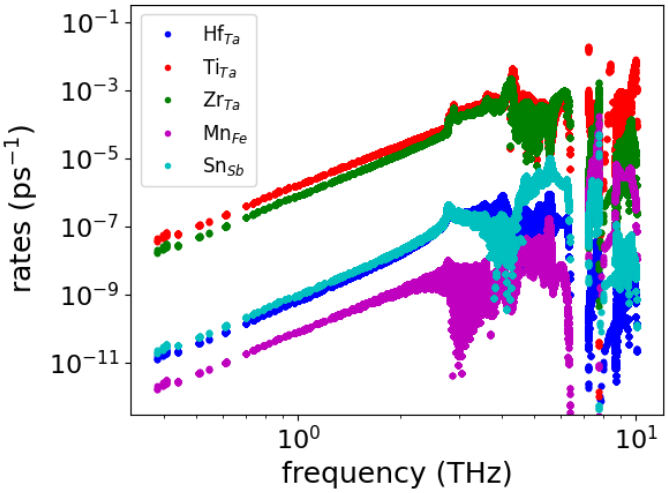

Figure 7.4: V_M perturbation scattering rates at $\chi = 10^{18}$ cm^{-3} for TaFeSb.

	Ti_V^{-1}	Ti_{Nb}^{-1}	Ti_{Ta}^{-1}	Hf_V^{-1}	Hf_{Nb}^{-1}	Hf_{Ta}^{-1}	Zr_{Nb}^{-1}	Zr_{Ta}^{-1}	Sc_{Hf}^{-1}	Sc_{Zr}^{-1}	Sn_{Sb}^{-1}	Mn_{Fe}^{-1}
$\frac{\Delta M}{M_0}$	0.06	0.48	0.74	2.50	0.92	0.01	0.02	0.496	0.75	0.50	0.025	0.016

Table 7.2: Absolute mass difference normalized by the host atom mass for each substitution impurity.

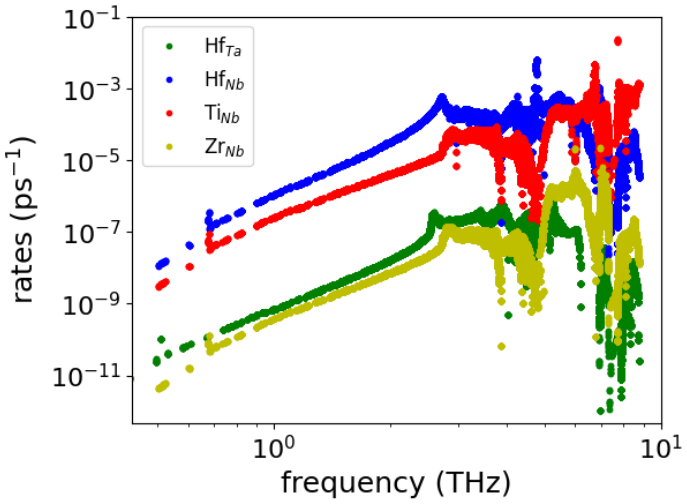

Figure 7.5: V_M perturbation scattering rates at $\chi = 10^{18}$ cm^{-3} for TaCoSn and NbCoSn.

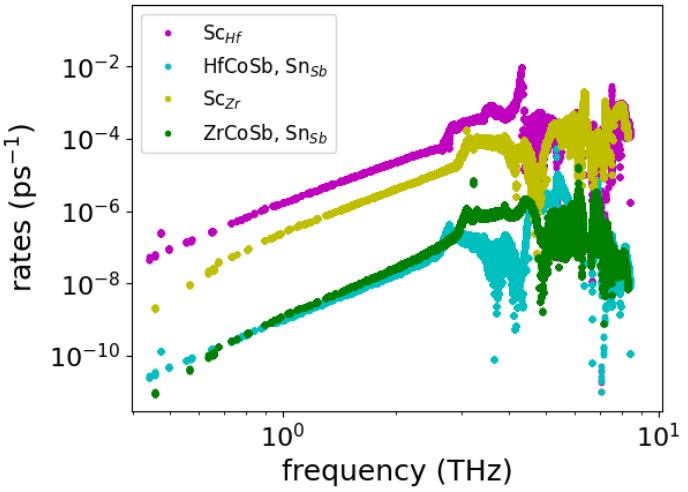

Figure 7.6: V_M perturbation scattering rates at $\chi = 10^{18}$ cm^{-3} for HfCoSb and ZrCoSb.

we note a stark contrast between the effect produced by the hafnium substitution with respect to titanium. Similarly, in figs. 7.3 and 7.4 the rates span several order of magnitude, ranging from $\sim 10^{-15}$ - 10^{-11} ps^{-1} for Sn and Mn dopants to $\sim 10^{-3}$ps^{-1} for Hf and Ti. Similar orders of magnitude are seen for the TaCoSn and NbCoSn dopants, see fig. 7.5, with the Zr and Hf$_{\text{Ta}}$ dopants producing little phonon scattering due to the small (normalised) mass difference. Finally, for ZrCoSb and HfCoSb the weak rates produced by Sn are contrasted by the much larger effect induced by scandium. For the whole set of defects, the rates span the range of magnitude $\sim 10^{-15}$ - 10^{-3} ps^{-1}, namely from the tin dopant in NbFeSb to the Hf substitution in VFeSb. This analysis does not include the effect of V_K, that is the change of bonds and the lattice relaxation around the impurity site induced by point defects. To better assess the importance of the bond perturbation and the magnitude of the scattering rates for each dopant and material we can use a descriptor defined as follows (in analogy with what we have done for the V_K-induced effect in BAs, see eq. 5.1):

$$D_{\text{def};V} \equiv \frac{1}{N}\sum_{\lambda} \tau^{-1}_{\lambda;V}, \tag{7.1}$$

where N is the number of $\vec{q}$ - points in the reciprocal space grid, $\tau_{\lambda;V}$ is the relaxation time computed with either the bond V_K, mass V_M or total $V = V_M + V_K$ perturbation. This descriptor aims at giving a scalar and temperature-independent representation of the magnitude of the scattering mechanisms for each of the considered dopants and materials. In tab. 5.1 we show the value of normalised mass variance for each defect and material.

The values of this descriptor in the case of VFeSb are reported in fig. 7.7. The mass perturbation from the two considered impurities clearly follows the mass variances trend, with a much stronger contribution from the Hf$_V^{-1}$ substitution. We note that most of the defect-induced perturbation is attributable to a change in the local bonds in the case of the Ti$_{\text{V}}^{-1}$ impurity where the mass part of the perturbation is negligibly small. The contribution from V_K is particularly relevant for the Hf$_{\text{V}}^{-1}$ defect, although in this case the effect coming from the force constants difference is present along with

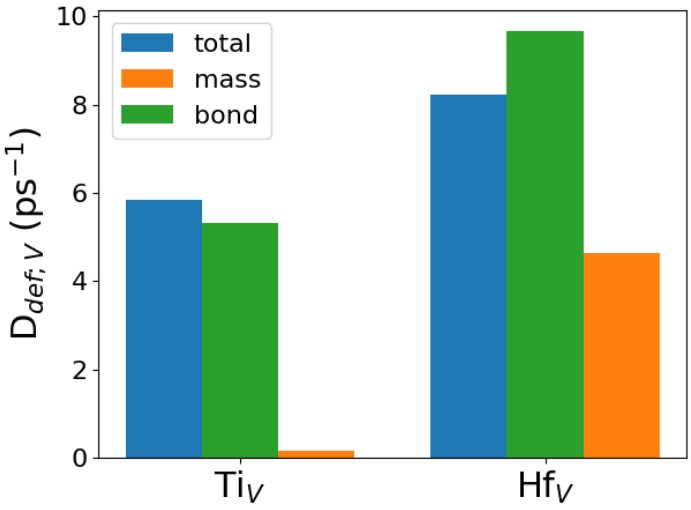

Figure 7.7: Descriptor for VFeSb dopants. The blue, orange and green columns indicate respectively the total, mass only and bond only induced-scattering rates.

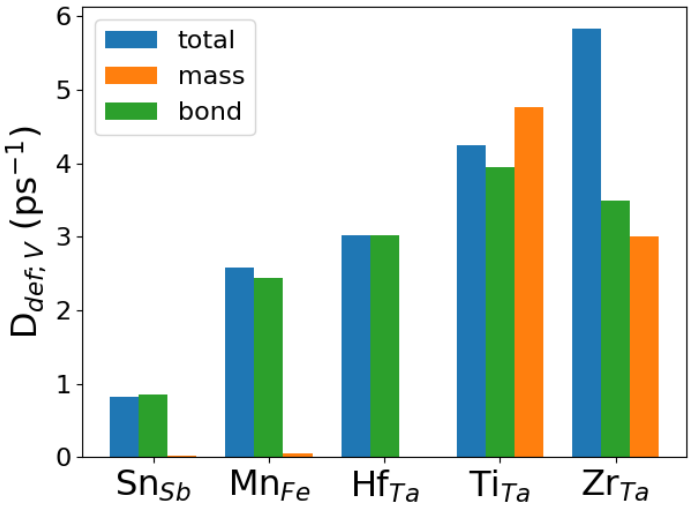

Figure 7.8: Descriptor for TaFeSb dopants. The blue, orange and green columns indicate respectively the total, mass only and bond only induced-scattering rates.

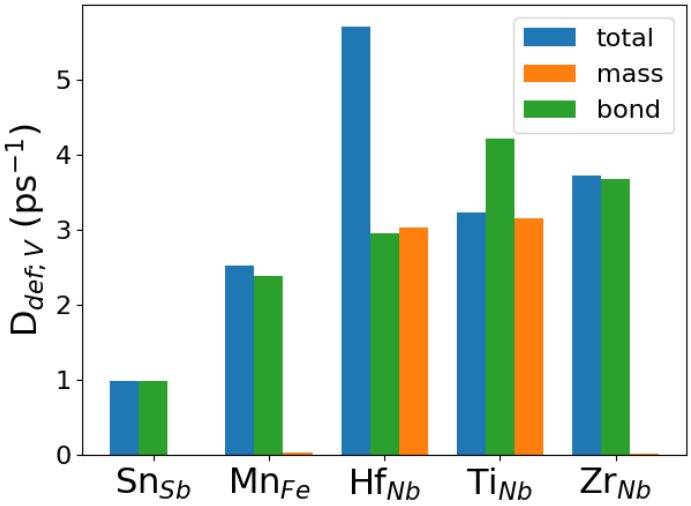

Figure 7.9: Descriptor for NbFeSb dopants. The blue, orange and green columns indicate respectively the total, mass only and bond only induced-scattering rates.

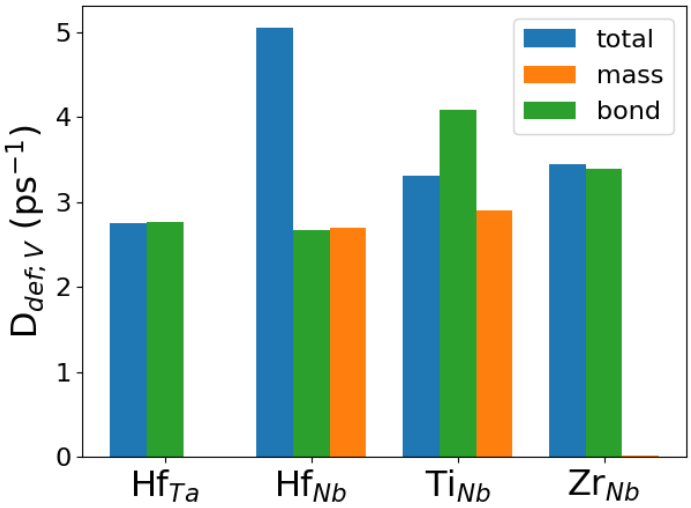

Figure 7.10: Descriptor for TaCoSn and NbCoSn dopants. The blue, orange and green columns indicate respectively the total, mass only and bond only induced-scattering rates.

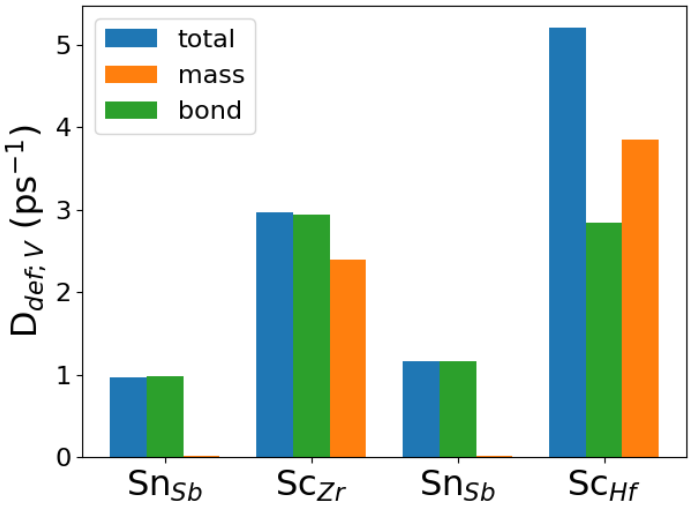

Figure 7.11: Descriptor for ZrCoSb and HfCoSb dopants. The blue, orange and green columns indicate respectively the total, mass only and bond only induced-scattering rates.

a much larger mass substitution that for Ti. We also recognise that $D_{\text{def};V} < D_{\text{def};V_K}$ in the case of the hafnium substitution.

In figures 7.8 and 7.9 we show the values of the descriptor for the dopants of TaFeSb and NbFeSb respectively. The mass perturbation is negligibly small in the $\text{Sn}_{\text{Sb}}^{-1}$, $\text{Mn}_{\text{Fe}}^{-1}$ and $\text{Hf}_{\text{Ta}}^{-1}$ ($\text{Zr}_{\text{Nb}}^{-1}$) cases, following the periodic table. If we evaluate the effect from V_K we can also see that phonons are still weakly scattered by the $\text{Sn}_{\text{Sb}}^{-1}$ substitution. The phonon-defect interaction is visibly much stronger when the dopants are Ti and Zr or even Hf and Mn. Combined with a large mass perturbation, the strongest scattering comes from $\text{Ti}_{\text{Ta}}^{-1}$ and $\text{Zr}_{\text{Ta}}^{-1}$ for TaFeSb and $\text{Hf}_{\text{Nb}}^{-1}$ and $\text{Ti}_{\text{Nb}}^{-1}$ for NbFeSb. A similar phenomenon is found in the cases of NbCoSn and TaCoSn dopants in fig. 7.10 with the $\text{Hf}_{\text{Nb}}^{-1}$ confirmed to give the strongest scattering, this also being due to the large associated V_M. A surprisingly large bond perturbation in the $\text{Ti}_{\text{Nb}}^{-1}$ and $\text{Zr}_{\text{Nb}}^{-1}$ substitution cases is also observed. We would also like to note, in both NbFeSb and NbCoSn, that the mass descriptor for the Ti_{Nb} impurity is larger than for Hf_{Nb}, despite Hf being much heavier than Ti. This can be attributed to the larger rates induced by Ti at medium-high frequencies, see figs. 7.3 and 7.5. We finally point out that, in both TaFeSb, NbFeSb and

NbCoSn, doping with titanium leads to an overall phonon scattering from impurities lower than what we could obtain by adding up the separate contributions from the mass and force constants perturbations alone, similarly to what we have previously observed in VFeSb (Hf substitution). We will explore this phenomenon in the next sections. If we now evaluate the last compound of each set, i.e. HfCoSb and ZrCoSb, we find in both cases that doping with Sn produces a rather small scattering, either of mass or bond origin, while the strongest impact is due to Sc substitution which leads to both a strong V_M and V_K terms.

Thus, as a general trend, we find that the Sn_{Sb}^{-1} substitution is responsible for a very weak phonon-defect interaction, while stronger effects can be expected for the remaining dopants. In particular, the Hf_{Nb}^{-1} and Sc_{Hf}^{-1} impurities are the sources for the strongest scattering effects among all the dopants in the set, by virtue of a combined effect of both large mass variance and strong bond perturbation. Of particular interest are the substitutions involving transition metals, specifically in the Zr_{Nb}^{-1}, Hf_{Ta}^{-1} and Ti_{V}^{-1} cases. It is common to assume that both mass and bond-induced perturbations are small for substitutional defects when the impurity and host atoms are adjacent in the periodic table. This is what happens in the Sn substitution case, but not when transition metal elements are considered, except for Mn.

We can give a simple qualitative explanation for the observed trend in terms of the electronic structure of the parent compounds. As mentioned in chapter 6, half-Heuslers have a strong d-orbital character near the electronic band gap, as a consequence of containing block-d elements. On the other hand the p-contribution to the density of states, coming mostly from elements like Sn and Sb, is much smaller close to the gap [202, 203, 204, 200].This has been confirmed by our eDOS calculations, see figs. 6.1-6.7. Therefore, the substitution of Sb is expected to affect the electronic properties, and thus forces and IFCs, much less than the substitution of a transition metal element. We also note that despite possessing a strong electronic DOS contribution, the replacement of Fe with Mn is among the weakest bond scatterers. Unlike the other cases, the Mn substitution takes place on the B-site. Thus one cannot fairly compare its effect with that of the other transition metal substitutions. The small scattering rates of the Mn_{Fe}^{-1} case

	VFeSb	NbFeSb	NbCoSn	TaFeSb	TaCoSn	HfCoSb	ZrCoSb
$\kappa_{ph,0}$ ($W \cdot K^{-1} \cdot m^{-1}$)	15.6	22.6	16.3	15.9	16.8	21.8	21.9

Table 7.3: Thermal conductivity of the pristine compounds at 300 K.

may also be partly the result of the small phonon local density of states on the Fe atom in the lower frequency range (see figs. 6.8-6.14). On the other hand, non-iron/cobalt atoms tend to present a bigger local phDOS at middle/low frequencies as results of having larger masses in general, which magnify the importance of the perturbation generated by their substitution.

7.3 Thermal conductivity

The pristine thermal conductivity $\kappa_{ph,0}$ at 300 K is shown in tab. 7.3 for the seven half-Heusler compounds. This section presents the dependence of $\kappa_{ph}/\kappa_{ph,0}$ on the impurity concentration at the temperature of 300 K for all the considered materials and defects. In figures 7.12-7.16 we report the conductivity normalised by its pristine value in the cases of VFeSb, TaFeSb, NbFeSb, TaCoSn, NbCoSn, ZrCoSb and HfCoSb upon doping. All defects are considered in their charged acceptor state, and dashed lines indicate the use of the mass perturbation only, while solid lines correspond to the total perturbation $V = V_K + V_M$ case. The conductivity curves partly reflect the trend observed for the descriptor. In general we find that Sn and Mn do not affect the thermal conductivity by much, lowering it by only a 20% at concentrations $\sim 10^{21}$ cm^{-3}. On the other hand, the conductivity of HfCoSb and ZrCoSb are reduced by as much as 40-50% at the same concentration upon Sc doping. A similarly large reduction is observed in the case of NbCoSn when Nb is substituted by Hf or TaFeSb when Ta is substituted by Ti or Zr. The largest reduction at $\chi \sim 10^{21}$ cm^{-3} is observed for VFeSb and NbFeSb when V or Nb are substituted by Hf, where the conductivity presents a decrease of $\sim 60\%$ of its pristine value. These results can be understood in terms of the large phonon-defect scattering rates shown in figs. 7.7 and 7.9.

The difference between total and mass contributions to the conductivity decrease is

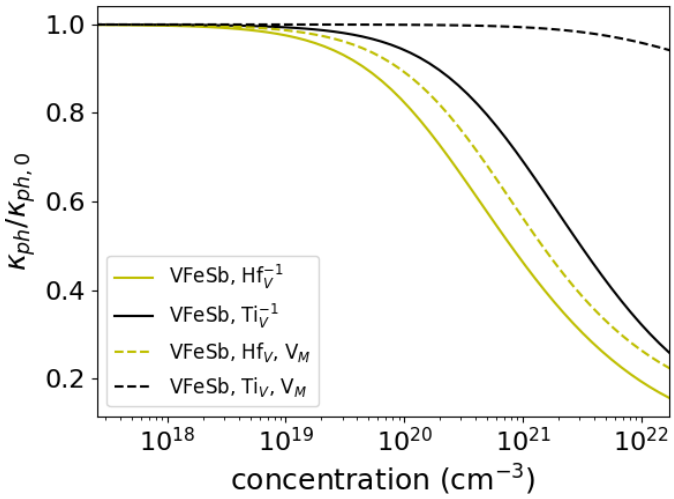

Figure 7.12: Thermal conductivity of VFeSb upon Ti and Hf doping. Continuous (dashed) lines correspond to total (mass only) perturbation.

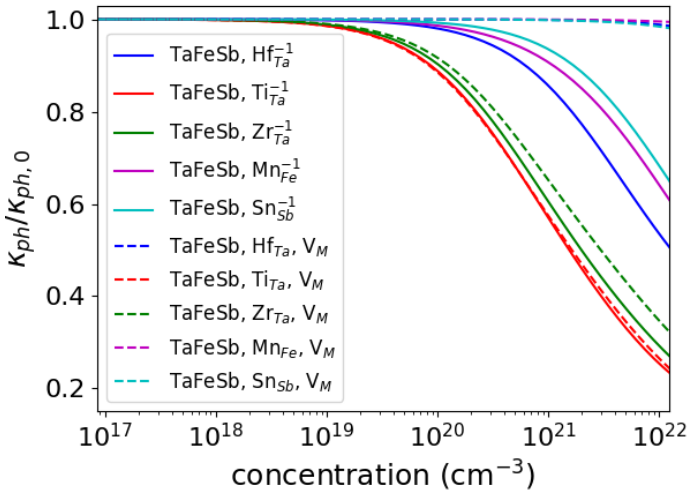

Figure 7.13: Thermal conductivity of TaFeSb upon Ti, Hf, Zr, Mn and Sn doping. Continuous (dashed) lines correspond to total (mass only) perturbation.

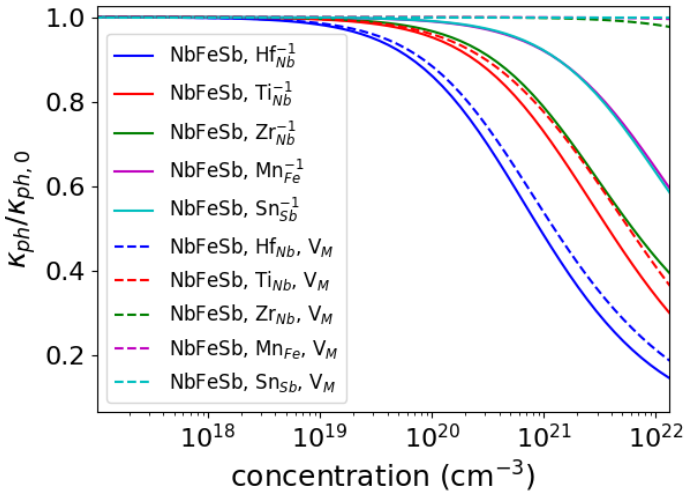

Figure 7.14: Thermal conductivity of NbFeSb upon Ti, Hf, Zr, Mn and Sn doping. Continuous (dashed) lines correspond to total (mass only) perturbation.

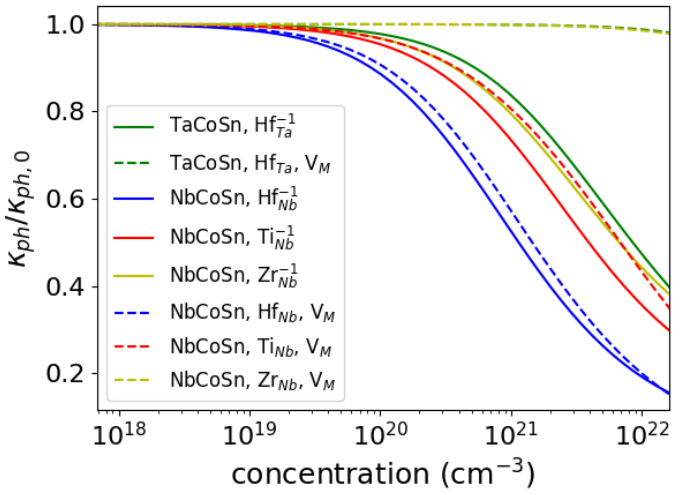

Figure 7.15: Thermal conductivity of TaCoSn and NbCoSn upon Hf, Ti and Zr doping. Continuous (dashed) lines correspond to total (mass only) perturbation.

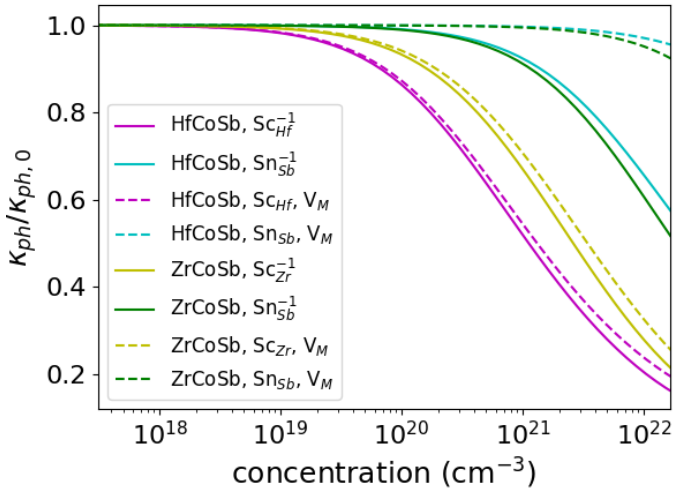

Figure 7.16: Thermal conductivity of HfCoSb and ZrCoSb upon Sc and Sn doping. Continuous (dashed) lines correspond to total (mass only) perturbation.

feeble when V_M is large. This can be seen in the cases of Hf_V^{-1}, Ti_{Ta}^{-1}, Zr_{Ta}^{-1}, Hf_{Nb}^{-1}, Ti_{Nb}^{-1} and Sc substitutionals. On the other hand the effect of V_K is much more noticeable in those transition metals substitutions where the impurity replaces its adjacent atom in the periodic table, namely Ti_V^{-1}, Zr_{Nb}^{-1} and Hf_{Ta}^{-1}.

The value of κ_{ph} is in general correlated with the normalized mass difference between the impurity and the substituted atom, but there are some exceptions. This is noticeable in the Ti_V^{-1}, Zr_{Nb}^{-1} and Hf_{Ta}^{-1} cases, which have a relevant impact on the thermal conductivity of VFeSb, NbFeSb/NbCoSn and TaFeSb/TaCoSn respectively, despite presenting a very weak mass perturbation and having similar atomic radii to the atom they substitute. Furthermore, the correlation with $\Delta M/M_0$ does not exclude the possibility of a correlation with the change in the local chemistry represented by V_K, which is the case of several V, Nb, Ta, Hf and Zr substitutionals, as also seen in figures 7.7-7.11.

7.3.1 Comparison with experimental data

Figure 7.17 compares our calculations for the Sn_{Sb}^{-1} doped ZrCoSb with the thermal conductivity measurements at 300 K reported in ref. [11] for the same material. The point defect perturbation induced by tin overestimates the phonon contribution to

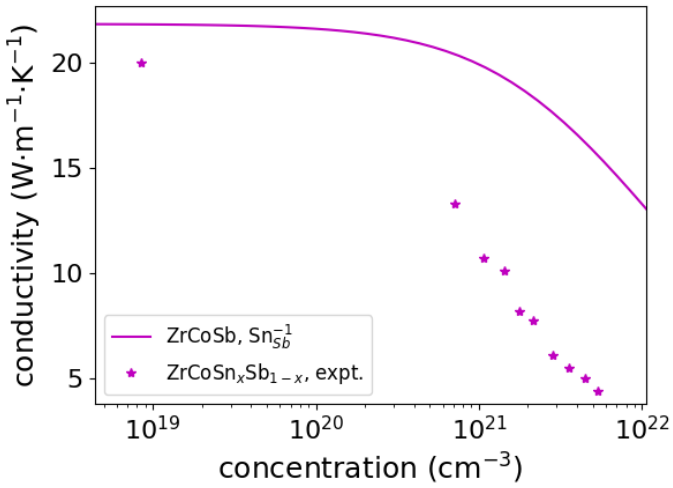

Figure 7.17: Thermal conductivity as a function of the concentration for Sn_{Sb}^{-1} doped ZrCoSb at 300 K. Continuous line: total defect perturbation. Stars: experimental measurements from ref. [11].

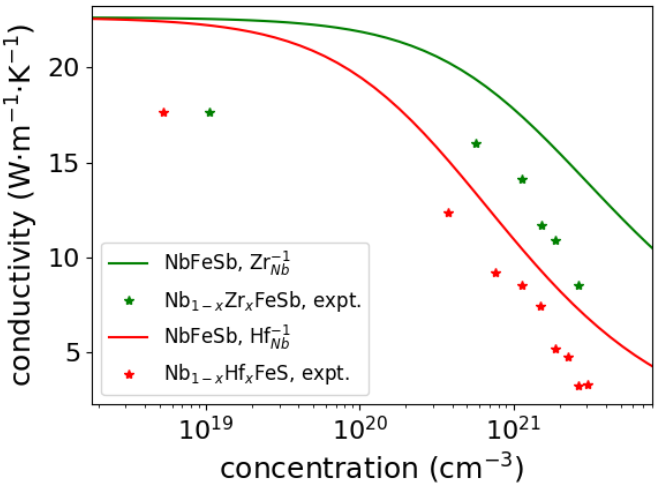

Figure 7.18: Thermal conductivity as a function of the concentration for $(Zr,Hf)_{Nb}^{-1}$ doped NbFeSb at 300 K. Continuous line: total defect perturbation. Stars: experimental measurements from ref. [12].

κ with respect to the experimental results. This is in agreement with the analysis reported in [11], which attributes the strong reduction of the conductivity as induced by Co/4d Frenkel pairs (FP), not included in the present study. Here 4d indicates the 4d($\frac{3}{4}$,$\frac{3}{4}$,$\frac{3}{4}$) Wyckoff position, which site is unoccupied in pristine HHs. With A/4d we mean that an atom of type A (cobalt, in this case) creates a FP by leaving its original location to occupy a neighbouring 4d site. Such large reduction due to Frenkel defects might also happen in other half-Heusler compounds having cobalt/iron at the B site and being doped with Sn, since the migration of Co atoms seems to be bolstered by the presence of tin as result of charge compensation effects that happen upon p-type doping [11]. Similarly, the formation of Fe/4d Frenkel pairs may plummet the conductivity in HHs containing iron at the B site with respect to the effect of the perturbation induced by replacing antimony with tin. In ref. [214] we also mention a different analysis which highlights the possibility that uncorrelated cobalt vacancies and interstitials may form in ZrCoSb (since they are energetically more favoured than Frenkel pairs) and possibly in other half-Heuslers (eventually with Fe replacing Co). Since phonons are considerably scattered by interstitials and vacancies, their inclusion in the calculations of κ_{ph} leads to a good agreement with the experiments in the case of ZrCoSb.

In figure 7.18 we show the calculated room-temperature κ_{ph} for $Nb_{1-x}A_xFeSb$ (A = Ti or Hf) as a function of the concentration of defects (including both the mass and force constants induced perturbations) in comparison with the measurements in ref. [12]. The lower values of the experimental measurement has been suggested to come from additional boundary and electron-phonon scattering contributions [12, 215], not included in the present *ab initio* calculation. On the other hand, we need to stress again that as a result of having orbitals in different symmetry group representations, the electron-acoustic phonon couplings are small in HH compounds [210]. This analysis was also corroborated by ref. [11] which found the scattering from carriers to be negligible. To clarify the role of the phonon-hole interaction from a thermal transport perspective, we have computed from first principles the self-energies (eq. 3.85) corresponding to a weakly- and ultra-doped sample in the case of NbFeSb, for which we have evaluated

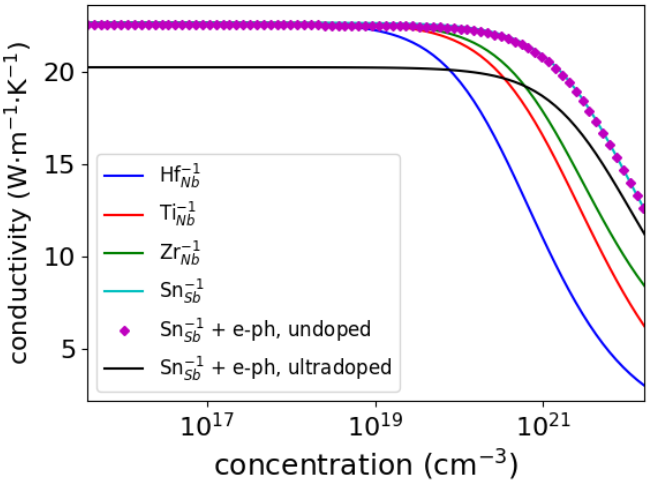

Figure 7.19: Thermal conductivity as a function of the concentration for $(Hf,Ti,Zr)_{Nb}^{-1}$ and Sn_{Sb}^{-1} doped NbFeSb at 300 K. Purple diamond and black curve include the presence of phonon-hole scattering computed through the *EPW* package [13, 14]. For simplicity, for each curve including the phonon-hole interaction a unique value of the Fermi level was considered (in the middle of the gap and at the VBM for the undoped and ultradoped cases respectively).

the lattice thermal conductivity as a function of the doping concentration. The scattering from carriers has been included as well in the tin substitution case, see fig. 7.19. The result confirms that the inclusion of the phonon-hole interaction is insufficient to match the experimental results, since it leads to a much poorer decrease of κ_{ph} with respect to the Hf, Zr and Ti dopants. This prompts the consideration of other factors to explain the strong reduction of the conductivity upon Hf and Zr doping, like the aforementioned Fe/4d Frenkel pairs or the presence of uncorrelated iron vacancies and interstitials.

7.3.2 Matthiessen's rule and interference effects

By inspecting figs. 7.7, 7.8 and 7.10 for hafnium-doped VFeSb and titanium-doped TaFeSb, NbFeSb and NbCoSn we realised that - in certain cases - the total scattering of phonons by impurities does not correspond to the sum of the V_M-only and V_K-only rates. With this purpose, it is worth stressing that $T^+[V] \neq T^+[V_M] + T^+[V_K]$, i.e.

the Mathiessen's rule does not apply to the mass and force constants perturbations induced by the defects. To assess the deviation of the true scattering rates eq. 3.80 from a Mathiessen-like formulation we ought to compute

$$\left(\frac{1}{\tau_{\lambda}^{\text{ph-def}}}\right)_{V_M} = -\chi \frac{V_{\text{uc}}}{\omega_{\lambda}} \operatorname{Im} \langle \lambda | T^{+}[V_M] | \lambda \rangle , \tag{7.2}$$

$$\left(\frac{1}{\tau_{\lambda}^{\text{ph-def}}}\right)_{V_K} = -\chi \frac{V_{\text{uc}}}{\omega_{\lambda}} \operatorname{Im} \langle \lambda | T^{+}[V_K] | \lambda \rangle \tag{7.3}$$

and

$$\tilde{\tau}^{-1}_{\lambda;\text{ph-def}} \equiv \tau^{-1}_{\lambda;\text{ph-def}}[V_M] + \tau^{-1}_{\lambda;\text{ph-def}}[V_K]. \tag{7.4}$$

Since at the second-order the T-matrix can be written as $V + VG_0^+V$ and $\tau^{-1}_{\lambda;\text{ph-def}}$ as $-\chi V_{uc} \sum_{\lambda'} |\langle \lambda | V | \lambda' \rangle|^2 \delta(\omega_{\lambda}^2 - \omega_{\lambda'}^2)$, with

$$|\langle \lambda | V | \lambda \rangle|^2 \equiv |V_{\lambda,\lambda'}|^2 = |V_{M;\lambda,\lambda'}|^2 + |V_{K;\lambda,\lambda'}|^2 + 2\,\text{Re}\Big\{ V^*_{M;\lambda,\lambda} V_{K;\lambda,\lambda} \Big\}, \tag{7.5}$$

this prompts us to identify the deviations from the Mathiessen's rule as due to interference effects between mass and bond induced perturbations. In figures 7.20-7.24 we show - for all the HHs and corresponding dopants - the phonon-defect scattering descriptor $D_{\text{def};V} \equiv \frac{1}{N}\sum_{\lambda} \tau^{-1}_{\lambda;V}$ along with $\tilde{D}_{\text{def}} \equiv D_{\text{def};V_M} + D_{\text{def};V_K}$ - representing the Matthiessen's rule - which excludes interference effects between mass and force constants perturbations. We can notice strong differences between D and $\tilde{D}$ for the following substitution $\text{Hf}_{\text{V}}^{-1}$, $\text{Ti}_{\text{Ta}}^{-1}$, $\text{Ti}_{\text{Nb}}^{-1}$ (in both NbFeSb and NbCoSn), $\text{Sc}_{\text{Zr}}^{-1}$ and $\text{Sc}_{\text{Hf}}^{-1}$. In all the previous cases we have $D < \tilde{D}$, a sign that the interference terms tend to partially cancel out the effect produced by V_M and V_K alone.

Given the presence of destructive interference between the contributions from V_M and V_K to the scattering rates descriptor in several impurities among those that scatter

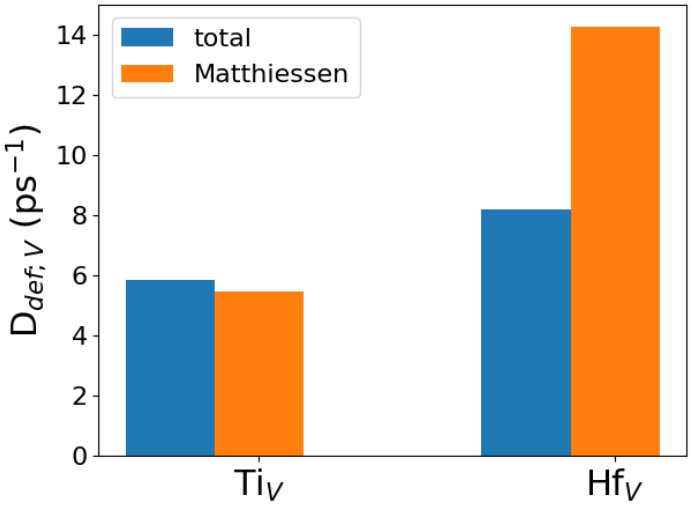

Figure 7.20: Phonon-defect scattering rates descriptor for VFeSb dopants. The blue (orange) columns are for a model that includes (neglects) the mass-force constants interference effects.

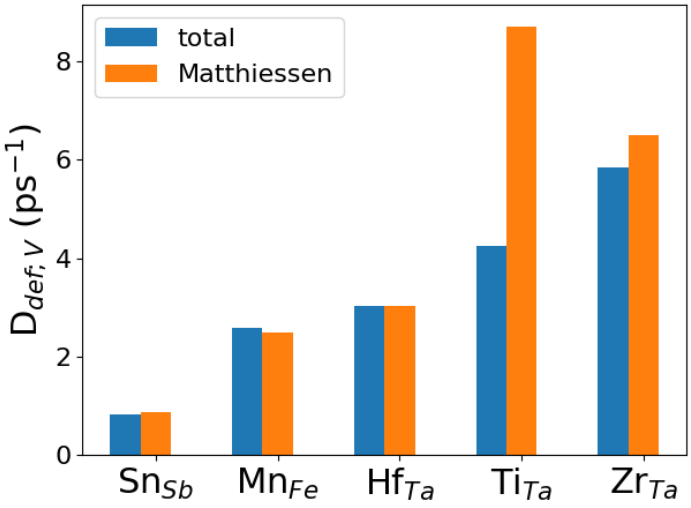

Figure 7.21: Phonon-defect scattering rates descriptor for TaFeSb dopants. The blue (orange) columns are for a model that includes (neglects) the mass-force constants interference effects.

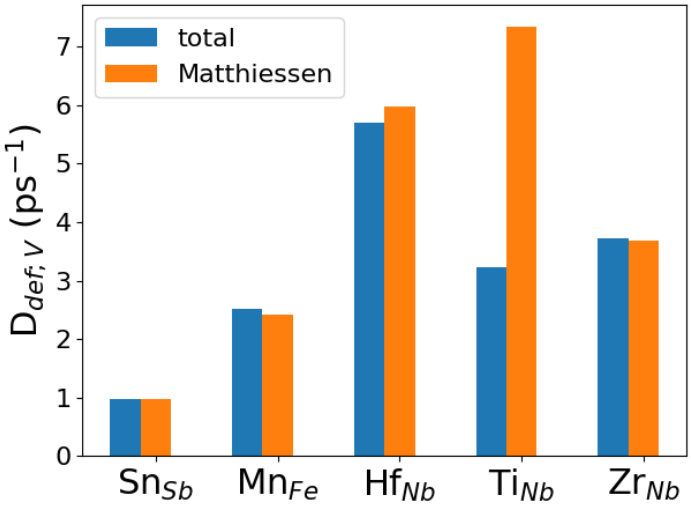

Figure 7.22: Phonon-defect scattering rates descriptor for NbFeSb dopants. The blue (orange) columns are for a model that includes (neglects) the mass-force constants interference effects.

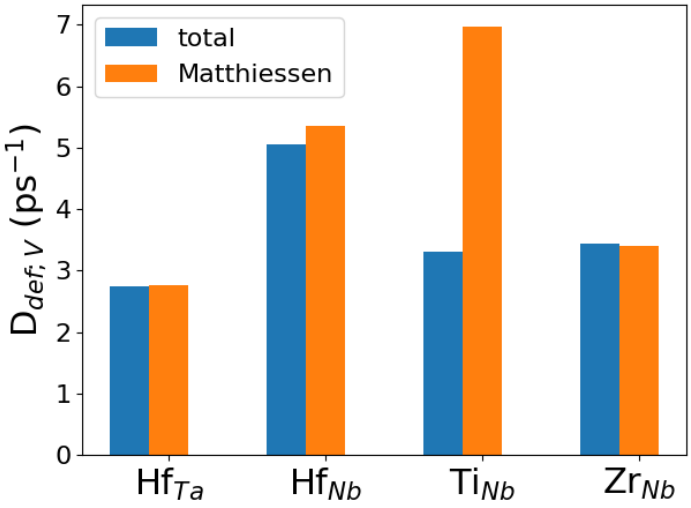

Figure 7.23: Phonon-defect scattering rates descriptor for NbCoSn and TaCoSn dopants. The blue (orange) columns are for a model that includes (neglects) the mass-force constants interference effects.

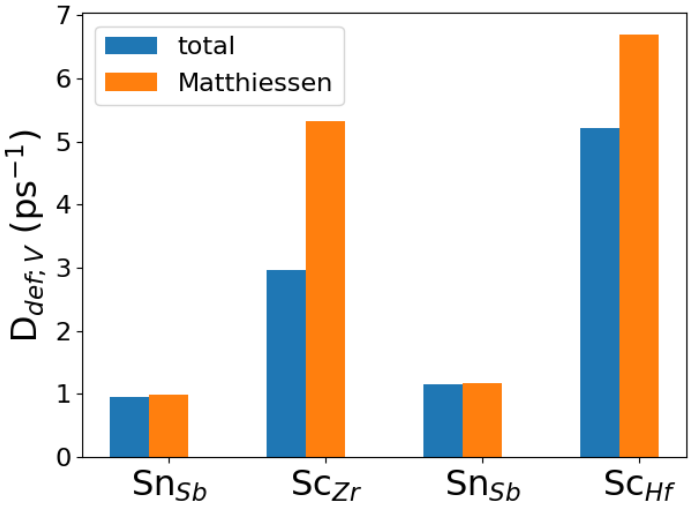

Figure 7.24: Phonon-defect scattering rates descriptor for ZrCoSb and HfCoSb dopants. The blue (orange) columns are for a model that includes (neglects) the mass-force constants interference effects.

phonon the most, it is instructive to see how the previous thermal conductivity results differ from a model that (incorrectly) neglects the interference term between bond and mass perturbations. In fig. 7.25 we notice that decoupling the mass and bond contributions to the phonon-impurity rates can lower κ_{ph} a 10% more than the correct formulation of $\tau^{-1}_{\lambda,\text{ph-def}}$. The effect of this overestimation is particularly visible when the dopant is titanium.

7.3.3 Empirical model for κ_{ph}

It is possible to analytically approximate the thermal conductivity as a function of temperature and doping concentration, including not only the mass perturbation but also the influence of dopants on the local bonds. To do so, we customise an empirical version of the model developed by Klemens [183]. This model assumes a linear phonon dispersion, high temperature limit and analytical expressions for Umklapp and defect induced scattering rates, thus it is unsuitable for a realistic calculation of the conductivity, and it does not include the phonon-defect interaction beyond the Born approximation level. Therefore we define the following empirical equation:

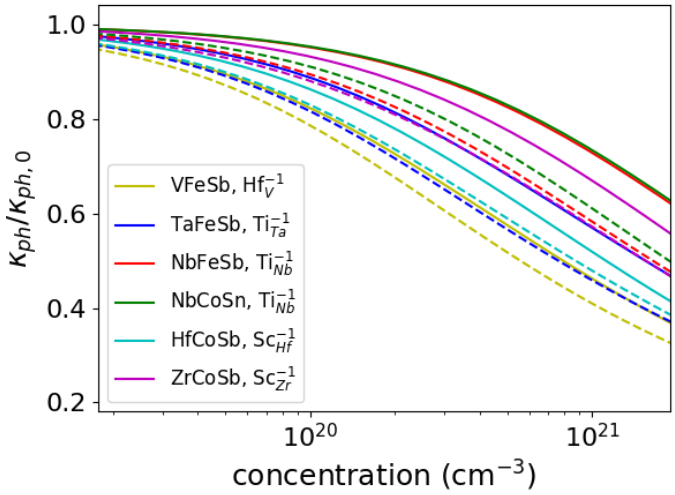

Figure 7.25: Thermal conductivity ratio for the "non Mathiessen" compounds. Continuous lines correspond to phonon-defect scattering rates modelled according to Eq. 3.80 with while dashed lines to the Matthiessen's rule applied to V_M and V_K.

$$\kappa_{\mathrm{ph}}(\chi,T) = \kappa_{\mathrm{bulk}}(300\mathrm{K})\left(\frac{300\mathrm{K}}{T}\right)\cdot\frac{\arctan[\sqrt{f(\chi,T)}]}{\sqrt{f(\chi,T)}}, \tag{7.6}$$

with

$$f(\chi,T) = \alpha\left(\frac{300\mathrm{K}}{T}\right)(\chi V_{uc})^{\beta}. \tag{7.7}$$

Table 7.4 lists the parameters α and β fitted for each compound and defect in the 300 K - 400 K temperature range. The small non-linearity with respect to the concentration has been included to better fit the high doping limit, although the β exponents are tightly clustered around $\beta_0 \equiv 1$. As this model involves both the contributions from V_M and V_K, which has proven to be important for several of the considered impurities, it can be used to estimate the phonon contribution to thermal transport in half-Heuslers and properly evaluate the thermoelectric efficiency. A comparison between the proposed analytical formula and the first principles calculations is shown in fig. 7.26 for the cases of $\mathrm{Hf_V^{-1}}$, $\mathrm{Ti_{Ta}^{-1}}$, $\mathrm{Hf_{Nb}^{-1}}$ (both in NbFeSb and NbCoSn) and $\mathrm{Sc_{Hf}^{-1}}$, which are the impurities with the steepest $\kappa_{\mathrm{ph}}/\kappa_{\mathrm{ph},0}$ ratio in our set.

	α	β
VFeSb, Hf_V^{-1}	116.444	0.946
VFeSb, Ti_V^{-1}	34.749	0.975
TaFeSb, Hf_{Ta}^{-1}	8.0567	0.895
TaFeSb, Ti_{Ta}^{-1}	55.414	0.930
TaFeSb, Zr_{Ta}^{-1}	40.428	0.894
TaFeSb, Mn_{Fe}^{-1}	4.305	0.864
TaFeSb, Sn_{Sb}^{-1}	3.490	0.936
NbFeSb, Hf_{Nb}^{-1}	137.689	1.065
NbFeSb, Ti_{Nb}^{-1}	27.681	0.999
NbFeSb, Zr_{Nb}^{-1}	15.306	0.930
NbFeSb, Mn_{Fe}^{-1}	4.456	0.939
NbFeSb, Sn_{Sb}^{-1}	4.761	0.969
TaCoSn, Hf_{Ta}^{-1}	11.765	0.975
NbCoSn, Hf_{Nb}^{-1}	107.918	1.068
NbCoSn, Ti_{Nb}^{-1}	24.936	0.979
NbCoSn, Zr_{Nb}^{-1}	14.114	0.922
HfCoSb, Sc_{Hf}^{-1}	85.389	0.977
HfCoSb, Sn_{Sb}^{-1}	3.974	0.928
ZrCoSb, Sc_{Zr}^{-1}	40.473	1.013
ZrCoSb, Sn_{Sb}^{-1}	5.321	0.978

Table 7.4: Parameters for the empirical model.

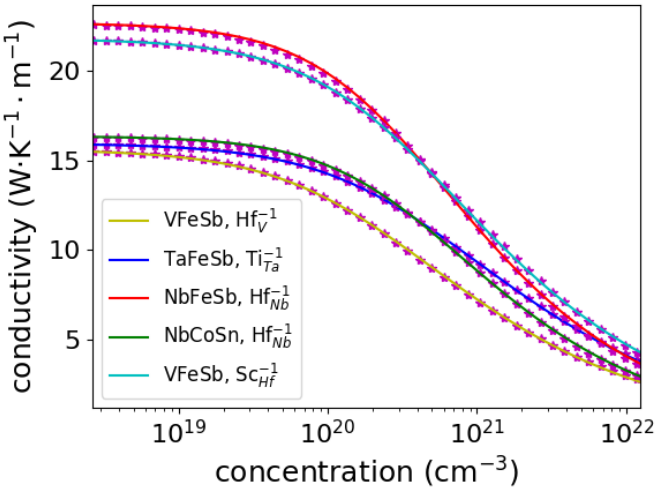

Figure 7.26: Continous lines: analytical model (Eq. 7.6). Star markers: *ab initio* data. The temperature is 300 K.

7.4 Discussion

We have computed the total scattering rates induced by substitutional impurities, considering the contributions from both the local change of mass V_M and of the bonds force constants V_K, for a selected group of half-Heusler compounds and their dopants. Aside from the magnitude of V_M, which can be inferred from table 5.1, the general finding is that the substitutions of transition metals produce a much larger V_K compared with the substitution of non-d-block elements, like Sb by Sn. This thus shows that if an element is replaced by an adjacent atom in the periodic table, the change in the local chemistry is not necessarily small. Amongst the transition metal substitutions, the one of Mn by Fe yields the smallest scattering rates. This could be attributed to the small vibrational density of states on the Fe atom in the acoustic frequency range of the studied compounds. The scattering probability by Fe substituting impurities is roughly proportional to this density of states, therefore being weak for the acoustic branches.

We have given a simple explanation for the observed behaviour, arguing that the strong d-orbital character of the considered compounds makes the electronic structure and IFCs much more sensible to impurities when the substituted atom is the one with the

d-character and/or when the host atom has a large phonon DOS weight. We have also computed *ab initio* the effect of phonon-defect scattering upon the concentration behaviour of the thermal conductivity for our set of materials and impurities, finding that κ_{ph} is much more reduced when transition metal elements are involved. In particular, the dopants that affect the thermal transport the most are Hf (replacing V and Nb in VFeSb, NbFeSb and NbCoSn), Sc (substituting Hf in HfCoSb), and Ti (for Ta in TaFeSb) with reductions ranging from 40 to 50% in the 10^{20}-10^{21} cm^{-3} concentration range.

We stress that we have only evaluated the effect of the perturbation induced by substitutional defects along with the intrinsic three-phonon and phonon-isotope scattering. However, other mechanisms to further reduce the thermal conductivity of half-Heusler compounds - like the electron-phonon interaction and boundary scattering [12, 215], or the formation of Frenkel defects [11] - have been suggested in past works. Our calculations on NbFeSb along with previous results [210] seem to imply that the scattering of acoustic phonons from holes and negative carriers is largely impaired and does not contribute to a substantial reduction of the lattice conductivity in these materials. On the other hand, Frenkel pairs provide much more scattering to phonons, although the formation of uncorrelated vacancies and interstitials is more favoured energetically and leads to a better agreement with the experiments at least in the case of ZrCoSb.

Finally, we have fitted the thermal conductivity curves to an analytical two-parameter model that may be employed when evaluating κ_{ph} at different temperatures and doping concentrations, and which could provide an easy way to study the impact of defects and phonon transport on the thermoelectric efficiency of HHs. The present findings show the general importance of both the impurity-induced mass and force constants perturbations upon thermal transport properties, and showcase general trends about the impact of the bond perturbation upon scattering of phonons. These results may be useful in the design of doped half-Heusler compounds for thermoelectric applications.

7.4.1 Computational details

The phonon calculations have been performed with the VASP [8, 9, 10] DFT code using the plane-augmented wave (PAW) [20, 191] formalism under the generalized gradient approximation (GGA) in the PBE [192, 193] parameterization. We have computed the second order force constants (IFC2) for all pristine and defect-laden systems in the case of a relaxed $4 \times 4 \times 4$ (192 atom) supercell using the small displacement method. The supercells and the atomic displacements are created with the help of the code *Phonopy* [2, 1], which is also employed to evaluate the force constants following DFT calculations. To calculate V_K, we first proceeded by taking the difference between the IFC2s of the pristine and the defect-laden system. Then we introduce the cutoffs R_{cut} and r_{cut} to account for the finite size of the perturbation as explained in subsection 5.7.1 of chapter 5. We have selected r_{cut} and R_{cut} to be 0.6-0.8 nm for all the considered dopants after convergence tests. The scattering T-matrix is then calculated using $V = V_K + V_M$ and the pristine retarded Green's function is evaluated using the analytical tetrahedron method and a 16x16x16 grid. To calculate the three-phonon scattering rates, we use the *thirdorder_vasp.py* code [128] in conjunction with *VASP* and *almaBTE* [143]. The phonon-substitution defect scattering rates are combined with the three-phonon and phonon-isotope scattering rates at the relaxation time approximation level using Matthiesen's rule inside the *almaBTE* code. We used a converged $28 \times 28 \times 28$ transport wave vector mesh to solve the phonon BTE. The validity of the SMRTA in the case of the pristine systems was tested by solving eq. 6.3 also in the $\Delta_\lambda \neq 0$ case. A good agreement between the relaxation time approximation and the full self-consistent solution was found for all the considered pristine materials in the considered 300 K - 400 K temperature range, with $|\kappa_{\text{ph}}^{\text{SMRTA}} - \kappa_{\text{ph}}^{\text{iter.}}|/\kappa_{\text{ph}}^{\text{iter.}} \leq 6\%$.

8

Conclusions

In the development of this thesis we have delved into the theory of phonon thermal transport and its dependence upon defect substitution. We have focused our attention on boron arsenide, a promising candidate for thermal management in electronics, and on a set of half-Heuslers materials that could potentially serve as converters of waste heat into electricity in a useful 500 - 800 °C range.

In the particular case of BAs we have studied group IV elements as dopants in virtue of their thermodynamical stability, defect formation energy and their dual acceptor and donor nature which could be exploited given the high n and p mobility of BAs. We have performed our calculations concerning C, Si and Ge doping in either neutral and charged states [187, 188] and in their donor and acceptor configuration depending on whether they substitute B or As.

We have found a rich phenomenology that can be summarised as follow. First of all the scattering induced by the change of mass does not follow the $\Delta M/M_0$ trend, a fact that can be explained in terms of the large mass mismatch between boron and arsenic masses. Secondly, we have found that neutral impurities present a much larger bond perturbation than the charged ones near the defect site and in the critical 4-8 THz frequency range for heat transport in BAs, a fact that can be qualitatively be attributed to a smaller change in the local electronic structure in presence of free carriers and with respect to the pristine system. This can be observed both by looking at suitably defined descriptors and at the thermal conductivity as a function of the impurity

concentration. Dopants like Ge_{As} and C_B appear to be apt for electronic applications as they only weakly affect the conductivity even at high concentrations $> 10^{19}$ cm^{-3}. In particular C_B is a potential candidate for *n* doping, although its higher formation energy with respect to its acceptor counterpart C_{As} makes its growth to be unsuitable under equilibrium conditions. On the other hand defects like Si_{As}, Si_B, C_{As} and Ge_B present a large effect on κ_{ph} even at low concentrations, with the conductivity reduced to half its pristine value at $\chi \sim 10^{19}$ cm^{-3}. Practically, all of them with the exception of Si_{As} are associated to both a large bond perturbation and a large mass perturbation. Our calculations support recent analysis [188] that suggested the presence of Si and C defects in the BAs precursors as the possible cause of its poor thermal transport properties in non-high quality crystals.

We have taken a step further in our analysis by studying the role of the thermodynamics of defect formation on the behaviour of κ_{ph} and considering not only the stable charged acceptors at low doping but also the effect of neutral acceptors and compensating donors that start to appear as χ is increased. To model the effect of the compensation on conductivity we have combined the Matthiessen's rule and the charge neutrality conditions into a unique formulation that presents dependence on the concentration of dopants and temperature as well. In the particular case of Ge doping, the weak dependence of the conductivity w.r.t. the concentration is replaced with a much sharper trend when both the neutral Ge_{As} acceptors and charged Ge_B donors - whose impact is stronger - kick in as the Fermi level approaches the pinning point and the acceptor level at $\chi \geq\sim 10^{19}$ cm^{-3}. In the case of C doping the observed behaviour is opposite, with the strong dependence on χ induced by the presence of C_{As} smoothened by C_B. These effects should be considered in the design of future boron arsenide based electronic devices. We also expect the phenomenology here encountered to be present in several more compounds, in particular for what concerns the transition between charged and neutral defect states, an effect that has been largely ignored in previous works on the lattice κ_{ph} of semiconductors and insulators. Furthermore, conductivity measurements may be appropriate for detecting the onset of compensation and be a valid alternative to Hall probes to extract the value and type of substitution defects in

samples.

In the case of the half-Heuslers (HHs) we have studied the set of $p-$type compounds and corresponding acceptors found by means of high-throughput calculations in [208]. Again, we have evaluated the scattering rates induced by substitution impurities, and descriptors have been introduced to better understand their effect on the conductivity. Finally we have shown how the various dopants in the defect-laden structures affect κ_{ph} with respect to its pristine value at room temperature and depending on the concentrations.

For all the considered materials we have found a strong *d*-orbital character near the electronic band gap, a fact that is perfectly consistent with the presence of transition metals in the HHs stoichiometry. We have observed a bond perturbation that is generally much stronger when the substituted atom belongs to the *d*-orbital group and weaker when it has *p*-character. Also, the importance of the phonon-defect scattering rates depends on the spectral weight (phDOS) of the substituted atom. Indeed, the phDOS tends to be smaller (larger) for light (heavy) elements in the range of acoustic frequencies. In the set of the materials and dopants that we have studied, the defect-induced scattering rates span two order of magnitude, whereby the poor decrease of the conductivity upon Sn doping is contrasted by the strong effect induced in VFeSb when vanadium is substituted by hafnium.

For several defects we have observed that the kinetic and potential perturbations, when treated separately with the Matthiessen's rule, overestimate the lowering of κ_{ph} as the concentration increases. This should be considered when fitting defect models to data for assessing the value of the ZT factor in doped compounds. Finally we have fitted *ab initio* calculations to an analytical model of the conductivity for bulk half-Heuslers that contains the effects of both mass and local bond perturbations. This model could be a valuable tool for thermoelectric efficiency evaluation in presence of defects, especially when the main scope of a calculation is related to the electronic part of ZT.

Concluding, this work shows the importance of first principles calculations to unveil how substitution impurities affect the lattice thermal transport in semiconductors.

The formulation herein introduced allows to probe the effects of dopants beyond the mass approximation and with good accuracy. In both the boron arsenide and half-Heuslers cases we have identified new trends and proposed candidates for doping that optimise thermal or thermoelectric properties. In the particular case of BAs we have been able to couple the thermal transport problem with the thermodynamics of defects, an approach that has been largely ignored in past works and that may be valuable in future studies and technological applications related to this material. In the case of half-Heuslers we have seen which defects give the larger reduction of the conductivity as a function of the concentration and we have observed a trend in the bond perturbation that is intimately related with the electronic and phononic structures of the parent compounds. We expect these results to be useful in the assessment of the role of substitution point defects on thermal transport properties for both high and low κ_{ph} semiconductors, to shed light on the role of impurity thermodynamics on phonon transport and to give an understanding about the origin and nature of the defect induced bond perturbations and their effect on the thermal conductivity for semiconductors.

Bibliography

[1] A Togo, F Oba, and I Tanaka. First-principles calculations of the ferroelastic transition between rutile-type and $CaCl_2$-type SiO_2 at high pressures. *Phys. rev. B*, 78:134106–134114, Oct 2008.

[2] A Togo and I Tanaka. First principles phonon calculations in materials science. *Scr. Mater.*, 108:1–5, Nov 2015.

[3] Anton S. Bochkarev, Ambroise van Roekeghem, Stefano Mossa, and Natalio Mingo. Anharmonic thermodynamics of vacancies using a neural network potential. *Phys. Rev. Materials*, 3:093803, Sep 2019.

[4] Jesús Carrete, Miquel López-Suárez, Martí Raya-Moreno, Anton S. Bochkarev, Miquel Royo, Georg K. H. Madsen, Xavier Cartoixà, Natalio Mingo, and Riccardo Rurali. Phonon transport across crystal-phase interfaces and twin boundaries in semiconducting nanowires. *Nanoscale*, 11(34):16007–16016, 2019.

[5] Jörg Behler. Atom-centered symmetry functions for constructing high-dimensional neural network potentials. *The Journal of Chemical Physics*, 134(7):074106, 2011.

[6] Terumasa Tadano and Shinji Tsuneyuki. Self-consistent phonon calculations of lattice dynamical properties in cubic $SrTiO_3$ with first-principles anharmonic force constants. *Phys. Rev. B*, 92:054301, Aug 2015.

[7] C. J. Glassbrenner and Glen A. Slack. Thermal Conductivity of Silicon and Germanium from 3°K to the Melting Point. *Phys. Rev.*, 134:A1058–A1069, May 1964.

[8] Georg Kresse and Jürgen Hafner. Ab initio molecular dynamics for liquid metals. *Physical Review B*, 47(1):558, 1993.

[9] G Kresse and J Hafner. Ab initio molecular-dynamics simulation of the liquid-metal–amorphous-semiconductor transition in germanium. *Physical Review B*, 49(20):14251, 1994.

[10] Georg Kresse and Jürgen Furthmüller. Efficient iterative schemes for ab initio total-energy calculations using a plane-wave basis set. *Physical Review B*, 54(16):11169, 1996.

[11] Ran He, Taishan Zhu, Yumei Wang, Ulrike Wolff, Jean-Christophe Jaud, Andrei Sotnikov, Pavel Potapov, Daniel Wolf, Pingjun Ying, Max Wood, Zhenhui Liu, Le Feng, Nicolas Perez Rodriguez, G. Jeffrey Snyder, Jeffrey C. Grossman, Kornelius Nielsch, and Gabi Schierning. Unveiling the phonon scattering mechanisms in half-heusler thermoelectric compounds. *Energy Environ. Sci.*, 13:5165–5176, 2020.

[12] Chenguang Fu, Shengqiang Bai, Yintu Liu, Yunshan Tang, Lidong Chen, Xinbing Zhao, and Tiejun Zhu. Realizing high figure of merit in heavy-band p-type half-Heusler thermoelectric materials. *Nature communications*, 6:8144, 09 2015.

[13] Feliciano Giustino, Marvin L. Cohen, and Steven G. Louie. Electron-phonon interaction using Wannier functions. *Phys. Rev. B*, 76:165108, Oct 2007.

[14] S. Poncé, E. R. Margine, C. Verdi, and F. Giustino. Electron-phonon coupling, transport and superconducting properties using maximally localized Wannier functions. *Computer Physics Communications*, 209:116–133, Dec 2016.

[15] P. Hohenberg and W. Kohn. Inhomogeneous Electron Gas. *Phys. Rev.*, 136:B864–B871, Nov 1964.

[16] Mel Levy, John P. Perdew, and Viraht Sahni. Exact differential equation for the density and ionization energy of a many-particle system. *Phys. Rev. A*, 30:2745–2748, Nov 1984.

[17] L. H. Thomas. The calculation of atomic fields. *Mathematical Proceedings of the Cambridge Philosophical Society*, 23(5):542â548, 1927.

[18] W. Kohn and L. J. Sham. Self-Consistent Equations Including Exchange and Correlation Effects. *Phys. Rev.*, 140:A1133–A1138, Nov 1965.

[19] Warren E. Pickett. Pseudopotential methods in condensed matter applications. *Computer Physics Reports*, 9(3):115 – 197, 1989.

[20] P. E. Blöchl. Projector augmented-wave method. *Phys. Rev. B*, 50:17953–17979, Dec 1994.

[21] Carsten Rostgaard. The projector augmented-wave method. *Arxiv, preprint*, 10 2009.

[22] R.G. Parr and W. Yang. *Density-Functional Theory of Atoms and Molecules*. Density-functional Theory of Atoms and Molecules. Oxford University Press, USA, 1994.

[23] David C. Langreth and John P. Perdew. Theory of nonuniform electronic systems. I. Analysis of the gradient approximation and a generalization that works. *Phys. Rev. B*, 21:5469–5493, Jun 1980.

[24] Axel D. Becke. A new mixing of Hartree Fock and local density functional theories. *The Journal of Chemical Physics*, 98(2):1372–1377, 1993.

[25] David Bohm and David Pines. A Collective Description of Electron Interactions. I. Magnetic Interactions. *Phys. Rev.*, 82:625–634, Jun 1951.

[26] David Pines and David Bohm. A Collective Description of Electron Interactions: II. Collective vs Individual Particle Aspects of the Interactions. *Phys. Rev.*, 85:338–353, Jan 1952.

[27] David Bohm and David Pines. A Collective Description of Electron Interactions: III. Coulomb Interactions in a Degenerate Electron Gas. *Phys. Rev.*, 92:609–625, Nov 1953.

[28] Murray Gell-Mann and Keith A. Brueckner. Correlation Energy of an Electron Gas at High Density. *Phys. Rev.*, 106:364–368, Apr 1957.

[29] Lars Hedin. New Method for Calculating the One-Particle Green's Function with Application to the Electron-Gas Problem. *Phys. Rev.*, 139:A796–A823, Aug 1965.

[30] F Aryasetiawan and O Gunnarsson. The GW method. *Reports on Progress in Physics*, 61(3):237–312, mar 1998.

[31] M. Methfessel and A. T. Paxton. High-precision sampling for Brillouin-zone integration in metals. *Phys. Rev. B*, 40:3616–3621, Aug 1989.

[32] Nicola Marzari, David Vanderbilt, Alessandro De Vita, and M. C. Payne. Thermal Contraction and Disordering of the Al(110) Surface. *Phys. Rev. Lett.*, 82:3296–3299, Apr 1999.

[33] P. Kratzer and J. Neugebauer. The Basics of Electronic Structure Theory for Periodic Systems. *Frontiers in Chemistry*, 7, 2019.

[34] M. Born and R. Oppenheimer. Zur Quantentheorie der Molekeln. *Annalen der Physik*, 389(20):457–484, January 1927.

[35] R. P. Feynman. Forces in Molecules. *Phys. Rev.*, 56:340–343, Aug 1939.

[36] R. Car and M. Parrinello. Unified Approach for Molecular Dynamics and Density-Functional Theory. *Phys. Rev. Lett.*, 55:2471–2474, Nov 1985.

[37] Alessandro Laio and Michele Parrinello. Escaping free-energy minima. *Proceedings of the National Academy of Sciences*, 99(20):12562–12566, 2002.

[38] W. Kohn. Image of the Fermi Surface in the Vibration Spectrum of a Metal. *Phys. Rev. Lett.*, 2:393–394, May 1959.

[39] Felix T. Smith. Diabatic and Adiabatic Representations for Atomic Collision Problems. *Phys. Rev.*, 179:111–123, Mar 1969.

[40] Michael F. Herman. Nonadiabatic semiclassical scattering. I. Analysis of generalized surface hopping procedures. *The Journal of Chemical Physics*, 81(2):754–763, 1984.

[41] John C. Tully. Molecular dynamics with electronic transitions. *The Journal of Chemical Physics*, 93(2):1061–1071, 1990.

[42] Léon Van Hove. The Occurrence of Singularities in the Elastic Frequency Distribution of a Crystal. *Phys. Rev.*, 89:1189–1193, Mar 1953.

[43] M. T. Yin and Marvin L. Cohen. Microscopic Theory of the Phase Transformation and Lattice Dynamics of Si. *Phys. Rev. Lett.*, 45:1004–1007, Sep 1980.

[44] K. Kunc and Richard M. Martin. Ab initio determination of static, dynamic and dielectric properties of semiconductors. *Physica B+C*, 117-118:511 – 516, 1983.

[45] K. Kunc and Richard M. Martin. Ab Initio Force Constants of GaAs: A New Approach to Calculation of Phonons and Dielectric Properties. *Phys. Rev. Lett.*, 48:406–409, Feb 1982.

[46] M. T. Yin and Marvin L. Cohen. Ab initio calculation of the phonon dispersion relation: Application to Si. *Phys. Rev. B*, 25:4317–4320, Mar 1982.

[47] W. Frank, C. Elsässer, and M. Fähnle. Ab initio Force-Constant Method for Phonon Dispersions in Alkali Metals. *Phys. Rev. Lett.*, 74:1791–1794, Mar 1995.

[48] K. Parlinski, Z. Q. Li, and Y. Kawazoe. First-Principles Determination of the Soft Mode in Cubic ZrO_2. *Phys. Rev. Lett.*, 78:4063–4066, May 1997.

[49] G J Ackland, M C Warren, and S J Clark. Practical methods in ab initio lattice dynamics. *Journal of Physics: Condensed Matter*, 9(37):7861–7872, sep 1997.

[50] Stefano Baroni, Paolo Giannozzi, and Andrea Testa. Green's function approach to linear response in solids. *Phys. Rev. Lett.*, 58:1861–1864, May 1987.

[51] Paolo Giannozzi, Stefano de Gironcoli, Pasquale Pavone, and Stefano Baroni. Ab initio calculation of phonon dispersions in semiconductors. *Phys. Rev. B*, 43:7231–7242, Mar 1991.

[52] Xavier Gonze. Perturbation expansion of variational principles at arbitrary order. *Phys. Rev. A*, 52:1086–1095, Aug 1995.

[53] Stefano Baroni, Stefano de Gironcoli, Andrea Dal Corso, and Paolo Giannozzi. Phonons and related crystal properties from density-functional perturbation theory. *Rev. Mod. Phys.*, 73:515–562, Jul 2001.

[54] Stefano de Gironcoli. Lattice dynamics of metals from density-functional perturbation theory. *Phys. Rev. B*, 51:6773–6776, Mar 1995.

[55] Fredrik Eriksson, Erik Fransson, and Paul Erhart. The Hiphive Package for the Extraction of High-Order Force Constants by Machine Learning. *Advanced Theory and Simulations*, 2:1800184, 02 2019.

[56] Jörg Behler and Michele Parrinello. Generalized Neural-Network Representation of High-Dimensional Potential-Energy Surfaces. *Phys. Rev. Lett.*, 98:146401, Apr 2007.

[57] E. J. Candes and M. B. Wakin. An Introduction To Compressive Sampling. *IEEE Signal Processing Magazine*, 25(2):21–30, 2008.

[58] Fei Zhou, Weston Nielson, Yi Xia, and Vidvuds Ozoliņš. Lattice Anharmonicity and Thermal Conductivity from Compressive Sensing of First-Principles Calculations. *Phys. Rev. Lett.*, 113:185501, Oct 2014.

[59] G. Cybenko. Approximation by superpositions of a sigmoidal function. *Mathematics of Control, Signals and Systems*, 2(4):303–314, Dec 1989.

[60] Jörg Behler. Perspective: Machine learning potentials for atomistic simulations. *The Journal of Chemical Physics*, 145(17):170901, 2016.

[61] M.T. Dove, M.F. Hochella, R.C. Liebermann, and A. Putnis. *Introduction to Lattice Dynamics*. Cambridge Topics in Mineral Physics and Chemistry. Cambridge University Press, 1993.

[62] D.C. Wallace. *Thermodynamics of Crystals*. Dover books on physics. Dover Publications, 1998.

[63] N. R. Werthamer. Self-Consistent Phonon Formulation of Anharmonic Lattice Dynamics. *Phys. Rev. B*, 1:572–581, Jan 1970.

[64] P. Souvatzis, O. Eriksson, M. I. Katsnelson, and S. P. Rudin. Entropy Driven Stabilization of Energetically Unstable Crystal Structures Explained from First Principles Theory. *Phys. Rev. Lett.*, 100:095901, Mar 2008.

[65] O. Hellman, I. A. Abrikosov, and S. I. Simak. Lattice dynamics of anharmonic solids from first principles. *Phys. Rev. B*, 84:180301, Nov 2011.

[66] Ion Errea, Matteo Calandra, and Francesco Mauri. First-principles theory of anharmonicity and the inverse isotope effect in superconducting palladium-hydride compounds. *Phys. Rev. Lett.*, 111:177002, Oct 2013.

[67] Ambroise van Roekeghem, Jesús Carrete, and Natalio Mingo. Quantum self-consistent ab-initio lattice dynamics. *Computer Physics Communications*, page 107945, 2021.

[68] Bourgoin Lannoo. Point Defects in Semiconductors I, Theoretical Aspects. Von M. Lannoo, J. Bourgoin. *Physik in unserer Zeit*, 13(4):127–128, 1982.

[69] P.A. Varotsos and K.D. Alexopoulos. *Thermodynamics of Point Defects and Their Relation with Bulk Properties*. Defects in crystalline solids. North-Holland, 1986.

[70] Christoph Freysoldt, Blazej Grabowski, Tilmann Hickel, Jörg Neugebauer, Georg Kresse, Anderson Janotti, and Chris G. Van de Walle. First-principles calculations for point defects in solids. *Rev. Mod. Phys.*, 86:253–305, Mar 2014.

[71] G. Makov and M. C. Payne. Periodic boundary conditions in ab initio calculations. *Phys. Rev. B*, 51:4014–4022, Feb 1995.

[72] Clas Persson, Yu-Jun Zhao, Stephan Lany, and Alex Zunger. *n*-type doping of $CuInSe_2$ and $CuGaSe_2$. *Phys. Rev. B*, 72:035211, Jul 2005.

[73] David Segev, Anderson Janotti, and Chris G. Van de Walle. Self-consistent band-gap corrections in density functional theory using modified pseudopotentials. *Phys. Rev. B*, 75:035201, Jan 2007.

[74] Malcolm W. Chase. *NIST-JANAF thermochemical tables*. American Institute of Physics, -1, 1998.

[75] R. W. Gurney and N. F. Mott. Conduction in polar crystals. iii. on the colour centres in alkali-halide crystals. *Trans. Faraday Soc.*, 34:506–511, 1938.

[76] S. R. Tibbs. Electron energy levels in nacl. *Trans. Faraday Soc.*, 35:1471–1484, 1939.

[77] Dr. Adolph Fick. V. on liquid diffusion. *The London, Edinburgh, and Dublin Philosophical Magazine and Journal of Science*, 10(63):30–39, 1855.

[78] Lars Onsager. Reciprocal Relations in Irreversible Processes. I. *Phys. Rev.*, 37:405–426, Feb 1931.

[79] Lars Onsager. Reciprocal Relations in Irreversible Processes. II. *Phys. Rev.*, 38:2265–2279, Dec 1931.

[80] S. R. de Groot and P. Mazur. Extension of Onsager's Theory of Reciprocal Relations. I. *Phys. Rev.*, 94:218–224, Apr 1954.

[81] P. Mazur and S. R. de Groot. Extension of Onsager's Theory of Reciprocal Relations. II. *Phys. Rev.*, 94:224–226, Apr 1954.

[82] Stefano Baroni, Riccardo Bertossa, Loris Ercole, Federico Grasselli, and Aris Marcolongo. *Heat Transport in Insulators from Ab Initio Green-Kubo Theory*, pages 809–844. Springer International Publishing, Cham, 2020.

[83] Melville S. Green. Markoff Random Processes and the Statistical Mechanics of Time-Dependent Phenomena. II. Irreversible Processes in Fluids. *The Journal of Chemical Physics*, 22(3):398–413, March 1954.

[84] Ryogo Kubo. Statistical-Mechanical Theory of Irreversible Processes. I. *Journal of the Physical Society of Japan*, 12(6):570–586, June 1957.

[85] Eugene Helfand. Transport Coefficients from Dissipation in a Canonical Ensemble. *Phys. Rev.*, 119:1–9, Jul 1960.

[86] Raffaele Resta and David Vanderbilt. *Theory of Polarization: A Modern Approach*, pages 31–68. Springer Berlin Heidelberg, Berlin, Heidelberg, 2007.

[87] Christian Carbogno, Rampi Ramprasad, and Matthias Scheffler. Ab Initio Green-Kubo Approach for the Thermal Conductivity of Solids. *Phys. Rev. Lett.*, 118:175901, Apr 2017.

[88] Jie Chen, Gang Zhang, and Baowen Li. How to Improve The Accuracy of Equilibrium Molecular Dynamics For Computation of Thermal Conductivity? *Physics Letters, Section A: General, Atomic and Solid State Physics*, 374, 05 2010.

[89] Denis J. Evans. Homogeneous nemd algorithm for thermal conductivity application of non-canonical linear response theory. *Physics Letters A*, 91(9):457 – 460, 1982.

[90] T. M. Gibbons and S. K. Estreicher. Impact of Impurities on the Thermal Conductivity of Semiconductor Nanostructures: First-Principles Theory. *Phys. Rev. Lett.*, 102:255502, Jun 2009.

[91] Stephen Stackhouse, Lars Stixrude, and Bijaya B. Karki. Thermal Conductivity of Periclase (MgO) from First Principles. *Phys. Rev. Lett.*, 104:208501, May 2010.

[92] B Dongre, T Wang, and G K H Madsen. Comparison of the Green–Kubo and homogeneous non-equilibrium molecular dynamics methods for calculating thermal conductivity. *Modelling and Simulation in Materials Science and Engineering*, 25(5):054001, may 2017.

[93] Philip B. Allen and Joseph L. Feldman. Thermal Conductivity of Glasses: Theory and Application to Amorphous Si. *Phys. Rev. Lett.*, 62:645–648, Feb 1989.

[94] Philip B. Allen and Joseph L. Feldman. Thermal conductivity of disordered harmonic solids. *Phys. Rev. B*, 48:12581–12588, Nov 1993.

[95] K. Huang. *Statistical Mechanics*. John Wiley and Sons, 2000.

[96] Georg Madsen and David Singh. BoltzTraP. A code for calculating band-structure dependent quantities. *Computer Physics Communications*, 175:67–71, 07 2006.

[97] G. K. H. Madsen, J. Carrete, and M. Verstraete. BoltzTraP2, a program for interpolating band structures and calculating semi-classical transport coefficients. *Comput. Phys. Commun.*, 231:140–145, 2018.

[98] Bolin Liao, Bo Qiu, Jiawei Zhou, Samuel Huberman, Keivan Esfarjani, and Gang Chen. Significant Reduction of Lattice Thermal Conductivity by the Electron-Phonon Interaction in Silicon with High Carrier Concentrations: A First-Principles Study. *Phys. Rev. Lett.*, 114:115901, Mar 2015.

[99] Natalio Mingo, K. Esfarjani, D. A. Broido, and D. A. Stewart. Cluster scattering effects on phonon conduction in graphene. *Phys. Rev. B*, 81:045408, Jan 2010.

[100] E. N. Economou. *Green's Functions in Quantum Physics*. Springer, 2006.

[101] Andrea Cepellotti and Nicola Marzari. Thermal Transport in Crystals as a Kinetic Theory of Relaxons. *Phys. Rev. X*, 6:041013, Oct 2016.

[102] Tianli Feng, Lucas Lindsay, and Xiulin Ruan. Four-phonon scattering significantly reduces intrinsic thermal conductivity of solids. *Phys. Rev. B*, 96:161201, Oct 2017.

[103] Tianli Feng and Xiulin Ruan. Quantum mechanical prediction of four-phonon scattering rates and reduced thermal conductivity of solids. *Phys. Rev. B*, 93:045202, Jan 2016.

[104] Navaneetha K. Ravichandran and David Broido. Unified first-principles theory of thermal properties of insulators. *Phys. Rev. B*, 98:085205, Aug 2018.

[105] Shin-ichiro Tamura. Isotope scattering of dispersive phonons in Ge. *Physical Review B*, 27(2):858, 1983.

[106] Shin-ichiro Tamura. Isotope scattering of large-wave-vector phonons in GaAs and InSb: Deformation-dipole and overlap-shell models. *Phys. Rev. B*, 30:849–854, Jul 1984.

[107] M. Omini and Amelia Carolina Sparavigna. Effect of phonon scattering by isotope impurities on the thermal conductivity of dielectric solids. *Physica B: Condensed Matter*, 233:230–240, 05 1997.

[108] R.H. Landau. *Quantum Mechanics II*. Wiley, 1990.

[109] N.F. Mott and H.S.W. Massey. *The Theory of Atomic Collisions, by N.F. Mott and H.S.W. Massey. 2nd Edition*. Clarendon Press (printed by C. Batey), 1949.

[110] D. Walton. *Phonon-Defect Interaction*, pages 393–440. Springer US, Boston, MA, 1975.

[111] Fumiko Yonezawa and Kazuo Morigaki. Coherent Potential Approximation. Basic concepts and applications. *Progress of Theoretical Physics Supplement*, 53:1–76, 01 1973.

[112] Alex Zunger, S.-H. Wei, L. G. Ferreira, and James E. Bernard. Special quasirandom structures. *Phys. Rev. Lett.*, 65:353–356, Jul 1990.

[113] Marco Arrigoni, Jesús Carrete, Natalio Mingo, and Georg K. H. Madsen. First-principles quantitative prediction of the lattice thermal conductivity in random semiconductor alloys: The role of force-constant disorder. *Phys. Rev. B*, 98:115205, Sep 2018.

[114] A.Neil W. Ashcroft and N. David Mermin. *Solid State Physics*. HRW international editions. Holt, Rinehart and Winston, 1976.

[115] H. Fröhlich. Electrons in lattice fields. *Advances in Physics*, 3(11):325–361, July 1954.

[116] Philip B. Allen. Neutron Spectroscopy of Superconductors. *Phys. Rev. B*, 6:2577–2579, Oct 1972.

[117] Nakib H. Protik and David A. Broido. Coupled transport of phonons and carriers in semiconductors: A case study of *n*-doped GaAs. *Phys. Rev. B*, 101:075202, Feb 2020.

[118] J. Bardeen and W. Shockley. Deformation Potentials and Mobilities in Non-Polar Crystals. *Phys. Rev.*, 80:72–80, Oct 1950.

[119] Conyers Herring and Erich Vogt. Transport and Deformation-Potential Theory for Many-Valley Semiconductors with Anisotropic Scattering. *Phys. Rev.*, 101:944–961, Feb 1956.

[120] J. M. Hinckley and J. Singh. Influence of substrate composition and crystallographic orientation on the band structure of pseudomorphic Si-Ge alloy films. *Phys. Rev. B*, 42:3546–3566, Aug 1990.

[121] J.M. Ziman. *Electrons and Phonons: The Theory of Transport Phenomena in Solids*. International series of monographs on physics. OUP Oxford, 2001.

[122] H.B.G. Casimir. Note on the conduction of heat in crystals. *Physica*, 5(6):495 – 500, 1938.

[123] Xiaokun Gu, Yujie Wei, Xiaobo Yin, Baowen Li, and Ronggui Yang. Colloquium: Phononic thermal properties of two-dimensional materials. *Rev. Mod. Phys.*, 90:041002, Nov 2018.

[124] Jean-Savin Heron, Chandan Bera, Thierry Fournier, Natalio Mingo, and Olivier Bourgeois. Blocking phonons via nanoscale geometrical design. *Phys. Rev. B*, 82:155458, Oct 2010.

[125] J. Carrete, L. J. Gallego, L. M. Varela, and N. Mingo. Surface roughness and thermal conductivity of semiconductor nanowires: Going below the Casimir limit. *Phys. Rev. B*, 84:075403, Aug 2011.

[126] Bjorn Vermeersch, Jesús Carrete, and Natalio Mingo. Cross-plane heat conduction in thin films with ab-initio phonon dispersions and scattering rates. *Applied Physics Letters*, 108(19):193104, 2016.

[127] Bjorn Vermeersch, Jesús Carrete, Natalio Mingo, and Ali Shakouri. Superdiffusive heat conduction in semiconductor alloys. I. Theoretical foundations. *Phys. Rev. B*, 91:085202, Feb 2015.

[128] Wu Li, Lucas Lindsay, David A. Broido, Derek A. Stewart, and Natalio Mingo. Thermal conductivity of bulk and nanowire $Mg_2Si_xSn_{1-x}$ alloys from first principles. *Phys. Rev. B*, 86:174307, 2012.

[129] N. Mingo and D. A. Broido. Length Dependence of Carbon Nanotube Thermal Conductivity and the "Problem of Long Waves". *Nano Letters*, 5(7):1221–1225, Jul 2005.

[130] C. W. Chang, A. M. Fennimore, A. Afanasiev, D. Okawa, T. Ikuno, H. Garcia, Deyu Li, A. Majumdar, and A. Zettl. Isotope Effect on the Thermal Conductivity of Boron Nitride Nanotubes. *Phys. Rev. Lett.*, 97:085901, Aug 2006.

[131] Ivana Savić, Natalio Mingo, and Derek A. Stewart. Phonon Transport in Isotope-Disordered Carbon and Boron-Nitride Nanotubes: Is Localization Observable? *Phys. Rev. Lett.*, 101:165502, Oct 2008.

[132] Derek A. Stewart, Ivana Savić, and Natalio Mingo. First-Principles Calculation of the Isotope Effect on Boron Nitride Nanotube Thermal Conductivity. *Nano Letters*, 9(1):81–84, Jan 2009.

[133] Taneli Juntunen, Osmo Vänskä, and Ilkka Tittonen. Anderson Localization Quenches Thermal Transport in Aperiodic Superlattices. *Phys. Rev. Lett.*, 122:105901, Mar 2019.

[134] M. N. Luckyanova, J. Mendoza, H. Lu, B. Song, S. Huang, J. Zhou, M. Li, Y. Dong, H. Zhou, J. Garlow, L. Wu, B. J. Kirby, A. J. Grutter, A. A. Puretzky, Y. Zhu, M. S. Dresselhaus, A. Gossard, and G. Chen. Phonon localization in heat conduction. *Science Advances*, 4(12), 2018.

[135] W. A. Little. The transport of heat between dissimilar solids at low temperatures. *Canadian Journal of Physics*, 37:334, January 1959.

[136] E. T. Swartz and R. O. Pohl. Thermal resistance at interfaces. *Applied Physics Letters*, 51(26):2200–2202, 1987.

[137] E. T. Swartz and R. O. Pohl. Thermal boundary resistance. *Rev. Mod. Phys.*, 61:605–668, Jul 1989.

[138] Sridhar Sadasivam, Yuhang Che, Zhen Huang, Liang Chen, Satish Kumar, and Timothy Fisher. The Atomistic Green's Function Method for Interfacial Phonon Transport. *Annual Review of Heat Transfer*, 17, Jan 2014.

[139] J.-S. Wang, J. Wang, and J. T. Lü. Quantum thermal transport in nanostructures. *The European Physical Journal B*, 62(4):381–404, Apr 2008.

[140] N. Mingo. Anharmonic phonon flow through molecular-sized junctions. *Phys. Rev. B*, 74:125402, Sep 2006.

[141] L. V. Keldysh. Diagram technique for nonequilibrium processes. *Zh. Eksp. Teor. Fiz.*, 47:1515–1527, 1964.

[142] Patrick Hopkins, John Duda, and Pamela Norris. Anharmonic Phonon Interactions at Interfaces and Contributions to Thermal Boundary Conductance. *Journal of Heat Transfer*, 133:062401, Jun 2011.

[143] Jesús Carrete, Bjorn Vermeersch, Ankita Katre, Ambroise van Roekeghem, Tao Wang, Georg K.H. Madsen, and Natalio Mingo. almaBTE : A solver of the space-time dependent boltzmann transport equation for phonons in structured materials. *Computer Physics Communications*, 220:351 – 362, 2017.

[144] Ambroise van Roekeghem, Bjorn Vermeersch, Jesús Carrete, and Natalio Mingo. Thermal Resistance of GaN/AlN Graded Interfaces. *Phys. Rev. Applied*, 11:034036, Mar 2019.

[145] Giorgia Fugallo, Michele Lazzeri, Lorenzo Paulatto, and Francesco Mauri. Ab initio variational approach for evaluating lattice thermal conductivity. *Phys. Rev. B*, 88:045430, Jul 2013.

[146] Joseph Callaway. Model for Lattice Thermal Conductivity at Low Temperatures. *Phys. Rev.*, 113:1046–1051, Feb 1959.

[147] M. G. Holland. Analysis of Lattice Thermal Conductivity. *Phys. Rev.*, 132:2461–2471, Dec 1963.

[148] D. T. Morelli, J. P. Heremans, and G. A. Slack. Estimation of the isotope effect on the lattice thermal conductivity of group IV and group III-V semiconductors. *Phys. Rev. B*, 66:195304, Nov 2002.

[149] Michele Simoncelli, Nicola Marzari, and Andrea Cepellotti. Generalization of Fourier's Law into Viscous Heat Equations. *Phys. Rev. X*, 10:011019, Jan 2020.

[150] Dongliang Zhao, Xin Qian, Xiaokun Gu, Saad Jajja, and Ronggui Yang. Measurement Techniques for Thermal Conductivity and Interfacial Thermal Conductance of Bulk and Thin Film Materials. *Journal of Electronic Packaging*, 138, 12 2016.

[151] O. Maldonado. Pulse method for simultaneous measurement of electric thermopower and heat conductivity at low temperatures. *Cryogenics*, 32(10):908 – 912, 1992.

[152] Mattias Gustavsson, Ernest Karawacki, and Silas E. Gustafsson. Thermal conductivity, thermal diffusivity, and specific heat of thin samples from transient measurements with hot disk sensors. *Review of Scientific Instruments*, 65(12):3856–3859, 1994.

[153] W. J. Parker, R. J. Jenkins, C. P. Butler, and G. L. Abbott. Flash Method of Determining Thermal Diffusivity, Heat Capacity, and Thermal Conductivity. *Journal of Applied Physics*, 32(9):1679–1684, 1961.

[154] S. Min, J. Blumm, and A. Lindemann. A new laser flash system for measurement of the thermophysical properties. *Thermochimica Acta*, 455(1):46 – 49, 2007. 6th KSTP Symposium.

[155] David G. Cahill, Henry E. Fischer, Tom Klitsner, E. T. Swartz, and R. O. Pohl. Thermal conductivity of thin films: Measurements and understanding. *Journal of Vacuum Science and Technology A*, 7(3):1259–1266, May 1989.

[156] David Cahill. Thermal conductivity measurement from 30 to 750 K: the 3ω method. *Review of Scientific Instruments*, 61:802 – 808, 03 1990.

[157] Allan Rosencwaig and Allen Gersho. Theory of the photoacoustic effect with solids. *Journal of Applied Physics*, 47(1):64–69, 1976.

[158] Allan Rosencwaig. Thermal-Wave Imaging. *Science*, 218(4569):223–228, 1982.

[159] W. S. Capinski, H. J. Maris, T. Ruf, M. Cardona, K. Ploog, and D. S. Katzer. Thermal-conductivity measurements of GaAs/AlAs superlattices using a picosecond optical pump-and-probe technique. *Phys. Rev. B*, 59:8105–8113, Mar 1999.

[160] Aaron J. Schmidt, Ramez Cheaito, and Matteo Chiesa. Characterization of thin metal films via frequency-domain thermoreflectance. *Journal of Applied Physics*, 107(2):024908, 2010.

[161] Vivek Mishra, Corey L. Hardin, Javier E. Garay, and Chris Dames. A 3 omega method to measure an arbitrary anisotropic thermal conductivity tensor. *Review of Scientific Instruments*, 86(5):054902, 2015.

[162] Jie Zhu, Dawei Tang, Wei Wang, Jun Liu, Kristopher W. Holub, and Ronggui Yang. Ultrafast thermoreflectance techniques for measuring thermal conductivity and interface thermal conductance of thin films. *Journal of Applied Physics*, 108(9):094315, 2010.

[163] David G. Cahill. Analysis of heat flow in layered structures for time-domain thermoreflectance. *Review of Scientific Instruments*, 75(12):5119–5122, 2004.

[164] Ruxandra M. Costescu, Marcel A. Wall, and David G. Cahill. Thermal conductance of epitaxial interfaces. *Phys. Rev. B*, 67:054302, Feb 2003.

[165] Te-Huan Liu, Bai Song, Laureen Meroueh, Zhiwei Ding, Qichen Song, Jiawei Zhou, Mingda Li, and Gang Chen. Simultaneously high electron and hole mobilities in cubic boron-V compounds: BP, BAs, and BSb. *Phys. Rev. B*, 98:081203, Aug 2018.

[166] Joon Sang Kang, Man Li, Huan Wu, Huuduy Nguyen, and Yongjie Hu. Basic physical properties of cubic boron arsenide. *Applied Physics Letters*, 115(12):122103, 2019.

[167] Bing Lv, Yucheng Lan, Xiqu Wang, Qian Zhang, Yongjie Hu, Allan J. Jacobson, David Broido, Gang Chen, Zhifeng Ren, and Ching-Wu Chu. Experimental study of the proposed super-thermal-conductor: BAs. *Applied Physics Letters*, 106(7):074105, 2015.

[168] Joon Sang Kang, Man Li, Huan Wu, Huuduy Nguyen, and Yongjie Hu. Experimental observation of high thermal conductivity in boron arsenide. *Science*, 361(6402):575–578, August 2018.

[169] Sheng Li, Qiye Zheng, Yinchuan Lv, Xiaoyuan Liu, Xiqu Wang, Pinshane Y. Huang, David G. Cahill, and Bing Lv. High thermal conductivity in cubic boron arsenide crystals. *Science*, 361(6402):579–581, August 2018.

[170] Fei Tian, Bai Song, Xi Chen, Navaneetha K Ravichandran, Yinchuan Lv, Ke Chen, Sean Sullivan, Jaehyun Kim, Yuanyuan Zhou, Te-Huan Liu, et al. Unusual high thermal conductivity in boron arsenide bulk crystals. *Science*, 361(6402):582–585, 2018.

[171] L. Lindsay, D. A. Broido, and T. L. Reinecke. First-Principles Determination of Ultrahigh Thermal Conductivity of Boron Arsenide: A Competitor for Diamond? *Phys. Rev. Lett.*, 111:025901, Jul 2013.

[172] G.A. Slack. Nonmetallic crystals with high thermal conductivity. *Journal of Physics and Chemistry of Solids*, 34(2):321 – 335, 1973.

[173] Lucas Lindsay and D Broido. Three-phonon phase space and lattice thermal conductivity in semiconductors. *Journal of Physics: Condensed Matter*, 20:165209, 03 2008.

[174] M. Lax, P. Hu, and V. Narayanamurti. Spontaneous phonon decay selection rule: *n* and *u* processes. *Phys. Rev. B*, 23:3095–3097, Mar 1981.

[175] Navaneetha K. Ravichandran and David Broido. Phonon-Phonon Interactions in Strongly Bonded Solids: Selection Rules and Higher-Order Processes. *Phys. Rev. X*, 10:021063, Jun 2020.

[176] Navaneetha K. Ravichandran and David Broido. Non-monotonic pressure dependence of the thermal conductivity of boron arsenide. *Nature Communications*, 10, 2019.

[177] L. Lindsay, D. A. Broido, Jesús Carrete, Natalio Mingo, and T. L. Reinecke. Anomalous pressure dependence of thermal conductivities of large mass ratio compounds. *Phys. Rev. B*, 91:121202, Mar 2015.

[178] Wu Li, Jesús Carrete, Nebil A. Katcho, and Natalio Mingo. ShengBTE: a solver of the Boltzmann transport equation for phonons. *Comp. Phys. Commun.*, 185:1747â1758, 2014.

[179] Jaehyun Kim, Daniel A. Evans, Daniel P. Sellan, Owen M. Williams, Eric Ou, Alan H. Cowley, and Li Shi. Thermal and thermoelectric transport measurements of an individual boron arsenide microstructure. *Applied Physics Letters*, 108(20):201905, 2016.

[180] Qiang Zheng, Carlos A. Polanco, Mao-Hua Du, Lucas R. Lindsay, Miaofang Chi, Jiaqiang Yan, and Brian C. Sales. Antisite Pairs Suppress the Thermal Conductivity of BAs. *Phys. Rev. Lett.*, 121:105901, Sep 2018.

[181] Nakib Haider Protik, Jesús Carrete, Nebil A. Katcho, Natalio Mingo, and David Broido. Ab initio study of the effect of vacancies on the thermal conductivity of boron arsenide. *Phys. Rev. B*, 94:045207, Jul 2016.

[182] C. A. Ratsifaritana and P. G. Klemens. *Scattering of Phonons by Vacancies*, pages 259–262. Springer US, Boston, MA, 1980.

[183] P. Klemens. Theory of Thermal Conduction in Thin Ceramic Films. *International Journal of Thermophysics*, 22:265–275, 01 2001.

[184] N. A. Katcho, J. Carrete, Wu Li, and N. Mingo. Effect of nitrogen and vacancy defects on the thermal conductivity of diamond: An ab initio Green's function approach. *Phys. Rev. B*, 90:094117, Sep 2014.

[185] L. Lindsay, D. A. Broido, and T. L. Reinecke. Phonon-isotope scattering and thermal conductivity in materials with a large isotope effect: A first-principles study. *Physical Review B*, 88(14):144306, October 2013.

[186] Mauro Fava, Nakib Haider Protik, Chunhua Li, Navaneetha Krishnan Ravichandran, Jesús Carrete, Ambroise van Roekeghem, Georg K. H. Madsen, Natalio Mingo, and David Broido. How dopants limit the ultrahigh thermal conductivity of boron arsenide: a first principles study. *npj Computational Materials*, 7(1):54, Apr 2021.

[187] S. Chae, K. Mengle, J. T. Heron, and E. Kioupakis. Point defects and dopants of boron arsenide from first-principles calculations: Donor compensation and doping asymmetry. *Applied Physics Letters*, 113(21):212101, November 2018.

[188] John L. Lyons, Joel B. Varley, Evan R. Glaser, Jaime A. Freitas, James C. Culbertson, Fei Tian, Geethal Amila Gamage, Haoran Sun, Hamidreza Ziyaee, and Zhifeng Ren. Impurity-derived p-type conductivity in cubic boron arsenide. *Applied Physics Letters*, 113(25):251902, 2018.

[189] Kyle Bushick, Kelsey Mengle, Nocona Sanders, and Emmanouil Kioupakis. Band structure and carrier effective masses of boron arsenide: Effects of quasiparticle and spin-orbit coupling corrections. *Applied Physics Letters*, 114(2):022101, 2019.

[190] Ke Chen, Bai Song, Navaneetha K. Ravichandran, Qiye Zheng, Xi Chen, Hwijong Lee, Haoran Sun, Sheng Li, Geethal Amila Gamage Udalamatta Gamage, Fei Tian, Zhiwei Ding, Qichen Song, Akash Rai, Hanlin Wu, Pawan Koirala, Aaron J. Schmidt, Kenji Watanabe, Bing Lv, Zhifeng Ren, Li Shi, David G. Cahill, Takashi Taniguchi, David Broido, and Gang Chen. Ultrahigh thermal conductivity in isotope-enriched cubic boron nitride. *Science*, 367(6477):555–559, January 2020.

[191] Georg Kresse and D Joubert. From ultrasoft pseudopotentials to the projector augmented-wave method. *Physical Review B*, 59(3):1758, 1999.

[192] John P Perdew, Kieron Burke, and Matthias Ernzerhof. Generalized gradient approximation made simple. *Physical review letters*, 77(18):3865, 1996.

[193] Kieron Burke, John P Perdew, and Matthias Ernzerhof. Why semilocal functionals work: Accuracy of the on-top pair density and importance of system averaging. *The Journal of chemical physics*, 109(10):3760–3771, 1998.

[194] Ankita Katre, Jesús Carrete, Bonny Dongre, Georg K. H. Madsen, and Natalio Mingo. Exceptionally Strong Phonon Scattering by B Substitution in Cubic SiC. *Phys. Rev. Lett.*, 119:075902, Aug 2017.

[195] A. Kundu, N. Mingo, D. A. Broido, and D. A. Stewart. Role of light and heavy embedded nanoparticles on the thermal conductivity of SiGe alloys. *Phys. Rev. B*, 84:125426, Sep 2011.

[196] Ankita Katre, Jesús Carrete, and Natalio Mingo. Unraveling the dominant phonon scattering mechanism in the thermoelectric compound ZrNiSn. *J. Mater. Chem. A*, 4:15940–15944, 2016.

[197] Ankita Katre, Jesús Carrete, Tao Wang, Georg K. H. Madsen, and Natalio Mingo. Phonon transport unveils the prevalent point defects in GaN. *Phys. Rev. Materials*, 2:050602, May 2018.

[198] Paolo Giannozzi, Stefano Baroni, Nicola Bonini, Matteo Calandra, Roberto Car, Carlo Cavazzoni, Davide Ceresoli, Guido L Chiarotti, Matteo Cococcioni, Ismaila Dabo, et al. Quantum espresso: a modular and open-source software project for quantum simulations of materials. *Journal of physics: Condensed matter*, 21(39):395502, 2009.

[199] G.S. Nolas, J. Sharp, and J. Goldsmid. *Thermoelectrics: Basic Principles and New Materials Developments*. Springer Series in Materials Science. Springer Berlin Heidelberg, 2001.

[200] Shuo Chen and Zhifeng Ren. Recent progress of half-Heusler for moderate temperature thermoelectric applications. *Materials Today*, 16(10):387 – 395, 2013.

[201] Binghai Yan and Shou-Cheng Zhang. Topological materials. *Reports on progress in physics. Physical Society (Great Britain)*, 75:096501, 08 2012.

[202] F. Aliev, N. Brandt, Victor Moshchalkov, V. Kozyrkov, R. Skolozdra, and A. Belogorokhov. Gap at the Fermi level in the intermetallic vacancy system RBiSn(R=Ti,Zr,Hf). *Zeitschrift für Physik B Condensed Matter*, 75:167–171, 06 1989.

[203] F. G. Aliev, V. V. Kozyrkov, V. V. Moshchalkov, R. V. Scolozdra, and K. Durczewski. Narrow band in the intermetallic compounds MNiSn (M=Ti, Zr, Hf). *Zeitschrift für Physik B Condensed Matter*, 80(3):353–357, Oct 1990.

[204] I Galanakis and Ph Mavropoulos. Spin-polarization and electronic properties of half-metallic Heusler alloys calculated from first principles. *Journal of Physics: Condensed Matter*, 19(31):315213, jul 2007.

[205] Tanja Graf, Claudia Felser, and Stuart S.P. Parkin. Simple rules for the understanding of heusler compounds. *Progress in Solid State Chemistry*, 39(1):1–50, 2011.

[206] Jesús Carrete, Wu Li, Natalio Mingo, Shidong Wang, and Stefano Curtarolo. Finding Unprecedentedly Low-Thermal-Conductivity Half-Heusler Semiconductors via High-Throughput Materials Modeling. *Physical Review X*, 4(1):011019, February 2014.

[207] Xiuwen Zhang, Liping Yu, Andriy Zakutayev, and Alex Zunger. Sorting Stable versus Unstable Hypothetical Compounds: The Case of Multi-Functional ABX Half-Heusler Filled Tetrahedral Structures. *Advanced Functional Materials*, 22(7):1425–1435, 2012.

[208] Sandip Bhattacharya and Georg K. H. Madsen. A novel p-type half-Heusler from high-throughput transport and defect calculations. *J. Mater. Chem. C*, 4, 01 2016.

[209] Hangtian Zhu, Jun Mao, Yuwei Li, Jifeng Sun, Yumei Wang, Qing Zhu, Guannan Li, Qichen Song, Jiawei Zhou, Fu Yuhao, Ran He, Tian Tong, Zihang Liu, Wuyang Ren, Li You, Zhiming Wang, Jun Luo, Andrei Sotnikov, Jiming Bao, and Hassan Ahmoum. Discovery of TaFeSb-based half-Heuslers with high thermoelectric performance. *Nature Communications*, 10, 01 2019.

[210] Jiawei Zhou, Hangtian Zhu, Te-Huan Liu, Qichen Song, Ran He, Jun Mao, Zihang Liu, Wuyang Ren, Bolin Liao, David Singh, Zhifeng Ren, and Gang Chen. Large thermoelectric power factor from crystal symmetry-protected non-bonding orbital in half-Heuslers. *Nature Communications*, 9, 04 2018.

[211] Akant Sagar Sharma, Subhasis Das, Sanowar Alam Gazi, and S. Dhar. Influence of Pb vs Ga solvents during liquid phase epitaxy on the optical and electrical properties of GaSbBi layers. *Journal of Applied Physics*, 126(15):155702, 2019.

[212] Stefano Curtarolo, Wahyu Setyawan, Shidong Wang, Junkai Xue, Kesong Yang, Richard H. Taylor, Lance J. Nelson, Gus L.W. Hart, Stefano Sanvito, Marco Buongiorno-Nardelli, Natalio Mingo, and Ohad Levy. Aflowlib.org: A distributed materials properties repository from high-throughput ab initio calculations. *Computational Materials Science*, 58:227 – 235, 2012.

[213] D.G. Pettifor. A chemical scale for crystal-structure maps. *Solid State Communications*, 51(1):31 – 34, 1984.

[214] Mauro Fava, Bonny Dongre, Jesús Carrete, Ambroise van Roekeghem, Georg K. H. Madsen, and Natalio Mingo. Effects of doping substitutions on the thermal conductivity of half-heusler compounds. *Phys. Rev. B*, 103:174112, May 2021.

[215] Genadi Naydenov, Philip Hasnip, Vlado Lazarov, and Matt Probert. Huge power factor in p-type half-Heusler alloys NbFeSb and TaFeSb. *Journal of Physics: Materials*, 2, 04 2019.

[216] J. Yang, G. P. Meisner, and L. Chen. Strain field fluctuation effects on lattice thermal conductivity of ZrNiSn-based thermoelectric compounds. *Applied Physics Letters*, 85(7):1140–1142, 2004.

[217] Alex Petersen, S. Bhattacharya, T. M. Tritt, and S. J. Poon. Critical analysis of lattice thermal conductivity of half-Heusler alloys using variations of Callaway model. *Journal of Applied Physics*, 117(3):035706, 2015.

[218] S. Bhattacharya, M. J. Skove, M. Russell, T. M. Tritt, Y. Xia, V. Ponnambalam, S. J. Poon, and N. Thadhani. Effect of boundary scattering on the thermal conductivity of TiNiSn-based half-Heusler alloys. *Phys. Rev. B*, 77:184203, May 2008.